

# Reconstruction and stability analysis of interfaces between electrically conducting fluids

Dissertation

zur Erlangung des akademischen Grades

Doktor-Ingenieur (Dr.-Ing.),

vorgelegt der Fakultät für Maschinenbau  
der Technischen Universität Ilmenau

von Dipl.-Ing. Oleksiy Kurenkov  
geboren am 03. Juni 1975 in Kiew (Ukraine)

1.Gutachter	Prof. Dr.rer.nat. habil. A. Thess
2.Gutachter	Prof. Dr.rer.nat. habil. Y.B. Kolesnikow
3.Gutachter	Prof. Dr.-Ing. habil. M. Oberlack

Tag der Einreichung: 22.12.2004

Tag der wissenschaftlicher Aussprache: 16.06.2005



# Zusammenfassung

Der Gegenstand dieser Arbeit ist die lineare Stabilitätsanalyse einer instabilen Aluminium/Kryolith Grenzfläche in Aluminium-Elektrolysezellen (im Folgenden als "Alu-Zelle" bezeichnet) mit einer Strömung ("background flow") sowie Methoden für die Rekonstruktion der Aluminium/Kryolith Grenzfläche in einer Alu-Zelle. Es wurden zwei Rekonstruktionsprobleme behandelt: die Rekonstruktion aus der Störung des elektrischen Potentials bzw. aus der Störung des Magnetfelds. Die Ursache für beide Störungen ist die Grenzflächenauslenkung. Die lineare Stabilitätsanalyse wurde an einem vereinfachten Modell durchgeführt. Es wurde die Ausbreitung von Gravitationswellen unter Einfluss von Magnetfeldern in einem unendlich ausgedehnten Kanal mit isolierenden Wänden studiert. Ein homogener elektrischer Strom und ein Magnetfeld wurden angelegt. Die Navier-Stokes Gleichung wurde in einer Flachwassernäherung aufgeschrieben und dann linearisiert. Alle Variablen wurden durch Mittelwert und Störung dargestellt. Die Gleichungen für die Störungsgrößen wurden hergeleitet und anschließend eine Normalmodenanalyse durchgeführt. Als Resultat wurde ein kompaktes Gleichungssystem gewonnen, das nur die Grenzflächen-deformation und die Störung des elektrischen Potentials beinhaltet. Es wurden vier dimensionslose Parameter gefunden. Die dimensionslose Geschwindigkeit des "background flow" und der MHD-Parameter begrenzen den Stabilitätsbereich. Das Aspektverhältnis und die Materialeigenschaften beeinflussen die Stabilitätsgrenzen. Es wurde festgestellt, dass die Entstehung der Kelvin-Helmholtz-Instabilität und die Entstehung der MHD-Instabilität zwei voneinander unabhängige Ereignisse sind. Allerdings wird die Form der Grenzflächenwellen durch die Lorentzkraft modifiziert.

Die Rekonstruktion der Grenzfläche in einer Alu-Zelle aus dem elektrischem Potential beinhaltet zwei Klassen von unterschiedlichen Problemen. Das erste Problem, das sogenannte Vorwärtsproblem, betrifft die Berechnung eines elektrischen Potentials in den Fluiden bei bekannter Grenzflächendeformation. Die Lösung des Vorwärtsproblems ist gewöhnlich eindeutig, d.h. die Störung des elektrischen Potentials kann immer mit beliebiger Genauigkeit berechnet werden. Das zweite Problem, das sogenannte Inverse Problem, umfasst die Bestimmung von einer unbekanntem

Grenzfläche aus der gegebenen (oder experimentell gemessenen) Potentialverteilung. Ein solches Problem ist schwer lösbar, weil eine Menge von Grenzflächen existieren die sehr ähnliche Potentialverteilungen hervorrufen. Der Messfehler bei der Potentialmessung erschwert die Rekonstruktion zusätzlich.

Bei der Lösung des Vorwärtsproblems wurden die Gleichungen linearisiert und anschließend analytisch gelöst. Das Inverse Problem wurde mit Standardtechniken wie Singulär-Wert Zerlegung für unterschiedliche Modenzahlen gelöst. Anschließend wurde eine optimale Lösung mittels L-Kurve gefunden, die als Kompromiss zwischen dem Datenfehler und dem Lösungsfehler gewählt wurde. Ein numerisches Experiment wurde zwecks Validierung der präsentierten Methode durchgeführt. Die Grenzfläche wurde vorgegeben und die Potentialverteilung wurde mit Hilfe einer analytischen Lösung für das Vorwärtsproblem berechnet. Dann wurde weißes Rauschen zu dem berechneten elektrischem Potential addiert. Die genannten Operationen simulieren eine Messung unter realen Bedingungen. Diese Dateien wurden zur Rekonstruktion genutzt. Die rekonstruierte Grenzfläche war der vorgegebenen Grenzfläche sehr ähnlich.

Für die Rekonstruktion der Grenzfläche aus dem Magnetfeld wurde das Vorwärtsproblem gelöst. Hierzu wurden die Störung des Magnetfeldes und die Stromverteilung in einem Zweifluidsystem berechnet. Die Geometrie des Systems wurde als ein unendlich ausgedehnter Zylinder mit isolierenden Wänden und beliebiger Querschnittsform beschrieben. Zwei Fluide mit unterschiedlichen elektrischen Leitfähigkeiten und Dichten sind übereinander angeordnet. Der vertikale homogene elektrische Strom fließt über die Grenzfläche. Die Magnetfeldstörung und die Inhomogenität des elektrischen Stroms sind ein Resultat der Grenzflächendeformation. Die Analyse basiert auf dem Biot-Savart'schen Gesetz, welches für dieses spezielle Problem zwecks Verringerung des Rechenaufwands vereinfacht werden kann. Die Lösung für eine beliebige Querschnittsform wurde erzielt. Zwei Beispiele wurden berechnet, eins für eine kreisförmige Querschnittsform und ein anderes für eine rechteckige Querschnittsform. Die präsentierte Analyse stellt die Lösung des Vorwärtsproblems für die Rekonstruktion der Grenzfläche in einer Aluminium-Elektrolysezelle dar.

**Begriffe:** Aluminum-Elektrolysezelle, lineare Stabilitätsanalyse, Inverses Problem

# Abstract

The topic of this thesis is the linear stability analysis of an unstable aluminium-cryolite interface in the aluminium reduction cell (in the following it will be denoted as "Alu-cell" ) with background flow and the reconstruction of the aluminum-cryolite interface in the Alu-cell. Two reconstruction problems are considered. In the first one the interface was reconstructed from the electric potential perturbation and in the second one from the magnetic field perturbation. Both perturbations resulted from the deviation of the aluminium-cryolite interface from its flat shape.

The stability analysis of the aluminium reduction cell was performed on a simplified geometrical model. The propagation of gravitational waves in the infinite channel with insulating channel walls was observed. Homogeneous vertical electrical current and magnetic field were applied. Navier-Stokes equations were written in the shallow water approximation and then linearized. All quantities are presented as mean value and perturbation. Equations for the perturbed quantities were derived. Then the normal mode approach was used. As a result a compact system of equations containing only the interface displacement and the electrical potential perturbation was obtained. Four dimensionless parameters are obtained. In particular one find that the dimensionless velocity of the background flow and the MHD-parameter form the stability thresholds. Also the aspect ratio and the material parameter influence the stability limits. It is found that the Kelvin-Helmholtz instability and the MHD-instability do not influence each other. However, the form of the interfacial waves is modified under the influence of the Lorentz force.

The reconstruction of the interface in aluminium reduction cells from electrical potential measurement contains two classes of different problems. The first problem, so-called forward problem, concerns with the calculation of the electrical potential in the fluids if the interface shape between aluminium and cryolite is known. The solution of the forward problem is usually unique, i.e. the potential perturbation can always be computed with high Faccuracy. The second problem, the so-called inverse problem, concerns with the determination of the unknown interface from a given (or experimentally measured) potential distribution. Such a problem is very

difficult to solve, because there exist a lot of interfaces which corresponds to similar potential distributions. The measurement errors in potential distributions make the reconstruction of interfaces much more difficult.

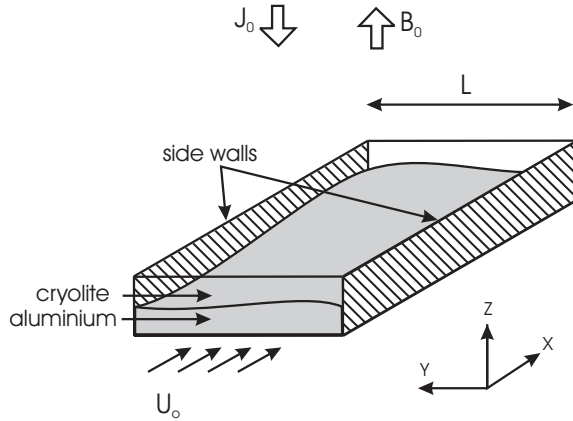
In order to solve the forward problem the governing equations are linearized and solved analytically. The inverse problem was solved using standard techniques such as singular value decomposition (SVD). The optimal solution which shows a compromise between data error and solution error, was found using a L-curve criterion [33]. A numerical experiment is performed in order to validate the presented reconstruction method. The interface was prescribed and the potential distribution was computed using the analytical solution of the forward problem. Then white noise was added to the computed electrical potential perturbation and this data was used for the reconstruction. This operations simulate the measurement under real conditions. The reconstructed interface was similar to the prescribed one.

For the reconstruction problem based on the magnetic field perturbation the forward problem was solved, namely the magnetic field perturbation and the electrical current perturbation were computed. The geometry under consideration contains an infinitely long rod with insulating walls and arbitrary form of the cross-section. Two fluids with different electrical conductivities and densities are superimposed. The vertical homogeneous electrical current flows through the interface. The perturbation of the magnetic field and the electrical current result from the inhomogeneity of the electrical current which is a result of the interface displacement. The analysis is based up on the Biot-Savart law which can be simplified in this special problem in order to decrease the computational costs. Expressions for the arbitrary form of the cross-section are obtained. Two examples are computed, one for a cylindrical and another for a rectangular cross-sections. The analysis presented can be used as the solution of the forward problem for the reconstruction of the interface in aluminium reduction cells.

**Key words:** aluminium reduction cell, linear stability analysis, inverse problem

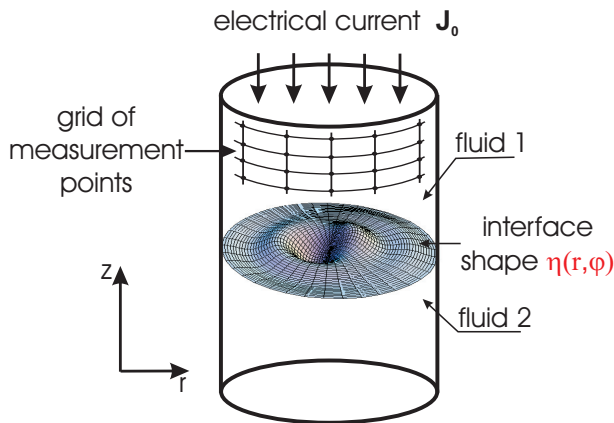
# The problems discussed in PhD

## 1. Linear stability analysis of Alu-Cell.



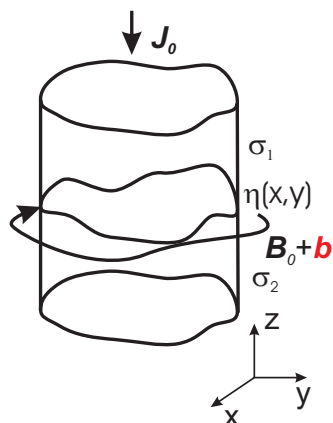
- Known: electrical current  $J_0$ , magnetic field  $B_0$ , thickness of layers  $h$ ,  $H$ , mean velocity  $U_0$ , channel width  $L$ , densities  $\rho_a$ ,  $\rho_c$
- Goal: Linear stability analysis of the unstable interface between aluminium and cryolite

## 2. Reconstruction of the interface from electric potential measurements: forward and inverse problem.



- Known: electrical potential  $\phi$ , electrical conductivities  $\sigma_1$ ,  $\sigma_2$ , mean electrical current  $J_0$
- Goal: Reconstruction of the interface shape  $\eta(r, \phi)$

## 3. Reconstruction of the interface from magnetic field measurements: forward problem.



- Known: interface shape  $\eta(r, \phi)$ , electrical current  $J_0$ , electrical conductivities  $\sigma_1$ ,  $\sigma_2$
- Goal: Computation of the electrical current perturbation  $j(r, \phi)$  and magnetic field perturbation  $b(r, \phi)$





# Preface

This thesis concerns with the treatment of the inverse problem of interface reconstruction in aluminium reduction cells and the linear stability analysis of the simplified model of aluminium reduction cells.

In chapter 2, a linear stability analysis of the simplified model of aluminium reduction cell is performed. The goal of the investigation was to find the influence of the mean flow on the stability of the aluminium reduction cell. We consider an infinite channel with electrically non-conducting walls. Thin layers of cryolite and aluminium are superimposed. A vertical homogeneous electrical current and magnetic field are applied in opposite directions. In the steady state, a mean flow in the aluminium is assumed, while the cryolite is at rest. Two different kinds of instability appear. The Kelvin-Helmholtz instability is a result of the different flow velocities in aluminium and cryolite. The second instability, namely MHD-instability, is produced by Lorentz forces, which are the result of nonuniformities of electrical current due to the interface perturbations. At the numerical point of view, the problem is solved in the shallow water approximation using normal mode analysis. Four dimensionless parameters are derived which influence the onset of instability.

In chapter 3, a method for reconstruction of unstable interface in aluminium reduction cells is developed. We consider the small (in comparison to the dimensions of the cell) oscillations of the interface. The interface between cryolite and aluminium is described as a sum of orthogonal functions (modes). An analytical solution for the solution of the forward problem (computing the potential perturbation from the known interface shape) was found. The inverse problem (the determining of the interface from the known potential distribution) is solved using the SVD-decomposition[52] and the L-curve criterion[33], [38].

In chapter 4, the perturbed electrical current and magnetic field in a two fluid system is computed. In an infinitely long rod with insulating walls two fluids with different conductivities are superimposed. The form of the cross-section is arbitrary. Homogeneous electrical current flows through the interface. For a known interface form the perturbation of the electrical current and the perturbation of the magnetic field are computed. The computation is based on the Biot-Savart law which can be simplified for this special problem. The method presented can be used for the treatment of the forward problem in the reconstruction of the interface in the aluminium reduction cell.

The appendix contains five parts. In part **A** the linear stability analysis of the half-limited system which is a particular case of the system studied in section 2 is presented. The system with one wall is analyzed, which is the special case of the channel flow (see section 2), if the walls of the channel are far from each other. In appendix **B** an overview of some relevant patents in the field of electrical impedance tomography is given. In appendix **C** the proof of uniqueness of the interface mapping into the potential perturbation is given. This part extends the results given in section 3. In appendix **D** it is proven that the Bessel functions describe the interface separating of the fluids in a cylindrical rod. The equations are directly derived from the equations of fluid mechanics. The representation of the interface as a superposition of Bessel functions is used at the solution of the forward problems treated in the chapters 3 and 4. Appendix **E** contains a paper "Reconstruction of interfaces between electrically conducting fluids from electrical potential measurements". A.Kurenkov and A.Thess. *Proc. of the PAMIR Conference, 2000, France*. The algorithm of interface reconstruction from electrical potential measurement is presented in this paper. Because of the limits of conference proceeding only the basic idea of reconstruction is presented with a small number of examples.

# Table of Contents

<b>Preface</b>	<b>ix</b>
<b>1 Introduction</b>	<b>1</b>
1.1 The subject of investigation: Aluminium reduction cell . . . . .	1
1.2 Stability of the aluminium reduction cells . . . . .	4
1.2.1 Background . . . . .	4
1.2.2 Basic instability mechanisms . . . . .	6
1.3 Reconstruction of interfaces in aluminium reduction cells using elec- tric potential measurements . . . . .	9
1.3.1 Background . . . . .	9
1.3.2 Electrical impedance tomography . . . . .	11
1.3.3 Inverse problems: definitions and classification. . . . .	12
1.4 Reconstruction of interfaces in aluminium reduction cells using mag- netic field measurements . . . . .	13
<b>2 Stability of aluminium reduction cells with mean flow</b>	<b>17</b>
2.1 Statement of the problem . . . . .	17
2.2 Basic equations . . . . .	18
2.2.1 Governing equations and basic flow . . . . .	18
2.2.2 Evolution of small perturbations . . . . .	19
2.2.3 Normal mode analysis and stability equations . . . . .	21
2.2.4 Non-dimensional parameters . . . . .	22
2.3 Solution of the stability problem . . . . .	23
2.3.1 The general case: Interaction between MHD-instability and Kelvin-Helmholtz instability . . . . .	23

2.3.2	The particular case of a pure Kelvin-Helmholtz instability ( $N = 0$ ) . . . . .	25
2.3.3	The particular case of a pure MHD instability ( $M = 0$ ) . . . . .	26
2.4	Results . . . . .	26
2.4.1	The general case: MHD-Instability and Kelvin-Helmholtz in- stability . . . . .	26
2.4.2	The particular case of a pure Kelvin-Helmholtz Instability . . . . .	27
2.4.3	The particular case of a pure MHD Instability . . . . .	30
2.5	Summary and conclusion . . . . .	32
<b>3</b>	<b>Reconstruction of interfaces from electric potential measurements: forward and inverse problem</b>	<b>33</b>
3.1	Statement of the problem . . . . .	33
3.2	Forward problem . . . . .	35
3.2.1	The interface perturbation . . . . .	35
3.2.2	Electrical potentials in the fluids . . . . .	36
3.2.3	Non-dimensional equations . . . . .	40
3.3	Inverse problem . . . . .	41
3.3.1	Basic location of the interface . . . . .	41
3.3.2	Reconstruction of axisymmetric interface . . . . .	42
3.3.3	Reconstruction of the non-axisymmetric interface . . . . .	47
3.3.4	Choice of optimal reconstruction parameters . . . . .	48
3.4	Examples of interface reconstruction . . . . .	50
3.5	Conclusion . . . . .	52
<b>4</b>	<b>Reconstruction of interfaces in aluminium reduction cells using magnetic field measurements: forward problem</b>	<b>55</b>
4.1	Introduction . . . . .	55
4.2	Governing equations . . . . .	56
4.2.1	Interface displacement . . . . .	56
4.2.2	Computation of perturbed electrical current . . . . .	57
4.2.3	Computation of the magnetic field perturbation . . . . .	59
4.3	Results . . . . .	62

---

4.4	Conclusions . . . . .	67
<b>5</b>	<b>Conclusions</b>	<b>69</b>
<b>6</b>	<b>Appendix</b>	<b>71</b>
6.1	Appendix A: Linear stability analysis in the half-bounded system . .	71
6.1.1	Formulation of the stability problem . . . . .	71
6.1.2	Basic equations . . . . .	72
6.1.3	Solution of the stability problem . . . . .	74
6.1.4	Discussion of the results . . . . .	75
6.2	Appendix B: EIT Patents . . . . .	78
6.3	Appendix C: Inverse problem of interface reconstruction: uniqueness proof . . . . .	80
6.4	Appendix D: Bessel functions as the set of orthonormal functions describing the interface separating fluids in a cylinder. . . . .	83
6.5	Appendix E: Reconstruction of interfaces between electrically con- ducting fluids from electrical potential measurements. A.Kurenkov and A.Thess. <i>Proc. of the PAMIR Conference, 2000, France.</i> . . . .	86
6.5.1	Introduction . . . . .	86
6.5.2	Forward problem . . . . .	88
6.5.3	Inverse problem . . . . .	89
6.5.4	Examples of interface reconstruction . . . . .	89
6.5.5	Conclusion . . . . .	91
	<b>Bibliography</b>	<b>93</b>
	<b>Acknowledgments</b>	<b>99</b>



# Chapter 1

## Introduction

### 1.1 The subject of investigation: Aluminium reduction cell

Aluminium is the earth's most abundant metallic element, making up approximately eight per cent of the planet's crust. It is commonly found in the form of oxides and aluminium never occurs naturally in its pure form. The most commercially viable source of aluminium is bauxite, which contains about 75 % hydrated alumina ( $Al_2O_3 \cdot 3H_2O$  and  $Al_2O_3 \cdot H_2O$ ). It is predominantly found in tropical and subtropical regions of the world, but also in Europe.

The process of aluminium production can be divided into the following main stages: 1) bauxite mining, 2) alumina refining, 3) smelting, and 4) processing [72]. Typically bauxite is extracted by open cast mining. In the second stage (refining) bauxite is washed, ground into a powder and mixed with a solution of caustic soda in autoclaves. There, under pressure and at a high temperature, the caustic soda combines with the hydrated alumina to leave a solution called sodium aluminate. Any impurities remain as undissolved residue and are filtered. The chemical reactions which are acting in this stage will be not described in detail in this thesis because it is not the aim of this work. As a result, the alumina (aluminium oxide  $Al_2O_3$ ) in the form of white powder like a table salt is obtained, which is used in the next stage for manufacturing of pure aluminium.

The next stage is the smelting or the aluminium reduction. This Ph.D. thesis

is devoted to the problems which appear here and which will be described in more details. The reduction of aluminium is based on the Hall-Heroult process invented in 1886. The reduction process acts in the aluminium reduction cells (see Fig. 1.1). Alumina (aluminium oxide  $\text{Al}_2\text{O}_3$ ) is dissolved in an electrolytic bath of molten cryolite (sodium aluminium fluoride  $\text{Na}_3\text{AlF}_6$ ) which is placed in a large graphite or carbon steel lined container. The last plays the role of a cathode and is called "a pot". Electric current which can be as strong as 500kA in modern cells passes through carbon anodes into the electrolyte layer. It crosses the underlying liquid aluminium layer and leaves the cell through carbon cathode blocks and embedded iron bars. Molten aluminium appears at the bottom of the pot. It is periodically pumped out, cleaned, cooled and processed. The operation and control dispose some difficulties because the temperature of the electrolytic bath is about  $970^\circ\text{C}$  and liquid and hot aluminium is chemically aggressive. Aluminium reduction cells

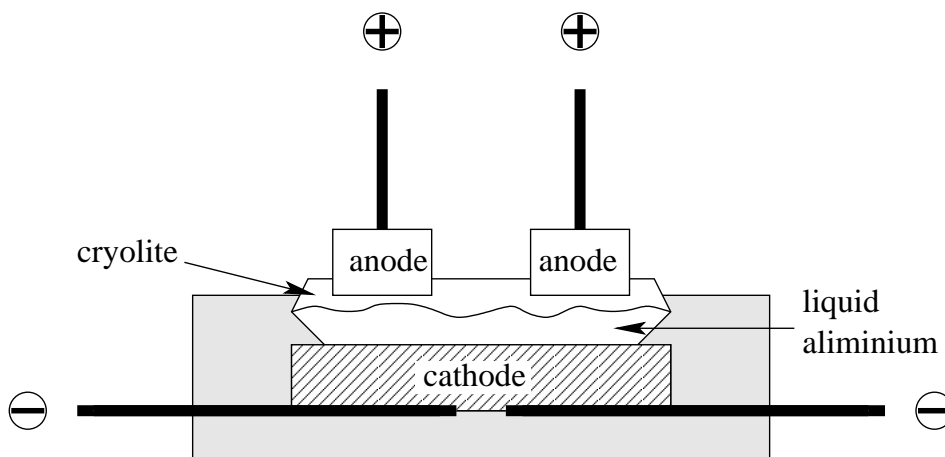


Figure 1.1: A schetch of aluminium reduction cell.

are combined in so-called potlines (see Fig. 1.2). Typically one aluminium smelter consists of about 300 pots and produces about 125000 t aluminium annually [72].

Aluminium manufacturing is a very energy intensive process:  $\sim 5\%$  of all electrical energy produced worldwide is spent by aluminium reduction cells [48]. For the producing of one kg of pure aluminium approximately 21,5 kWh of electrical energy is necessary. Therefore aluminium smelters are mostly located in the regions where the electrical energy is cheap. The main part of research topics in aluminium industry is devoted to the question how the Hall-Herault process can be made more





Figure 1.2: A reduction line (sometimes called a potline) at Boyne Smelters Limited, near Gladstone, Queensland, Australia. Comalco.

energy efficient. The main part of electrical energy applied to Alu-cell disappears as Joule losses in the cryolite layer because the cryolite is a very poor conductor in comparison with the molten aluminium. Therefore it is necessary to keep the cryolite layer as thin as possible. But the main problem of aluminium reduction cell is that the interface between the aluminium and cryolite is unstable. It moves periodically under the influence of interaction of interfacial waves with the vertical component of magnetic field and/or the vertical component of the electrical current. The vertical component of magnetic field is always presented in the system as a far-field from a busbar system. It can be concluded, that the questions about the control and measurement of the unstable aluminium - cryolite interface are the key points in the modern aluminium manufacturing.

In this Ph.D. thesis two major directions of aluminium cell investigation are studied. The first part is devoted to the stability analysis of the Alu-cell. In the next subsections the motivation of this study are presented. The second one deals with the methods for the reconstruction of the cryolite-aluminium interface in Alu-cell. Two different possibilities are studied: the reconstruction using the potential

measurement on the cell boundary and the reconstruction using magnetic field measurement outside the cell.

## 1.2 Stability of the aluminium reduction cells

### 1.2.1 Background

The interface between cryolite and aluminium in an aluminium reduction cell is in permanent motion under the influence of Lorentz forces. Under some conditions this motion can lead to different instabilities. The uncontrolled growth of the interface shape can damage the operation of the aluminium reduction cell. It can lead to a short-circuit between electrodes with the following destruction of the Alu-cell. Therefore the stability analysis of Alu-cell is a relevant safety aspect. Another reason is that an instability of the cryolite-aluminium interface reduces the total amount of aluminium produced by the cell.

Let us consider the configuration of Alu-cells in details. The consumable anodes are suspended in the molten electrolyte (cryolite) by means of a steel structure, which allows adjustment of the anode-cathode distance (ACD). The separation between anode bottom and aluminium surface is usually 5cm. The typical depth of aluminium layer is  $\sim 20$ cm. Taking into account the horizontal dimensions of the cell as the order of few meters (typically 4x10m), one can consider the system as rather shallow.

The electric current and the magnetic field, generated by currents both inside and outside of the cell and the magnetization of the steel shell, create Lorentz forces, which stir both liquid electrolyte and metal. With current densities of  $0.8A/cm^2$  velocities of  $\sim 20cm/s$  are common and useful in distributing the fed aluminium oxide and avoiding the formation of a sludge. However, the density difference of only about 10% between liquid bath and metal allows distortions of the aluminium-electrolyte interface in the magnitude of centimeters. The current distribution in the ACD is very sensitive to these deformations, as the electric resistivity of the electrolyte is much higher than that of liquid aluminium. As long as these deformations are steady-state the consumption speed of the anodes, which is proportional to the current density, will level out the differences in ACD distribution.

Depending on the distribution of the electric current and magnetic field the self-exciting magnetohydrodynamic oscillation of the interface can occur. A perturbation of the interface leads to the redistribution of the electric current and magnetic field and, consequently, Lorentz forces. Under certain circumstances the Lorentz force perturbation can increase the amplitude of the interface wave in the cell. This kind of behavior called "shake or metal pad roll" is detected by the fluctuations of the net cell resistance and often counteracted by lifting the anodes slightly and thus increasing the ACD. As the electrolyte has the largest contribution to the ohmic resistance of the cell, this measure increases the production of Joule heat and therefore leads to a disturbance of the heat balance of the cell and additional energy consumption. On the other hand, any turbulence caused by the velocity gradients at the interface during an instability decreases the amount of produced metal, measured as current efficiency, as it transports already reduced aluminium back into the electrolyte with the chance of re-oxidation.

Although the mechanism of MHD instabilities in connection with aluminium production cells has been investigated for more than 30 years, the complexity of the problem is still challenging. Design and operation of cells with higher amperage and continued demand for lower energy consumption requires both a detailed theoretical understanding of the underlying physical principles and accurate numerical models. The development in this direction has a long history from a basic criterion for the magnetic field [59], over principle MHD stability analysis [46], [47] and shallow water approximations [66], [24], to detailed three-dimensional models [58] of instabilities including the physical effects of induced electric currents, mean flow, cavity size and many geometric details such as anode channels and ledge profile. Interaction between the horizontal perturbations of electric currents and the vertical component of unperturbed magnetic field has been identified as the most significant mechanisms of the MHD stability.

The linear stability analysis performed in [4] and [60] leads to a wave equation for the interface deviation

$$\frac{\partial^2 \boldsymbol{\eta}}{\partial t^2} + \boldsymbol{\Omega}^2 \boldsymbol{\eta} = \epsilon \mathbf{K} \boldsymbol{\eta} \quad (1.1)$$

where  $\boldsymbol{\eta}$  is a vector with amplitudes of Fourier interface modes, diagonal matrix  $\boldsymbol{\Omega}$  contains gravitational frequencies of interface oscillations,  $\mathbf{K}$  is the matrix with

magnetic interaction coefficients, scalar  $\epsilon$  is a dimensionless measure of relative importance of gravitational and magnetic forces to interfacial waves. With vanishing electrical current or magnetic field, the solutions of the eigenvalue problem (1.1) reduces to the standard gravitational wave spectra, with all real eigenvalues. At increasing current density and magnetic field or decreasing ACD or density difference, the solution is modified so that the pairs of the eigenvalues degenerate to form complex-valued eigenmodes indicating the onset of the MHD instability. The shape of the unstable interface modes are always that of propagating waves, while the real eigenmodes are just deformed gravitational standing waves. The most basic instability mode in the aluminium reduction cell is a rotating single-crest wave.

The flows driven by the Lorentz forces in an Alu-cell can also become unstable. The motivation of the study presented in the chapter 2 is the understanding of the role of background flow in the Alu-cell. Two types of instability are studied, one originating from the interaction of electrical current in the flow with magnetic field and another one is the instability of the flow itself. In the next subsection the basic instability mechanisms for both instabilities are discussed.

### 1.2.2 Basic instability mechanisms

Before we begin with the numerical analysis of the stability problem, let us describe the principal physical mechanism of the instabilities, under consideration, which are (1) Kelvin-Helmholtz instability and (2) MHD-instability.

The Kelvin-Helmholtz instability is illustrated in Fig. 1.3(a). Two fluids are superimposed. The upper one has smaller density in comparison to the lower one so that in the absence of any flow the basic state is stable. If, however, there are horizontal flows in the fluid layers and the velocity field is discontinuous at the interface, an instability appears. This instability, called Kelvin-Helmholtz instability, is well known and is described in classical textbooks on hydrodynamic stability such as Chandrasekhar [13] or Drazin & Reid [23].

MHD-instabilities arise as a result of a closed-loop interaction between the internal gravity waves and Lorentz forces  $\mathbf{F} = \mathbf{J} \times \mathbf{B}$ . Here,  $\mathbf{J}$  represents the electric current distribution within the cell, while  $\mathbf{B}$  is the magnetic field created by currents from all cells in a plant including the considered one. Crucial for understanding the

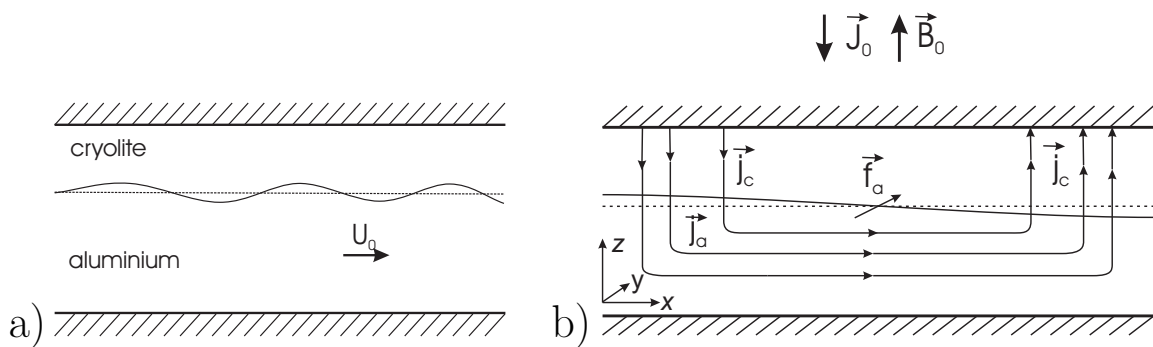


Figure 1.3: Mechanisms of instabilities in aluminium reduction cells. a) Kelvin-Helmholtz instability. b) MHD instability of type I.

MHD instabilities is the observation that the spatial distribution of the electric current and, thereby, the Lorentz force depend strongly on the unknown shape  $\eta(x, y, t)$  of the cryolite-aluminum interface because of the strong disparity in the electrical conductivities of aluminum and cryolite. The aluminum is an excellent conductor, the cryolite is a very poor conductor. While  $\mathbf{J}$  and  $\mathbf{B}$  have a highly complex spatial structure in a real aluminum reduction cell, the mechanism for MHD instability can be best understood in the simplified case sketched in Fig. 1.3(b). We assume that both the fluids are at rest and that the basic (unperturbed) state of a cell is characterized by a flat interface ( $\eta = 0$ ), vertical electrical current distribution  $\mathbf{J}_0 = -J_0 \mathbf{e}_z$  and a magnetic field whose dominant component is  $\mathbf{B}_0 = B_0 \mathbf{e}_z$ . It is obvious that the unperturbed Lorentz force  $\mathbf{F}_0 = \mathbf{J}_0 \times \mathbf{B}_0$  is zero in this case and, therefore,  $\eta = 0$  represents an equilibrium state.

As soon as the interface deviates from its flat shape, the distribution of the electrical current is altered due to the arising variations of local resistivity of the cryolite layer. As a result, the electrical current is perturbed according to  $\mathbf{J} = \mathbf{J}_0 + \mathbf{j}$  and the magnetic field becomes  $\mathbf{B} = \mathbf{B}_0 + \mathbf{b}$ , where  $\mu_0 \mathbf{j} = \nabla \times \mathbf{b}$ . The Lorentz force, which can be written as  $\mathbf{F} = \mathbf{j} \times \mathbf{B}_0 + \mathbf{J}_0 \times \mathbf{b} + \mathbf{j} \times \mathbf{b}$  is, thus, no longer zero and can, under favorable conditions, drive an interfacial instability. For infinitesimal surface deformations, the second-order term  $\mathbf{j} \times \mathbf{b}$  in the Lorentz force can be neglected. Depending on whether  $\mathbf{j} \times \mathbf{B}_0$  or  $\mathbf{J}_0 \times \mathbf{b}$  dominates, the instability is called type I or type II MHD instability. Their specific mechanisms are discussed next.

Let us assume that the interface is tilted as shown in Fig. 1.3(b), where  $\mathbf{j}_c$  and  $\mathbf{j}_a$  denote the electric current perturbations in the cryolite and aluminum respectively.

Davidson & Lindsay [18] have shown that  $\mathbf{j}_c$  is predominantly vertical due to the poor conductivity of the cryolite, while  $\mathbf{j}_a$  is essentially horizontal as they close in the highly conducting aluminum bounded by the moderately conducting carbon cathode. The dominant component of the Lorentz force is therefore in the liquid metal (i.e.  $\mathbf{j}_a \times B_0 \mathbf{e}_z$ ). It is directed into the plane of the paper and gives rise to an additional tilt of the interface in the direction perpendicular to the initial tilt. For sufficiently large values of the product  $J_0 B_0$  this mechanism leads to an unstable sloshing motion, called type I instability.

The type II instability arises from the interaction of the perturbed magnetic field  $\mathbf{b}$  with the applied electric current  $J_0 \mathbf{e}_z$ . Davidson & Lindsay [18] have shown that for large aspect ratios (i.e.  $kH \ll 1$  where  $k$  is the longitudinal wavenumber of the perturbation and  $H$  is the depth of the unperturbed aluminum layer) the type II instability is "less dangerous" than type I. Therefore we will restrict our attention to the type I instability and use  $\mathbf{F} = \mathbf{j} \times \mathbf{B}_0$  for the computation of the Lorentz force in the liquid metal. The Lorentz force in the cryolite will be neglected.

Before proceeding to the formulation of the stability problem we mention Davidson & Lindsay's expression for the Lorentz force  $\mathbf{j}_a \times \mathbf{B}_0$  which, in its most compact form, can be written as

$$\mathbf{F} = \frac{J_0 B_0}{Hh} \nabla_{\perp} (\nabla^{-2} \eta)$$

Here  $h$  is the thickness of the cryolite layer,  $\nabla_{\perp} = \mathbf{e}_x \partial / \partial y - \mathbf{e}_y \partial / \partial x$  and  $\nabla^{-2}$  is a symbolic notation for the inverse Laplacian. This formula can be derived by expressing  $\mathbf{j}_a(x, y)$  through the electric potential

$$\mathbf{j}_a = -\sigma_a \nabla \phi$$

and solving the Poisson equation

$$\nabla^2 \phi = -\frac{J_0}{\sigma_a H} \eta(x, y).$$

Details of the derivation can be found in [17] and [18].

At last, we mention one principal aspect of difference between the type I MHD instability (called hereafter MHD instability for simplicity) and the Kelvin-

Helmholtz instability. In contrast to the Kelvin-Helmholtz instability, which produces short waves, the MHD instability generates long wave motions of liquid metal. This effect will be appointed later in the subsection 2.4.

## **1.3 Reconstruction of interfaces in aluminium reduction cells using electric potential measurements**

### **1.3.1 Background**

The knowledge of the position of the interface between highly conducting molten aluminium and poorly conducting liquid cryolite is important to prevent undesirable instabilities in aluminium reduction cells [19]. Unstable cryolite-aluminium interface damages and makes it difficult to operate aluminium reduction cells. Instabilities of aluminium-cryolite interface lead to an uncontrolled rapid growth of interfacial wave with result of a short circuit between the electrodes. Such an accident in an aluminium reduction cell is an real disaster completely destructing a cell. Therefore the interface shape between cryolite and aluminium must be permanently monitored during the operation. This problem is treated in chapter 3.

The cryolite-aluminium interface separates two regions with completely different electrical conductivities. Principally the problem at hand is to determine the electrical conductivity distribution in the cell. Then the sharp jump in the conductivity distribution can be used for detecting the interface. The present reconstruction problem is similar in many respects to the tasks of electrical impedance tomography (EIT). This technique will be shortly described in the next subsection.

The problem of reconstruction of internal impedance distribution occurs in many applications in material processing. There are a lot of problems where it would be useful to know the time-dependent distribution of the electrical conductivity of a single fluid or a multiphase flow. The examples include electrical conductivity distributions in glass melting furnaces, metal-slag interfaces in steel and ironmaking as well as on-line detection of inclusions [32]. The liquids involved in materials processing such as molten metals, semiconductors, and glass melts are mostly hot

and very aggressive. Therefore conventional measurement techniques employing local probes face serious difficulties.

The concepts of electrical impedance tomography (EIT) which have been successfully applied to a variety of medical problems [14] and multiphase flows [28], [12] can be used in order to locate interfaces between current carrying fluids of different electrical conductivity in high-temperature melts. The basic idea of the approach presented in chapter 3 is to exploit the greatest possible extent of the electrical currents which are already present in materials processing operations such as aluminium reduction, electrical glass melting or vacuum arc remelting rather than to inject additional artificial electrical current as it is usually done in EIT applications. In particular, the electrical current flowing through the highly simplified model of an aluminium reduction cell provides sufficient information for reconstruction of the unknown position of the aluminium-cryolite interface.

The problem of interface reconstruction represents a so-called inverse problem [43]. The solution of such a problem is difficult, usually non-unique and unstable. A small measurement error in the electrical potential data set induces a significant error in the solution. It requires a special solution methods. Typically an inverse problem is solved and a set of solution is generated. Then the best solution is chosen applying some criteria defined by the user at the beginning of reconstruction. The most common criterion is so-called L-curve [33] representing a good compromise between data error and any prescribed norm of solution. In subsection 3.3 the theory of inverse problems will be briefly described.

At last it should be noted that the mapping of the interface into the electrical potential perturbation is unique. The proof of this is given in appendix C. It means, that the exact reconstruction of interface is possible. This is not a self-evident fact. There exist a class of problems, which are non-unique. An example showing this problem will be shown in the next section of this thesis. It is impossible to reconstruct the exact interface in Alu-cell from magnetic field measurement outside the cell, because the interface cryolite-aluminium is not uniquely mapped in the magnetic field. Additional information is needed in such cases.



### 1.3.2 Electrical impedance tomography

Electrical impedance tomography (EIT) is a noninvasive technique for the construction of an approximation to the conductivity distribution in a given region from electrical potential data sets which are measured at the boundaries of the region [12]. In comparison with other methods, such as x-ray tomography, it is much cheaper, it does not require any complex and large technical devices and it is generally not dangerous. It is also a very fast method acceptable for online systems working in real time.

The principal idea of an EIT-device (see Fig.1.4) is to apply the electrical current(s) on the electrode(s), which are situated on the surface of the body under testing, and to measure the electrical voltage developed between other electrodes. In order to obtain a suitable picture of the inner body structure it is necessary to conduct hundreds and thousands of measurements.

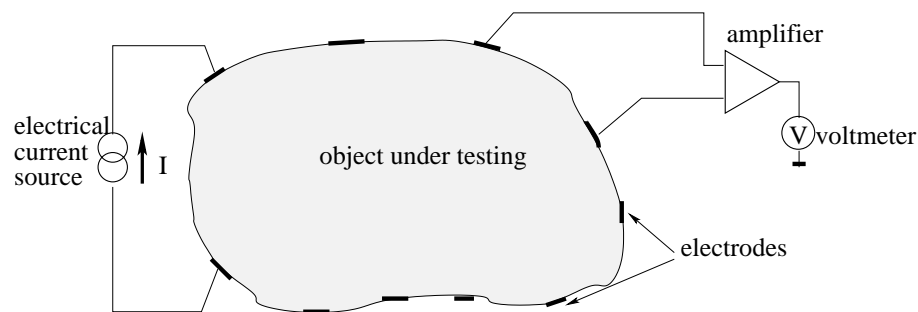


Figure 1.4: Principle of the electrical impedance tomography (EIT).

EIT has a wide applications field from medicine to process control. In medicine the knowledge of internal electrical properties of the body can be useful in the detection of pulmonary emboli, blood cloths in the lungs [14] or blood flow imaging [9]. Air, tissue and blood have very different electrical properties. Therefore it is no problem to map electrical properties and the internal structure of the body with methods of EIT. There exists also non-clinical applications of EIT, such as the imaging of multiphase flow [70], [67], [28]. Butler at al. [12] have shown the possibility to determine particle migration for the pressure-driven pipe flow with the help of EIT. Other applications of EIT are the determination of mineral resources in the earth [20], [50], tracing the spread of contaminants in the earth [53], [54],

[16] and semiconductor wafer characterization [21]. Many methods and algorithms based on EIT are patented. Appendix **B** contains brief descriptions of some of them.

### 1.3.3 Inverse problems: definitions and classification.

An *inverse problem* takes place if the physical quantity or information can not be directly measured, but has to be determined from the interaction of this information or quantity [43]. Applying this to the reconstruction problems presented in the thesis, the interface shape between aluminium and cryolite is not directly measurable. Instead it is reconstructed from physical quantities, which are influenced by the interface, namely the magnetic field outside the Alu-cell or the electrical potential on the cell boundaries. The *forward problem* can be described as direct computation of some physical quantity if the model and parameters are known. The *forward problem* is the *effect of the cause*, and in contrary to this the *inverse problem* is the *cause of the effect*.

In general the discrete linear inverse problem which is treated in this work can be described by a matrix equation

$$\mathbf{Ax} = \mathbf{y} \tag{1.2}$$

where  $\mathbf{y}$  is a set of measurement data with errors, matrix  $\mathbf{A}$  depicts some *forward* model which is known. The unknown is the vector of "parameters"  $\mathbf{x}$ . The solution of the forward problem is always unique. The solution of the inverse problem is often unstable. A small measurement error in the data set  $\mathbf{y}$  induces a significant error in the determined parameter vector  $\mathbf{x}$ . Such problems are called ill-posed. A well-posed problem is presented if eq. (1.2) has a solution, this solution is unique, and this solution depends continuously from the data [43]. If one of this conditions is not valid, the problem is ill-posed.

The solution methods for inverse problems can be classified into two large groups: deterministic methods (cross-validation [31], gradients methods [49], truncated singular value decomposition [30], [52], Tikhonov-Philips regularization [65]) and stochastic methods (simulated annealing [40], evolutionary and genetic algorithms [55], [1], [29], Monte-Carlo methods) to name only a few.

The solution of an ill-posed inverse problem is an optimization problem and it can be described as the finding of the compromise between experimental data and model which describes this data. For estimation of the model the *a priori* known information is used. For example, in the case of interface reconstruction described in the thesis it is the smoothness of the reconstructed interface.

In this thesis the truncated singular value decomposition is used for interface reconstruction from electrical potential measurements (see chapter 3). This is a standard technique for solving optimization problems in the least squares sense, i.e. minimization of the norm

$$\| \mathbf{Ax} - \mathbf{y} \| = 0.$$

The algorithm of the solution of the inverse problem is described in chapter 3.

## 1.4 Reconstruction of interfaces in aluminium reduction cells using magnetic field measurements

Another possibility to reconstruct the interface in an aluminium reduction cell is to recover it from the magnetic field. The total magnetic field is produced as result of the electrical currents flowing in the Alu-cell. It can be represented as the sum

$$\mathbf{B} = \mathbf{B}_0 + \mathbf{b}$$

where  $\mathbf{B}_0$  is main magnetic field and  $\mathbf{b}$  is the magnetic field perturbation.  $\mathbf{B}_0$  is resulted from the main electrical current  $\mathbf{J}_0 = J_0 \mathbf{e}_z$  which is applied between cathode and anode. The perturbation of magnetic field appears if the interface between cryolite and aluminium is wavy, i.e. it is displaced from its flat shape. In this case it takes place the perturbation of electrical current  $\mathbf{j}$  which leads to the perturbation of the magnetic field  $\mathbf{b}$  which is used for the reconstruction.

The idea to use magnetic field measurements to reconstruct internal structures in the body under testing is not new. The measurement of weak magnetic fields on the human body are used in magnetic field tomography to reconstruct internal

current sources in the body [34]. The authors differ between magnetocardiography (MCG) which is the measurement of the heart activity and magnetoencephalography (MEG), which investigates the human brain activity. These studies are often called magnetic source imaging or current-flow imaging. Reviews on MEG methods are given in [68],[69], [56] and [35].

The measurement of very weak ( $\sim 10^{-11} \dots 10^{-13} T$ ) biomagnetic fields of a human body is still a challenge. It requires the use of special hardware, which is able to measure the magnetic fluxes from a femtotesla (fT) up to a pikotesla (pT) [22]. For this purpose the SQUIDs (a superconducting loop interrupted by two Josephson junctions [15]) are widely used. Usually the special shielded rooms [34] for suppression of noises and special measurement techniques are required. The practical implementations, measurement techniques and algorithms of reconstruction are given by Brauer *et al.* [5], [6], [7]. In these studies the biomagnetic measurements are performed on a physical thorax phantom using the 2x31 SQUID system. Biomagnetic currents are modelled with current sources in the torax. The measured magnetic field is used for reconstruction of current inside the torax and compared with a prescribed sources.

The reconstruction methods successfully applied in biomagnetismus are not limited to purely clinical applications. In many technological applications using very hot /or aggressive fluids (crystal growth, metal casting) the determination of velocity fields depicts a serious problem. The use of standard techniques via pressure probes, hot wire probes, mechano-optical probes provide only the local velocity information near the probe itself [61]. The use of ultrasound beams or x-rays require scattering obstacles in the melt. Contrary to this approaches, the reconstruction of velocity field using magnetic field measurement is a non-intrusive technique giving the complete 3D velocity field. This method was first introduced by Baumgartl *et al.* [2]. In this paper the fluid was placed into an external magnetic field, which induces the electrical currents in the fluid. This currents produce the secondary magnetic field inside and outside the fluid volume. It was postulated that some information about the velocity field can be extracted from the secondary magnetic field. Similar considerations were made by Kasuga *et al.* [39]. In contrary to the previous work the authors have restricted their interest to the reconstruction

of the electrical currents in an conducting fluid (usually a melt). The determination of the velocity field from magnetic field is considered in [3] and [61]. These papers deal with the inverse problem in more detail.

In [3] and [61] it was shown, that generally the reconstruction from magnetic field without additional information is not uniquely. In 1853 it was shown by Helmholtz [36] that an electric current could not to be uniquely reconstructed from magnetic field outside the conductor. There are the current distributions which are magnetically silent ( $\mathbf{B} = 0$  outside of conductor). The simplest example of such distribution is the radial dipole in a spherically symmetric conductor. The solution of this problem consists on the using of additional information. Berkov and Gorn [3] have proposed for this purpose to apply the magnetic field on the body under investigation in different directions and to measure the secondary magnetic field. Stefani and Gerbeth [61] includes the potential measurement at the boundary as additional information in reconstruction algorithm and they achieve good accuracy. In later work [62] the another idea is used to make the reconstruction uniquely: a "regularizing functional" for the wanted velocity which points out the minimization of kinetic energy for moving fluid is introduced. However, this analysis is restricted to the special case of spherical geometry and homogeneous external magnetic field. The experimental validation of methods introduced by Stefani *et al.* was performed in [63], where the three-dimensional velocity field of a propeller driven liquid metal flow is reconstructed by applying two external orthogonal magnetic fields and measurements of the secondary magnetic fields.

Unfortunately the reconstruction from magnetic field in Alu-cells will also produce some difficulties. In case of an Alu-cell there exists a class of interfaces which do not produce any changing of magnetic field outside the Alu-cell. These are axisymmetrical interfaces, which produce axisymmetric current perturbations. An axisymmetrical current perturbations does not induce any magnetic field perturbation outside the cylinder. Therefore from the magnetic field measurements one can recover only the non-axisymmetric interfaces. To avoid this limitation the potential perturbation measurement with reconstruction algorithm shown in chapter 3 can be used.

The solution of the inverse problem for interface reconstruction from the mag-

netic field measurement is beyond the scope of this work. In this thesis only the solution of the forward problem for the reconstruction of the aluminium-cryolite interface from the magnetic field will be treated.

# Chapter 2

## Stability of aluminium reduction cells with mean flow\*

### 2.1 Statement of the problem

The simplified model of an aluminum reduction cell sketched in Fig. 2.1 is considered. The cryolite layer is superposed over the aluminum in an infinite horizontal channel of width  $L$ . It is assumed that both fluids are inviscid. The flow in the aluminum is supposed to be uniform  $\mathbf{U}_a = U_0 \mathbf{e}_x$ . The cryolite is initially at rest. A vertical homogeneous magnetic field  $\mathbf{B}_0 = B_0 \mathbf{e}_z$  and a homogeneous electric current  $\mathbf{J}_0 = -J_0 \mathbf{e}_z$  are applied. For the sake of the model simplicity the chemical processes such as generation of carbon dioxide bubbles in the reaction between the carbon anode and oxygen are not considered.

---

\*This chapter is based on the *extended version* of the paper "Stability of aluminium reduction cells with mean flow". A.Kurenkov, A.Thess, O.Zikanov, M.Segatz, Ch.Droste, D. Vogelsang. *Magnetohydrodynamics* **40**, 2 (2004).

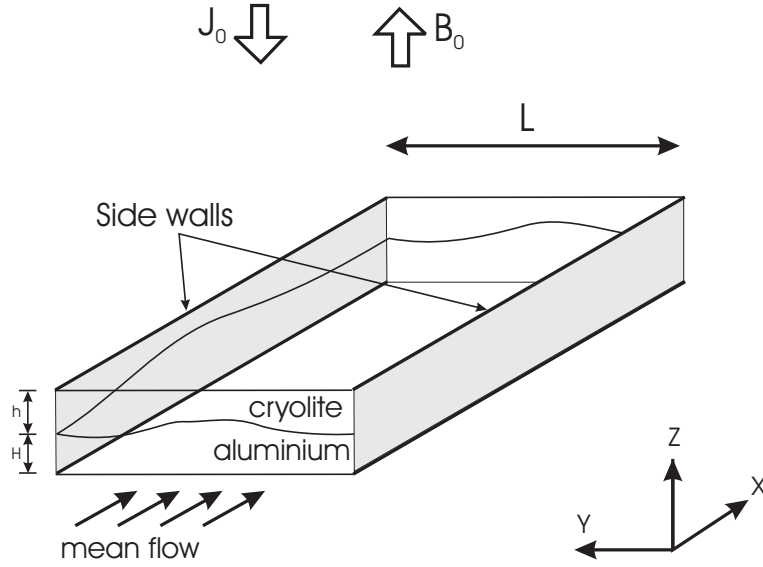


Figure 2.1: Schematic representation of the model. In the basic steady state, a uniform flow (mean flow) in the aluminum is assumed, while the cryolite is supposed to be at rest.

## 2.2 Basic equations

### 2.2.1 Governing equations and basic flow

Our model is based on the shallow water approximation [51]. The approximation rests on the assumption that the layer thicknesses are small, i.e.,

$$h, H \ll L, \lambda, \quad (2.1)$$

where  $\lambda$  is the typical length scale of interfacial perturbations, and  $h$  and  $H$  are the thicknesses of cryolite and aluminium layers, respectively.

Taking into account the Lorentz force in the aluminum  $\mathbf{F}_a = -\sigma_a B_0 \nabla_{\perp} \phi$  due to the interaction of the electric current perturbation  $\mathbf{j}_a = -\sigma_a \nabla \phi$  with the magnetic field  $B_0 \mathbf{e}_z$ , the nonlinear shallow water equations governing the fluid motions can be written as [71]

$$\frac{\partial \mathbf{u}_a}{\partial t} + (\mathbf{u}_a \cdot \nabla) \mathbf{u}_a = -\frac{\nabla p}{\rho_a} - g \nabla \eta - \sigma_a \frac{B_0}{\rho_a} \nabla_{\perp} \phi \quad (2.2)$$



$$\frac{\partial \mathbf{u}_c}{\partial t} + (\mathbf{u}_c \cdot \nabla) \mathbf{u}_c = -\frac{\nabla p}{\rho_c} - g \nabla \eta \quad (2.3)$$

$$\frac{\partial \eta}{\partial t} + \nabla \cdot [(H + \eta) \mathbf{u}_a] = 0 \quad (2.4)$$

$$\nabla \cdot [(H + \eta) \mathbf{u}_a + (h - \eta) \mathbf{u}_c] = 0 \quad (2.5)$$

$$\nabla^2 \phi = -\frac{J_0 \eta}{\sigma_a H h} \quad (2.6)$$

where  $\nabla_{\perp} = \mathbf{e}_x \partial / \partial y - \mathbf{e}_y \partial / \partial x$ . The shallow-water approximation eliminates the  $z$ -dependence, so all equations are two-dimensional. Indices "a" and "c" refer to aluminum and cryolite respectively.  $\mathbf{u}_a(x, y, t)$  and  $\mathbf{u}_c(x, y, t)$  are the vertically averaged horizontal velocities in corresponding layers,  $p(x, y, t)$  is the pressure at the interface  $z = \eta(x, y, t)$ , and  $\phi(x, y, t)$  is the perturbation of the electrical potential. In the system (2.2) - (2.6), equations (2.2) and (2.3) are the momentum equations, (2.4) describes evolution of the interface, (2.5) imposes the mass conservation condition, and (2.6) provides the link between the deflection of interface and perturbations of electrical current.

The boundary conditions are

$$u_{ay} = u_{cy} = \frac{\partial \phi}{\partial y} = 0 \quad \text{at } y = 0 \text{ and } y = L \quad (2.7)$$

The first two conditions are the conventional free slip conditions at the channel walls, while the last condition describes electrically non-conducting channel walls.

Equations (2.2-2.6) admit an exact stationary solution

$$\mathbf{u}_a = U_0 \mathbf{e}_x, \quad \mathbf{u}_c = 0, \quad p = \eta = \phi = 0 \quad (2.8)$$

whose stability with respect to infinitesimal perturbations we wish to investigate.

### 2.2.2 Evolution of small perturbations

We consider small perturbations  $\mathbf{v}_a$ ,  $\mathbf{v}_c$ ,  $p$ ,  $\eta$ ,  $\phi$  superimposed upon the basic state (2.8). The linearized equations for the evolution of these perturbations are readily

obtained from (2.2)-(2.6) as

$$\frac{\partial \mathbf{v}_a}{\partial t} + U_0 \frac{\partial \mathbf{v}_a}{\partial x} = -\frac{\nabla p}{\rho_a} - g\nabla\eta - \frac{\sigma_a B_0}{\rho_a} \nabla_{\perp} \phi \quad (2.9)$$

$$\frac{\partial \mathbf{v}_c}{\partial t} = -\frac{\nabla p}{\rho_c} - g\nabla\eta \quad (2.10)$$

$$\frac{\partial \eta}{\partial t} + U_0 \frac{\partial \eta}{\partial x} + H\nabla \cdot \mathbf{v}_a = 0 \quad (2.11)$$

$$U_0 \frac{\partial \eta}{\partial x} + H\nabla \cdot \mathbf{v}_a + h\nabla \cdot \mathbf{v}_c = 0 \quad (2.12)$$

$$\nabla^2 \phi = -\frac{J_0 \eta}{\sigma_a H h} \quad (2.13)$$

Defining  $\chi = \nabla \cdot \mathbf{v}$  and  $\omega = -\nabla_{\perp} \cdot \mathbf{v}$ , applying the operators  $\nabla \cdot$  and  $-\nabla_{\perp} \cdot$  to (2.9) and (2.10), the first four equations are transformed into

$$\frac{\partial \chi_a}{\partial t} + U_0 \frac{\partial \chi_a}{\partial x} = -\frac{\nabla^2 p}{\rho_a} - g\nabla^2 \eta \quad (2.14)$$

$$\frac{\partial \chi_c}{\partial t} = -\frac{\nabla^2 p}{\rho_c} - g\nabla^2 \eta \quad (2.15)$$

$$\frac{\partial \omega_a}{\partial t} + U_0 \frac{\partial \omega_a}{\partial x} = \frac{\sigma_a B_0}{\rho_a} \nabla^2 \phi \quad (2.16)$$

$$\frac{\partial \omega_c}{\partial t} = 0 \quad (2.17)$$

$$\frac{\partial \eta}{\partial t} + U_0 \frac{\partial \eta}{\partial x} + H\chi_a = 0 \quad (2.18)$$

$$U_0 \frac{\partial \eta}{\partial x} + H\chi_a + h\chi_c = 0 \quad (2.19)$$

The system can be further simplified by eliminating the pressure in (2.14) using (2.15), by eliminating  $\chi_c$  using (2.19), and by noting that  $\omega_c = 0$ , if the vorticity of the cryolite is zero in the initial condition. Furthermore, equation (2.16) is not necessary to determine the stability threshold since  $\omega_a$  is decoupled from the rest of the system. Finally, we obtain three equations

$$H\bar{\rho} \frac{\partial \chi_a}{\partial t} + \rho_a U_0 \frac{\partial \chi_a}{\partial x} = -g\Delta\rho \nabla^2 \eta - \frac{\rho_c U_0}{h} \frac{\partial^2 \eta}{\partial x \partial t} \quad (2.20)$$

$$\frac{\partial \eta}{\partial t} + U_0 \frac{\partial \eta}{\partial x} + H \chi_a = 0 \quad (2.21)$$

$$\nabla^2 \phi = -\frac{J_0 \eta}{\sigma_a H h} \quad (2.22)$$

for the divergence of the aluminum flow  $\chi_a$ , the interface deflection  $\eta$  and the electric potential  $\phi$ . Here we define  $\bar{\rho} = (\rho_a/H) + (\rho_c/h)$  and  $\Delta\rho = \rho_a - \rho_c$ . To derive a boundary condition for  $\eta$  we take the y-components of (2.9) and (2.10), use the first two conditions of (2.7) and eliminate the pressure obtaining

$$g\Delta\rho \frac{\partial \eta}{\partial y} = \sigma_a B_0 \frac{\partial \phi}{\partial x} \quad \text{at } y = 0 \text{ and } y = L. \quad (2.23)$$

This condition together with the boundary condition (2.7) for the electric potential and the stability equations (2.20)-(2.22) completes the formulation of the linear stability problem. It will be seen later that no boundary condition for  $\chi_a$  is necessary.

### 2.2.3 Normal mode analysis and stability equations

We decompose the perturbation into normal modes according to

$$\begin{aligned} \chi_a &= \hat{\chi}_a(y) \exp[ik(x - ct)], \\ \phi &= \hat{\phi}(y) \exp[ik(x - ct)], \\ \eta &= \hat{\eta}(y) \exp[ik(x - ct)]. \end{aligned} \quad (2.24)$$

Substitution (2.24) into (2.20)-(2.22) gives

$$ik(-\bar{\rho}Hc + \rho_a U_0) \hat{\chi}_a = -g\Delta\rho(D^2 - k^2) \hat{\eta} - ck^2 U_0 \frac{\rho_c}{h} \hat{\eta} \quad (2.25)$$

$$ik(-c + U_0) \hat{\eta} = -H \hat{\chi}_a \quad (2.26)$$

$$(D^2 - k^2) \hat{\phi} = -\frac{J_0 \hat{\eta}}{\sigma_a H h} \quad (2.27)$$

where  $D = \partial/\partial y$ .

In (2.25),  $\chi_a$  can be eliminated using (2.26), which reduces the stability problem

to the two ordinary differential equations

$$\left\{ \left( \frac{g\Delta\rho}{\bar{\rho}k^2} \right) (D^2 - k^2) + c^2 - 2cU_0 \left( \frac{\rho_a}{\bar{\rho}H} \right) + U_0^2 \left( \frac{\rho_a}{\bar{\rho}H} \right) \right\} \hat{\eta} = 0 \quad (2.28)$$

$$\sigma_a H h (D^2 - k^2) \hat{\phi} + J_0 \hat{\eta} = 0 \quad (2.29)$$

and the boundary conditions

$$g\Delta\rho D\hat{\eta} - ik\sigma_a B_0 \hat{\phi} = D\hat{\phi} = 0 \quad \text{at } y = 0 \text{ and } y = L \quad (2.30)$$

The stability problem (2.28)-(2.30) determines the complex wave speed  $c(U_0, B_0, J_0, k) = c_r + ic_i$  of stable ( $c_i < 0$ ) or unstable ( $c_i > 0$ ) perturbations. The condition  $c_i(U_0, B_0, J_0, k) = 0$  corresponds to the marginal stability state.

## 2.2.4 Non-dimensional parameters

We convert the stability problem (2.28) - (2.30) to a non-dimensional form by introducing the new variables  $y_*, k_*, D_*, c_*, \hat{\eta}_*, \hat{\phi}_*$  via  $y_* = y/H$ ,  $k_* = kH$ ,  $D_* = HD$ ,  $c_* = c/c_0$ ,  $\hat{\eta}_* = \eta/H$ ,  $\hat{\phi}_* = \hat{\phi}\sigma_a h/(H^2 J_0)$ . Here  $c_0 = g(\rho_a - \rho_c)/(\rho_a/H + \rho_c/h)$  is the propagation speed of internal gravity waves on the interface. Upon introduction of these new quantities into the stability problem the following dimensionless parameters appear.

$$M = \frac{U_0}{c_0}$$

is the dimensionless velocity of the mean flow.

$$N = \frac{J_0 B_0 H}{(\rho_a - \rho_c) g h}$$

is the main stability parameter. It describes the ratio between destabilizing electromagnetic forces and the stabilizing influence of gravity. The parameter

$$\xi = \frac{1}{1 + \frac{\rho_c H}{\rho_a h}}$$

contains the thicknesses of the fluid layers and densities of the fluids. Finally,

$$A = \frac{L}{H}$$

is the aspect ratio.

After rearrangement and dropping the asterisk the stability problem takes the dimensionless form

$$[(D^2 - k^2) + k^2(c^2 - 2cM\xi + M^2\xi)]\hat{\eta} = 0 \quad (2.31)$$

$$(D^2 - k^2)\hat{\phi} + \hat{\eta} = 0 \quad (2.32)$$

with the boundary conditions

$$D\hat{\eta} - iNk\hat{\phi} = D\hat{\phi} = 0 \quad \text{at } y = 0 \text{ and } y = A \quad (2.33)$$

Our goal is to compute the dispersion relation  $c(M, N, \xi, A, k)$ . In the following consideration we use only dimensionless variables and drop the asterisk.

## 2.3 Solution of the stability problem

We start with the numerical solution of the general problem, in which both Kelvin-Helmholtz and MHD instabilities are present. Then, it will be shown that, in the case of pure Kelvin-Helmholtz instability (zero Lorentz force), the stability problem has an analytical solution.

### 2.3.1 The general case: Interaction between MHD-instability and Kelvin-Helmholtz instability

Let us introduce the abbreviations

$$\kappa^2 = k^2(c^2 - 2\xi Mc - 1 + \xi M^2), \quad p = \kappa A/2, \quad q = kA/2 \quad (2.34)$$

and write the phase velocity of perturbations as

$$c = \xi M \pm \sqrt{1 - M^2(\xi - \xi^2) + \kappa^2/k^2} \quad (2.35)$$

Then the stability system (2.31-2.33) becomes

$$(D^2 + \kappa^2)\hat{\eta} = 0 \quad (2.36)$$

$$(D^2 - k^2)\hat{\phi} + \hat{\eta} = 0 \quad (2.37)$$

$$D\hat{\eta} - ikDa\hat{\phi} = D\hat{\phi} = 0 \quad \text{for } y = \pm A/2 \quad (2.38)$$

Here, the  $y$ -coordinate is shifted in such a way, that the centerline of the channel is located at  $y = 0$ . The general solutions of (2.36) and (2.37) are

$$\hat{\eta} = C_1 \cos \kappa y + C_2 \sin \kappa y \quad (2.39)$$

$$\hat{\phi} = \frac{C_1 \cos \kappa y}{\kappa^2 + k^2} + \frac{C_2 \sin \kappa y}{\kappa^2 + k^2} + C_3 \cosh ky + C_4 \sinh ky \quad (2.40)$$

where  $C_1, C_2, C_3, C_4$  are unknown coefficients. We apply the boundary conditions (2.38) and obtain a system of four linear equations with four unknown variables  $C_1, C_2, C_3, C_4$ . After some algebraic transformation, it can be reduced to

$$\underbrace{\begin{pmatrix} \kappa \sin p & \frac{iN}{\kappa^2+k^2}[k \sin p - \kappa \cos p \tanh q] \\ \frac{iN}{\kappa^2+k^2}[k \cos p + \kappa \sin p \coth q] & \kappa \cos p \end{pmatrix}}_{\mathbf{Q}} \begin{pmatrix} C_1 \\ C_2 \end{pmatrix} = 0 \quad (2.41)$$

This system has a non-trivial solution only if the determinant of the matrix  $\mathbf{Q}$  is equal to zero. We find the corresponding value of  $\kappa$  numerically, varying  $\kappa$  and calculating  $\det[\mathbf{Q}]$  at a given  $N$ . After the eigenvalue is found, we use (2.35) to obtain the complex velocity  $c(M, N, \xi, A, k) = c_r + ic_i$  of stable ( $c_i < 0$ ) or unstable ( $c_i > 0$ ) oscillations.

For the states of marginal stability ( $c_i = 0$ ) we obtain the expressions for the interface shape  $\eta(x, y, t)$  and the electrical potential perturbation  $\phi(x, y, t)$  as

$$Re[\eta(x, y, t)] = Re\{\hat{\eta}(y) \exp[ik(x - ct)]\} \quad (2.42)$$

$$Re[\phi(x, y, t)] = Re\{\hat{\phi}(y) \exp[ik(x - ct)]\} \quad (2.43)$$

where  $\hat{\eta}(y)$  and  $\hat{\phi}(y)$  are corresponding eigensolutions (2.39) and (2.40).

### 2.3.2 The particular case of a pure Kelvin-Helmholtz instability ( $N = 0$ )

In the case  $N = 0$  (which corresponds to  $J_0 = 0$  or  $B_0 = 0$ ) we deal with pure Kelvin-Helmholtz instability. The destabilizing Lorentz forces are non-existent in this case. The mean flow becomes unstable if its velocity exceeds a certain critical value. Here, we will obtain the analytical expression for the critical mean flow velocity.

Inserting  $N = 0$  in system (2.41) we obtain the equation for  $\kappa$

$$\kappa^2 \sin(2p) = 0 \quad (2.44)$$

whose solutions are

$$\kappa = \pi n/A \quad n = 0, 1, \dots \quad (2.45)$$

The complex velocity of perturbations can be easily obtained from equation (2.35) as

$$c = \xi M \pm \sqrt{1 - M^2(\xi - \xi^2) + \frac{\pi^2 n^2}{k^2 A^2}} \quad (2.46)$$

The stability threshold is defined as

$$M = \sqrt{\frac{1 + \frac{\pi^2 n^2}{k^2 A^2}}{\xi - \xi^2}}. \quad (2.47)$$

We define the critical mean flow velocity  $M_c$  as the smallest  $M$ , for which the instability appears for an arbitrary wavenumber  $k$ . It is clear from the last equation that  $M_c$  is to be computed by setting  $n = 0$  as

$$M_c = \sqrt{\frac{1}{\xi - \xi^2}}. \quad (2.48)$$

### 2.3.3 The particular case of a pure MHD instability ( $M = 0$ )

The case of pure MHD-instability corresponds to the situation of zero mean flow ( $M = 0$ ) when the fluids are initially at rest. In this case, equation (2.35), which determines the complex speed of interfacial perturbations, simplifies to

$$c = \pm \sqrt{1 + \kappa^2/k^2} \quad (2.49)$$

The complex parameter  $\kappa$  has to be computed numerically from the condition  $\det[\mathbf{Q}] = 0$  [cf. Eq. (2.41)].

From the condition of instability  $\text{Im}[c] > 0$  it is clear that the instability sets in if the parameter  $\kappa$  has non-zero imaginary part. Real  $\kappa$  corresponds to stable states.

We investigated the stability numerically starting with the stable state (real values of  $\kappa$  for all wavenumbers  $k$ ) at  $N = 0$  and increasing  $N$  so that we could find the critical parameter  $N_c$ , at which  $\kappa$  moves off into the complex plane. As will be discussed in section 2.4,  $N_c$  is to be obtained for  $k \rightarrow 0$ , i.e, the most unstable waves are infinitely long waves.

## 2.4 Results

The results of the stability analysis described in this section can be summarized as follows. Both the mean flow and electromagnetic fields can trigger its own instability but neither of them affects the threshold of instability caused by the other mechanism. The only mutual impact is through the modification of the phase velocity of unstable and stable modes.

### 2.4.1 The general case: MHD-Instability and Kelvin-Helmholtz instability

It was discussed in section 2.3 that the instability develops through two different mechanisms: Kelvin-Helmholtz instability and MHD instability. The main parameter of the Kelvin-Helmholtz instability is the non-dimensional critical mean flow velocity  $M_c$ . The main parameter of the MHD instability is  $N_c$ . The basic state is stable if  $N < N_c$  and  $M < M_c$  and unstable otherwise. The main result is that



both stability limits are independent, i.e.  $M_c$  does not depend on  $N$  and  $N_c$  does not depend on  $M$ . We can explain this fact as follows. The instability sets in if the complex part of the phase velocity of perturbations, which is determined by Eq. (2.35), becomes negative. It happens if  $M > M_c$  or  $\kappa$  is complex. The eigenvalues  $\kappa$  are real at small  $N$  (at  $N = 0$  they are computed analytically, s. Eq. (2.45)) and then with increasing of  $N$  they move off into the complex plane (at  $N = N_c$ ). It can be also seen from the system (2.41) that  $\kappa$  depends only on  $N$  and does not depend on  $M$ . Therefore  $N_c$  is independent of  $M$ . On the other side,  $M_c$ , which is given by (2.48), does not depend on  $N$ . We conclude, that the stability limits  $M_c$  and  $N_c$  are independent from each other.

Figure 2.2(a) shows the stability chart. The marginal stability curve consists of the two independent stability thresholds,  $N = N_c$  and  $M = M_c$ . Each inner point in the region  $N < N_c$  and  $M < M_c$  means stability contrary to the outer points which mean instability. The stability threshold  $N_c$  depends on the aspect ratio  $A$  and was computed numerically.  $M_c$  was computed by Eq. (2.48) and depends on parameter  $\xi$ . It can also be seen in Fig. 2.2(a), that with increasing aspect ratio  $A$  (corresponding to increasing channel width) the stability region decreases. This means that the waves in a narrow channel are more stable than waves in a wide channel. Another possible reason for the contraction of the stability region is the decrease of  $\xi$ , which may be caused by increasing the ratio  $H/h$ , where  $H$  is the aluminum depth and  $h$  is cryolite depth.

The mean flow plays not only a destabilizing role in our model, but it also modifies the frequencies of the interfacial waves. Fig. 2.2(b) shows the frequencies of interface oscillations at different mean flow velocities. At  $M = 0$ , two symmetrical waves are moving in opposite directions. With increasing of  $M$ , one of the waves changes the travelling direction to the opposite. For large  $M$ , both waves move in the same direction as the mean flow.

### 2.4.2 The particular case of a pure Kelvin-Helmholtz Instability

For this case, the marginal stability curve has to be computed from Eq. (2.47). The stability threshold depends on  $k$ ,  $\xi$ ,  $A$ , and the transverse wavenumber  $n$ .

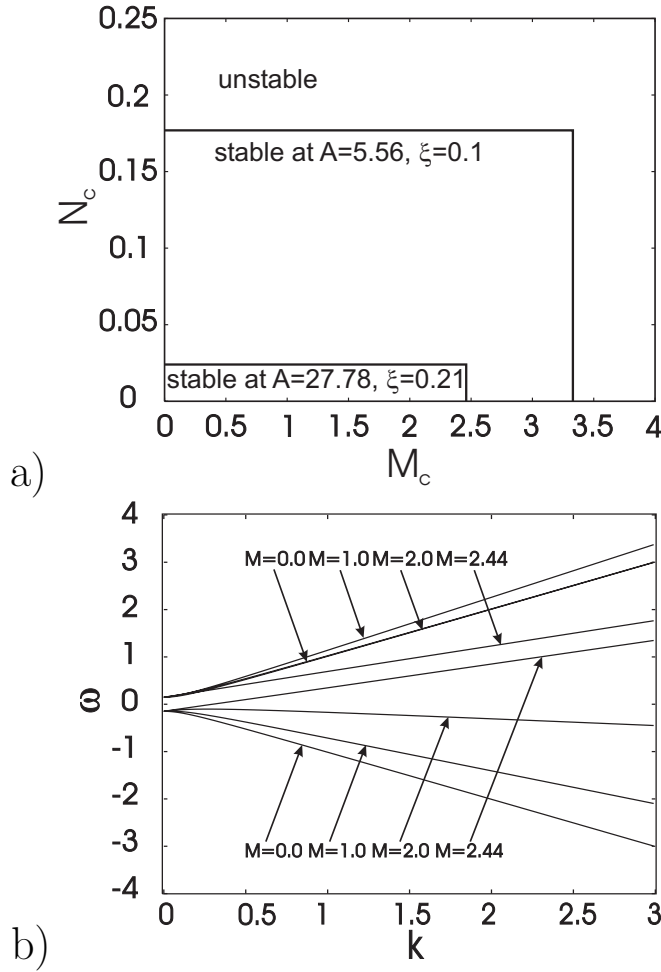


Figure 2.2: Stability results for the general case. (a) Stability chart for selected values of  $\xi$  and  $A$ . (b) Frequencies of interface perturbations for different values of  $M$  in the state of marginal stability.  $\xi = 0.2132, A = 14.95$ .

For  $M < M_c$ , Eq. (2.46) only gives real solutions, which describe two stable waves moving upstream or downstream respectively. As the mean flow velocity  $M$  exceeds  $M_c$ , one of the waves changes its propagation direction. Figure 2.3(a) shows the marginal stability curves for the two modes with transverse wavenumber  $n = 0$  and  $n = 1$ . The mode with  $n = 0$  depends only on  $x$ , while mode with  $n = 1$  depends on both coordinates  $x$  and  $y$  (cf. inserts on Fig. 2.3(a)). We see that the one-dimensional mode ( $n = 0$ ) is the most unstable mode for any wavenumber  $k$  and the critical mean flow velocity  $M_c$  is defined by the stability of mode with  $n = 0$  and is given by Eq.(2.48).

Instability limits with respect to the higher modes with  $n \geq 1$  depend on the

longitudinal wavenumber  $k$  (see Fig. 2.3(a)). For these modes the short waves are more unstable than the long waves.

Figure 2.3(b) shows the frequencies of interface oscillations at the marginal stability state, at  $M = M_c$ .

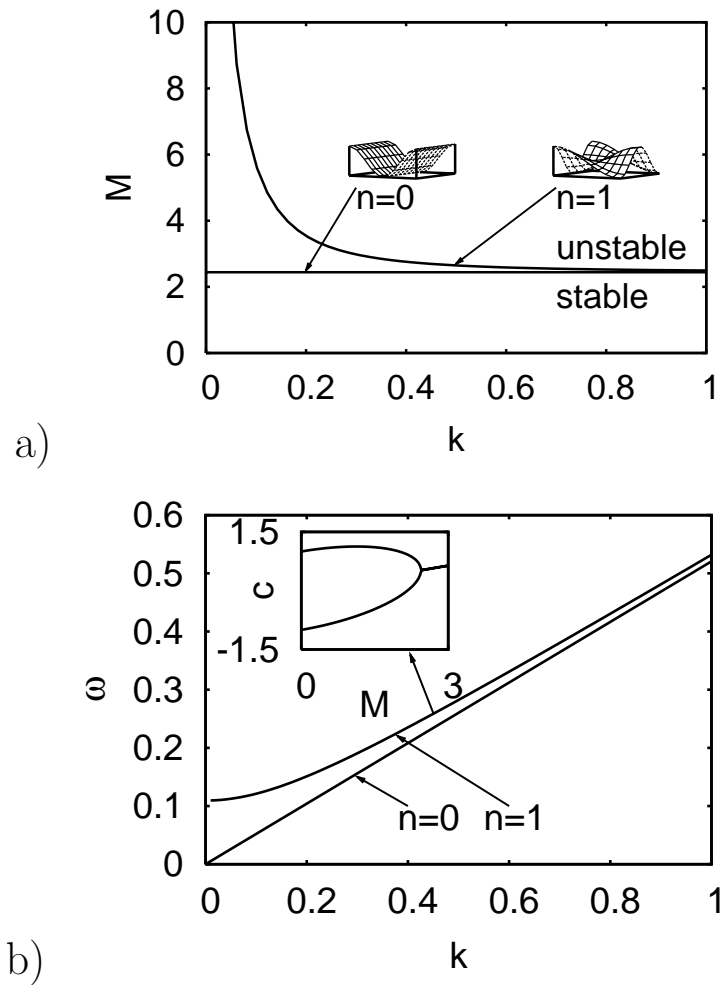


Figure 2.3: Stability results for the particular case of a pure Kelvin-Helmholtz instability ( $N = 0$ ). (a) Marginal stability curves for the two first transverse modes:  $n = 0$  and  $n = 1$ . Inserts show the interfaces for  $0 < x < 2L$ ,  $0 < L < y$ . (b) Frequency of interface perturbations  $\omega$  in the marginally stable state ( $M = M_c$ ) as a function of longitudinal wavenumber  $k$  and for  $\xi = 0.2132$ ,  $A = 14.95$ . The insert shows the wave speed as a function of  $M$  for  $k = 0.5$ .

### 2.4.3 The particular case of a pure MHD Instability

This case (characterized by  $M = 0$ ) was considered by Davidson & Lindsay [18]. However, the dependence of  $N_c$  on  $\xi$  and  $A$  was not discussed there. Figure 2.4 presents the family of stability curves for different aspect ratios  $A$  as obtained from our numerical computation. The instability sets in at the threshold value of  $N$  that depends on the wavenumber  $k$ . Our computations show that, for the MHD-instability, the short waves are more stable in comparison to the long waves.

An increase of the aspect ratio  $A$  leads to the reduction of the instability threshold for all  $k$ . It can be shown, that, for  $A \rightarrow \infty$  (only one wall),  $N_c \rightarrow 0$ .

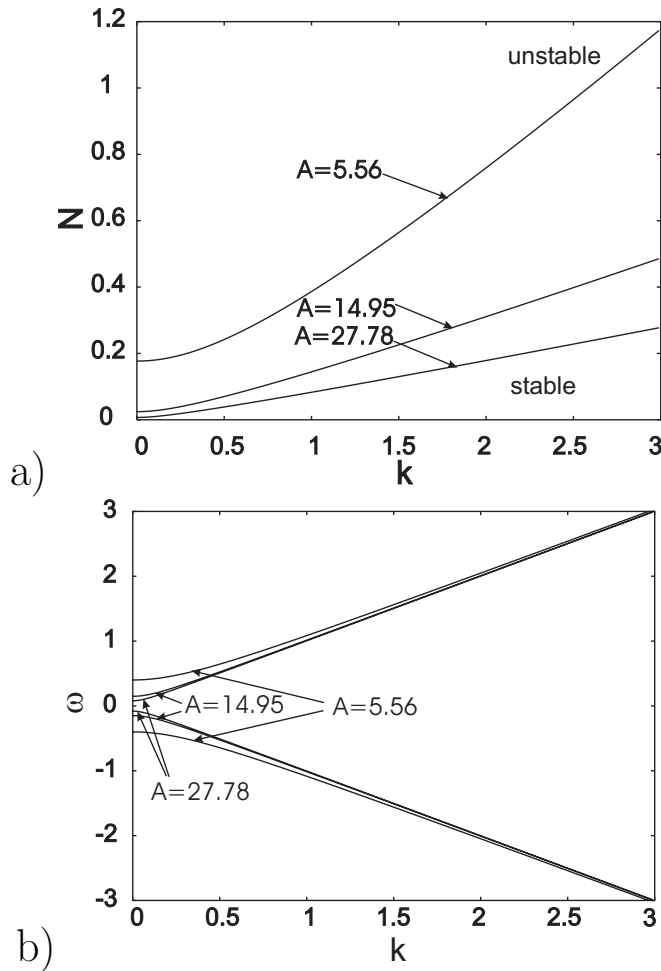


Figure 2.4: Stability results for the particular case of a pure MHD-Instability ( $M = 0$ ). a) Marginal stability curves for the different aspect ratios  $A$ . b) Frequencies of interface perturbations in the marginal stability state.

The mechanism of instability onset is very interesting. In the absence of the

Lorentz force there exist gravitational modes with different transverse wavenumber  $n$ . The key to the understanding of the instability onset is the interaction of two modes with  $n = 0$  [see Fig. 2.5 (a)] and  $n = 1$ . As  $N$  increases the mode with  $n = 0$  changes its shape under the influence of the Lorentz force [see Fig.2.5 (b)]. This new mode has the transverse wavenumber  $n = 1$  and its shape is identical to those of the existing gravitational mode with  $n = 1$ . Its oscillation frequency, however, is at small  $N$  different from that of the "old" gravitational mode with  $n = 1$ . If  $N$  further increases, the two complex frequencies of "new" and "old" modes with  $n = 1$  converge on the real axis. At  $N = N_c$ , the two frequencies coincide and move off into the complex plane resulting into one unstable and one stable mode.

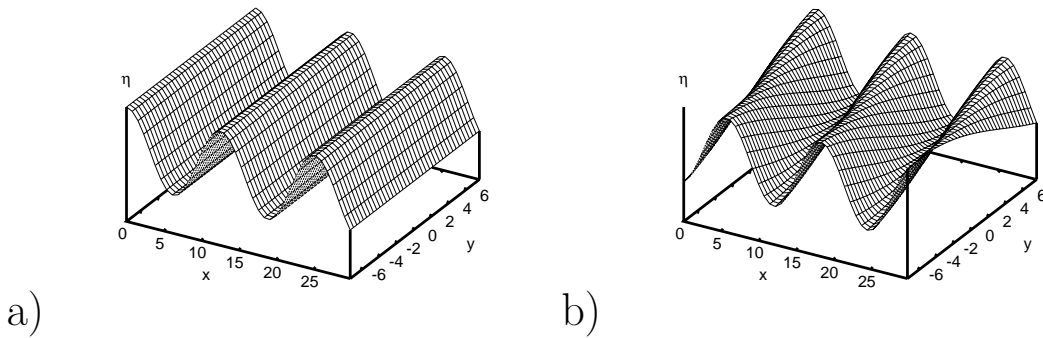


Figure 2.5: Mechanism of instability onset in the channel. a)  $N = 0$ , the spatial shape of the one-dimensional gravitational mode is not deformed b)  $N > 0$ , the one-dimensional mode is deformed by Lorentz forces. It destabilizes the existing gravitational mode, if the frequencies of both coincide.

A similar instability scenario was described by Davidson & Lindsay [18] for the mechanical counterpart of the system (the so-called compound pendulum). In their model, two arbitrary gravitational modes are modified by the Lorentz force so their complex frequencies coincide on the real axis and then move off into the complex plane. Contrary to the pendulum model we do not observe the interaction between any other modes than the two with  $n = 0$  and  $n = 1$ . This can be explained by the fact, that the pendulum model explains the instabilities in a rectangular cell with finite dimensions while our model deals with an infinitely long channel.

## 2.5 Summary and conclusion

We have presented a simplified model of an aluminum reduction cell with an uniform mean flow in aluminum layer. Two major sources of instability, namely Kelvin-Helmholtz instability and MHD-instability, are investigated.

The Kelvin-Helmholtz instability is characterized by the critical mean flow velocity  $M_c$ , given by Eq. (2.47), at which the transition to an unstable state occurs. At  $M = M_c$  the one-dimensional mode with transverse wavenumber  $n = 0$  (depending only on  $x$ ) becomes unstable, while the modes with  $n > 0$  are destabilized at higher  $M$ . For the one dimensional mode, the instability sets in for all  $k$  at the same value of  $M$ , whereas, for the two-dimensional modes the stability threshold depends on  $k$ . The long waves are more stable in comparison with to the short ones. The critical mean flow velocity  $M_c$  depends only on the densities of the fluids and thicknesses of the layers. If the densities of the two fluids, here aluminium and cryolite, are close to one another (as is the case in aluminum reduction cells), the waves are more stable in the channel with deep aluminum in comparison to the channels where this layer is shallow.

The parameter  $N$  is the criterion for the onset of the MHD-instability. For small values of  $N$  the waves are stable and become unstable as soon as  $N$  exceeds the critical value that depends on  $k$ . Contrary to the Kelvin-Helmholtz instability, the short waves are more stable in comparison with the long waves. The aspect ratio  $A$  influences the stability. Waves in the wide channel are more unstable in comparison to the narrow channel.

It was not observed any cross-interference between the mechanisms of MHD and Kelvin-Helmholtz instability as far as the threshold of instability is concerned. Both effects occur independently one from another. However, the direction of propagation of interfacial waves is influenced by the mean flow. For  $M = 0$  there exist two symmetrical waves moving in opposite directions. At  $M > 0$ , one of the waves slows down and finally changes its travelling direction so that, for large values of  $M$ , both waves move in the direction of the mean flow.

# Chapter 3

## Reconstruction of interfaces in aluminium reduction cells using electric potential measurements: forward and inverse problem<sup>†</sup>

### 3.1 Statement of the problem

The statement of the considered problem is schematically shown in Fig. 3.1a). Two fluids with different electrical conductivities  $\sigma_1$  (upper) and  $\sigma_2$  (lower) are situated in an infinite cylinder with the radius  $R$ . The cylinder walls are non-conducting. Along the axis of the cylinder a homogeneous electrical current with density  $j_0$  is applied.

If the interface between the fluids is flat, the electrical current  $\mathbf{J}$  is homogeneous everywhere (Fig. 3.1b)). In this case the total electrical potential  $\Phi$  is equal to the electrical potential  $\Phi_0 = -j_0 z / \sigma$ , induced by the applied electrical current  $j_0$ . As soon as the interface deviates from its flat shape due to interfacial waves or an external forcing, the electrical current density  $\mathbf{J}$  will become nonhomogeneous near the interface (Fig. 3.1c)). At  $z \rightarrow \pm\infty$  the mean current  $\mathbf{J}$  becomes asymptotically

---

<sup>†</sup>This chapter is based on the paper "Reconstruction of interfaces between electrically conducting fluids from electrical potential measurements". A.Kurenkov, H.Babowsky, and A.Thess. Submitted to *Inverse Problems*.

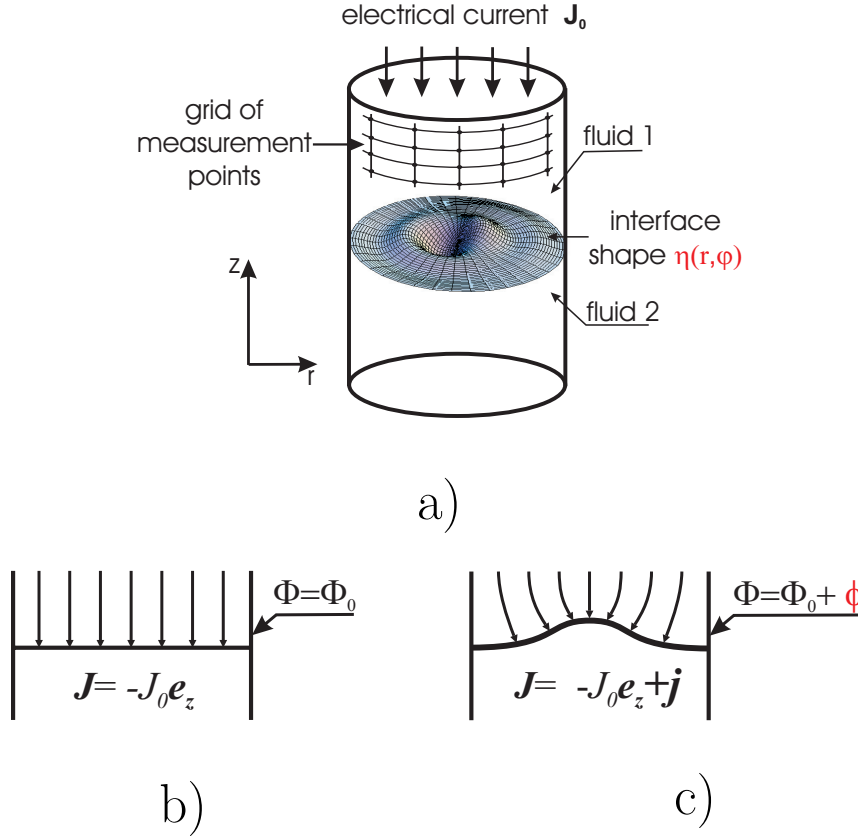


Figure 3.1: Definition of the problem. Figure a) shows the considered two fluid system with the interface and applied electrical current. In Figures b) and c) are shown the electrical current and electrical potential distribution for the unperturbed interface and for the perturbed interface respectively.

constant. The inhomogeneity of current  $\mathbf{J}$  can be represented by the perturbation of electrical current density  $\mathbf{j}$  (where  $\mathbf{J} = \mathbf{j}_0 + \mathbf{j}$ ). This induces a perturbation of the electrical potential  $\phi$  (where  $\Phi = \Phi_0 + \phi$ ). The question as to whether we can reconstruct the interface shape from measurements of  $\phi$  at the wall represents the central focus of our work.

The typical values of the interface displacement in the latter system are very small compared to the lateral extent of the system. Let us illustrate this by considering typical figures of a real aluminium reduction cell. Typically the cross-section of the aluminium reduction cell has a maximum length  $L = 10m$ . The interface displacement  $\eta$  is of the order of several centimetres. It is well known from industrial practice that already such small interface displacement can perturb significantly the operation of an aluminium reduction cell. As a result, our problem is characterised



by a very small ratio  $\epsilon = \eta/L$  between the interface displacement and the lateral size of the system. Therefore we have decided to restrict the present analysis to  $\epsilon \ll 1$ .

In our further discussion two tasks will be distinguished. The first task, the forward problem, concerns the calculation of the electrical potential in the fluids from the interface perturbation. The second task, the inverse problem, is devoted to the reconstruction of the interface shape from the electrical potential at the fluid-cylinder boundary.

The structure of this chapter is organised as follows. In the next section the solution of the forward problem is described. The dependence of the electrical potential in the fluids on the interface perturbation is studied in detail. The algorithm for the reconstruction is presented in section 3.3. Examples of a complete interface shape reconstruction are demonstrated in section 3.4. In section 3.5 the conclusion is summarised and some topics that would be useful to investigate in future are discussed.

## 3.2 Forward problem

### 3.2.1 The interface perturbation

We consider small deviations of the interface position  $z = \eta(r, \varphi, t)$  from its unperturbed location in the plane at  $z = 0$ . More precisely, we shall assume that  $\eta \ll R$ . We will restrict our attention to a cylindrical geometry. However, the present analysis can be extended to infinite rods with arbitrary cross sections.

The interface displacement can be represented in the form [45]

$$\eta(r, \varphi, t) = \sum_{i=1}^{\infty} \xi_i(t) \psi_i(r, \varphi) \quad (3.1)$$

where  $\psi_i(r, \varphi)$  is a complete set of orthonormal functions satisfying Neumann boundary conditions  $\partial\psi_i/\partial r$  at  $r = R$ . Using Bessel functions as a basis we can write any interface displacement in the form

$$\eta(r, \varphi, t) = \sum_{m=-M}^M \sum_{n=1}^N c_{mn}(t) J_m(k_{mn}r) e^{im\varphi}, \quad (3.2)$$

where  $c_{mn}$  is the complex amplitude of the interface modes,  $J_m$  is the Bessel function of the first kind,  $k_{mn} = y_{mn}/R$  and  $y_{mn}$  is the  $n$ -th solution of the equation  $J'_m(r) = 0$ . In the case  $m = 0$  we omit the solution  $y_{00} = 0$  because this solution corresponds to the flat surface  $\eta(t) = \text{const}$ . Here a limited number of modes  $M$  and  $N$  is used. It can be shown [26], that the amplitudes of higher modes decline as  $\langle |\eta_k|^2 \rangle \sim k^{-7/2}$ . Hence higher modes may be neglected.

Equation (3.2) describes the general case of a non-axisymmetric interface. For the axisymmetric case ( $m = 0$ ) this equation simplifies to

$$\eta(r, t) = \sum_{n=1}^N c_n(t) J_0(k_n r). \quad (3.3)$$

If the interface undergoes free oscillations, the time-dependent coefficients in equations (3.2) and (3.3) have the form  $c_{mn} e^{i\omega t}$ . The oscillation frequency  $\omega$  can be obtained from linear stability analysis. It should however be noted that we do not consider the dynamical origin of the time-dependent amplitudes  $c_{mn}(t)$  since the subsequent theory depends only on their instantaneous values.

### 3.2.2 Electrical potentials in the fluids

The interface perturbation  $\eta$  leads to an inhomogeneous distribution of the total electrical current density  $\mathbf{J}$  in the fluids. This inhomogeneous current density can be written as

$$\mathbf{J} = -j_0 \mathbf{e}_z + \mathbf{j} \quad (3.4)$$

where  $j_0$  is the density of the mean electrical current and  $\mathbf{j}$  the perturbation of the current density. The present analysis is valid for both direct current and low-frequency alternating electrical current where the skin effect can be neglected. The maximal allowable frequency of the electrical current can be estimated by  $\delta \ll R$ , where  $\delta$  is the skin depth. In our case this leads to the requirement that the frequency  $f$  of the alternating current is limited as

$$f \ll \frac{1}{2\pi\mu_0\sigma R^2}$$

where  $\sigma$  is the electrical conductivity of the fluid with the higher conductivity. The total electrical potential in the fluid is then

$$\Phi = \Phi_0 + \phi, \quad (3.5)$$

where  $\phi$  is the perturbation of the electrical potential which is induced by the perturbation of the current density  $\mathbf{j}$ . The perturbations of the electrical current  $\mathbf{j}$  and the electrical potential  $\phi$  are caused by the interface perturbation  $\eta(r, \varphi)$ . If the interface  $\eta(r, \varphi)$  is flat, then  $\mathbf{j} = 0$  and  $\phi = 0$ .  $\Phi_0$  is induced by the homogeneous electrical current density  $j_0$ . The solution for  $\Phi_0$ , called the basic solution, follows from Ohms law with boundary condition  $\Phi_0 = 0$  at  $z = 0$ :

$$\Phi_0 = \frac{j_0 z}{\sigma} \quad (3.6)$$

Perturbation of electrical potential  $\phi$  satisfies

$$\Delta\phi_1 = \Delta\phi_2 = 0 \quad (3.7)$$

together with the system of the four boundary conditions

$$\frac{\partial\phi}{\partial r} = 0, \quad \text{at } r = R, \quad (3.8)$$

$$\phi_1 = \phi_2 = 0, \quad \text{at } z = \pm\infty, \quad (3.9)$$

$$\phi_1 - \phi_2 = j_0\eta \left[ \frac{1}{\sigma_2} - \frac{1}{\sigma_1} \right], \quad \text{at } z = 0, \quad (3.10)$$

$$\sigma_1 \frac{\partial\phi_1}{\partial z} = \sigma_2 \frac{\partial\phi_2}{\partial z}, \quad \text{at } z = 0. \quad (3.11)$$

The first condition (3.8) expresses the fact of a non-conductivity of the cylinder walls and the second condition (3.9) expresses the vanishing electrical potential perturbation at  $z = \pm\infty$ . The last two conditions (3.10)-(3.11) follow from the continuity of the tangential component of the electrical field and the normal component of the electrical current density at the interface. The exact conditions are  $\mathbf{J}_1 \cdot \mathbf{n} = \mathbf{J}_2 \cdot \mathbf{n}$  and  $\Phi_1 = \Phi_2$  along the interface  $z = \eta(r, \varphi)$ . These two conditions were linearised around  $z = 0$  in order to solve the problem analytically. This method which is

based on the assumption of a small interface perturbation is commonly used for the analysis of aluminium reduction cells (see e.g. Davidson[17]).

The harmonic function which satisfies all four boundary conditions is determined from the ansatz [17]

$$\phi_i(r, \varphi, z) = \frac{j_0 \eta(r, \varphi)}{\sigma_i} f_i(z), \quad (3.12)$$

where  $\sigma_i$ ,  $i = 1, 2$  is the conductivity of the corresponding fluid. Subscript 1 denotes the first one and subscript 2 the second one respectively.  $f_i(z)$  are some functions to be determined,  $j_0$  is the density of the mean electrical current and  $\eta(r, \varphi) = c_{mn} J_m(k_{mn} r) e^{im\varphi}$  is the interface. This expression is valid for both fluids. Condition (3.8) is automatically satisfied because the first derivative of  $\eta(r, \varphi)$  vanishes at  $r = R$ . Substituting expression (3.12) into equation (3.7) and using condition (3.9), we obtain  $f_1(z) = b_1 \cdot \exp(-k_{mn} z)$  and  $f_2(z) = b_2 \cdot \exp(k_{mn} z)$ . We find the constants  $b_1$  and  $b_2$  from the boundary conditions (3.10)-(3.11) as  $b_1 = -b_2 = (\sigma_1 - \sigma_2)/(\sigma_1 + \sigma_2)$ . The electrical potential perturbation in the fluid is the superposition of the elementary potential perturbations caused by each single mode of the interface perturbation. The total potential perturbation in both fluids satisfy

$$\phi_i(r, \varphi, z) = \text{sign}[z] \frac{j_0}{\sigma_i} \frac{\sigma_1 - \sigma_2}{\sigma_1 + \sigma_2} \sum_{m=-M}^M \sum_{n=1}^N c_{mn} J_m(k_{mn} r) e^{im\varphi - k_{mn}|z|}. \quad (3.13)$$

For the axisymmetric interface case ( $m = 0$ ) this expression simplifies to

$$\phi_i(r, z) = \text{sign}[z] \frac{j_0}{\sigma_i} \frac{\sigma_1 - \sigma_2}{\sigma_1 + \sigma_2} \sum_{n=1}^N c_n J_0(k_n r) e^{-k_n |z|} \quad (3.14)$$

The perturbations of the electrical potential  $\phi$  in the fluid at the cylinder boundary caused by a single mode of the interface perturbation  $\eta(r, \varphi)$  are presented in Fig. 3.2b) for the axisymmetric case and Fig. 3.2d) for the non-axisymmetric case. The perturbations appear in both fluids, but they are higher in the poorly conducting fluid.

For large interface displacements the boundary conditions at the interface  $z = \eta$

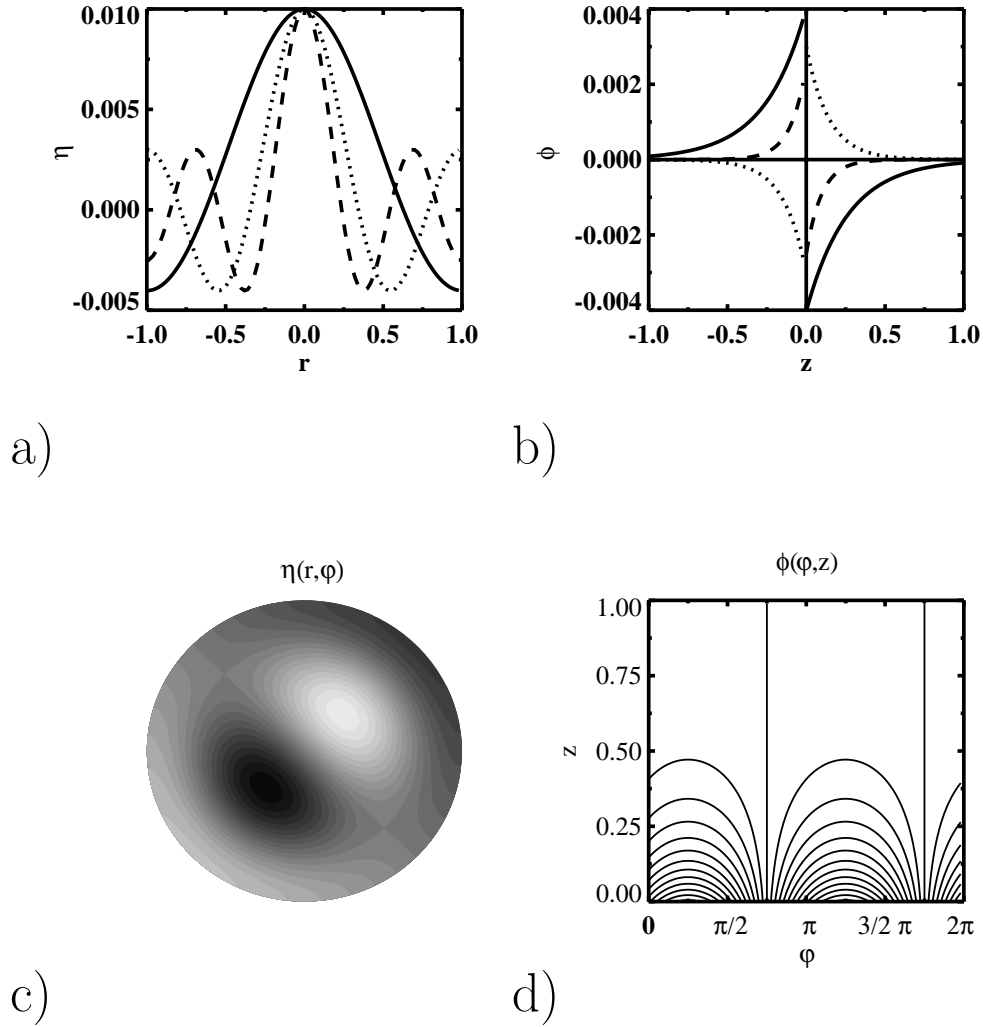


Figure 3.2: Interface perturbations and corresponding potential perturbations: in Figure a) the axisymmetric interface for the first, second and third radial modes (the modes (0,1), (0,2), (0,3)) is shown. Figure b) presents the dependence of the potential perturbation  $\phi$  on  $z$  in the fluid at the cylinder boundary, where  $\phi$  is caused by a single mode of the axisymmetric interface perturbation  $\eta(r)$ . The full line represents the potential perturbation which is obtained for the first radial mode of interface perturbation, the dotted line for the second radial mode, the dashed line for the third radial mode. In Figure c) the non-axisymmetric interface [the mode (1,2)] is shown and in Figure d) the caused by its the potential perturbation at the fluid boundary is presented.

can not be linearised anymore and the forward problem would have to be solved numerically. However, such fully numerical solution does not provide a clear understanding of the dependence of the electrical potential perturbation  $\phi$  on the interface

displacement  $\eta$ . In contrast, the analytical solution gives a comparatively simple expression which makes a qualitative analysis of the last dependence  $\phi$  on  $\eta$  possible. Therefore in the following parts of this chapter only the analytical solution of the forward problem will be used.

### 3.2.3 Non-dimensional equations

We define the dimensionless variables  $r^*, z^*, \eta^*, \phi^*$  by  $z^* = z/R$ ,  $r^* = r/R$ ,  $\eta^* = \eta/R$ ,  $\phi_i^* = \phi_i \sigma_i / j_0 R$ . In the dimensionless equations the expression  $k_{mn}r$  will be transformed to  $y_{mn}r^*$ . The dimensionless equation for the electrical potential in the non-axisymmetric case is thus modified to

$$\phi_i(r, \varphi, z) = \text{sign}[z] \sum_{m=-M}^M \sum_{n=1}^N c_{mn} J_m(y_{mn}r) e^{im\varphi - y_{mn}|z|} \quad (3.15)$$

and in the axisymmetric case it reduces to

$$\phi_i(r, z) = \text{sign}[z] \sum_{n=1}^N c_n J_0(y_n r) e^{-y_n |z|}. \quad (3.16)$$

In the remaining part of paper we will use only non-dimensional variables.

Evaluating equations (3.15) and (3.16) at the cylinder wall  $r = 1$  we finally arrive at the equations providing the link between the surface deflection (described by the expansion coefficients  $c_{mn}$  or  $c_n$ ) and the potential distribution at the walls. These equations form the mathematical basis of our work. The rest of the paper is devoted to the treatment of the inverse problem  $\phi(\varphi, z) \rightarrow c_{mn}$  or  $\phi(z) \rightarrow c_n$ .

It must be remarked, that for the reconstruction of the interface it is sufficient to have the data set of the electrical potentials at the fluid boundary in one of the fluids only. Therefore we consider only one fluid further in this paper. The  $\text{sign}[z]$  will be taken positive in the equations describing the dependence of the electrical potential perturbation on the interface perturbation. It is also assumed, that the basic interface is known. The possibilities for determining the basic interface location will be given in subsection 3.3.1.

## 3.3 Inverse problem

### 3.3.1 Basic location of the interface

For the subsequent interface reconstruction we need to know the position of the basic flat interface. For an experiment or application a cylinder of large but finite height  $H$  could be used, in which the mean electrical current  $\mathbf{J}$  could be applied between electrodes. Therefore in this subsection we consider the determination of the basic location for a finite cylinder.

If the interface is non-disturbed, the basic interface location can be easily determined from the measurement of the mean electrical current density  $j_0$  and from the voltage  $U$  between two electrodes. The conductivities  $\sigma_1$  and  $\sigma_2$  of the two fluids and the height of the cylinder  $H$  are also known. To find the interface position, we need to evaluate the expression for the mean electrical current. The last could be computed from the Ohms law as

$$j_0 = U \frac{\sigma_1 \sigma_2}{\sigma_2 h_1 + \sigma_1 h_2} \quad (3.17)$$

where  $h_1$  is the distance between the interface and the lower electrode,  $h_2$  between the interface and the upper electrode. Substituting  $h_1 = H - h_2$  in the last equation, we obtain

$$h_2 = \frac{U}{j_0} \frac{\sigma_1 \sigma_2}{\sigma_1 - \sigma_2} - \frac{\sigma_2}{\sigma_1 - \sigma_2} H. \quad (3.18)$$

In the practical application of the aluminium reduction cells the current density and the voltage between electrodes are measured automatically, so that the location of basic interface presents no difficulty.

If the interface undergoes small oscillations, the electrical voltage  $U$  becomes also oscillating near the value, which corresponds to the case without oscillations. Normally it is tried to hold the mean electrical current  $j_0$  in the aluminium reduction cells at a constant value. Therefore it is also possible to determine the basic location for the moving interface by the above described method. In this case the averaged voltage  $\langle U \rangle$  will be used instead of constant value  $U$  in eq. (3.18).

### 3.3.2 Reconstruction of axisymmetric interface

The interface perturbation is mapped into the electrical potential in the fluid at the cylinder boundary as follows

$$\phi_k = \sum_{n=1}^N c_n J_0(y_n) e^{-y_n z_k}. \quad (3.19)$$

Here  $c_n$  is the amplitude of  $n$ -th radial mode of the interface perturbation,  $\phi_k$  is the value of the electrical potential in the fluid at the cylinder wall at the  $k$ -th measurement point, and  $z_k$  is the  $z$ -coordinate of the  $k$ -th measurement point with  $1 \leq k \leq K$ .  $K$  is the total number of measurement points in vertical direction. The last expression can be transformed into the matrix equation

$$\phi_k = \sum_{n=1}^N A_{kn} c_n, \quad (3.20)$$

where the linear operator  $A_{kn} = J_0(y_n) e^{-y_n z_k}$  is also called the system matrix. A direct inversion of  $A$  leading to  $\eta = \phi \cdot A^{-1}$  is not in general possible for two reasons. First, the number of measurement points is usually higher than the number of modes to be reconstructed ( $K > N$ ). In this case we would have more equations than variables. Second, the system matrix is in general ill-conditioned and the inversion of the operator  $A$  becomes unstable. In this case the reconstruction error is so intense that the solution cannot be discerned from noise. We solve the presented inverse problem of the interface reconstruction in the least-square sense, i.e. we find the solution vector  $\boldsymbol{\eta}$  which minimises the deviation  $\| A\boldsymbol{\eta} - \boldsymbol{\phi} \|$ . A well-known technique for the solution of the linear least-squares problem is the singular value decomposition (SVD) method [52]. Using SVD the system matrix  $A$  can be written as

$$A = U \cdot \text{diag}[w] \cdot V^T, \quad (3.21)$$

where  $U$  is a  $N \times K$  column-orthogonal matrix,  $w$  is a  $K \times K$  diagonal matrix with positive elements on its diagonal only,  $V$  is a  $N \times N$  square orthogonal matrix. The matrices  $U$  and  $V$  satisfy  $U^T \cdot U = V^T \cdot V = I$ , where  $I$  is the unitary matrix. Then



the inverse operator  $A^{-1}$  can be represented in the form

$$A^{-1} = V \cdot \text{diag}[w^{-1}] \cdot U^T. \quad (3.22)$$

Based on this, we obtain the solution of the reconstruction problem as

$$\boldsymbol{\eta} = V \cdot \text{diag}[w^{-1}] \cdot (U^T \cdot \boldsymbol{\phi}) \quad (3.23)$$

The condition number of the system matrix  $A$  is defined in the common case as  $C = \|A\| \cdot \|A^{-1}\|$ , where  $\|\cdot\|$  is any valid matrix norm. If the Euclidean matrix norm is used then this is the ratio of the largest element of the matrix  $w$  to the smallest element of  $w$  [57]. The condition number is basically a measure of stability or sensitivity of a matrix (or the linear system it represents) to numerical operations. Matrices with condition numbers near 1 are said to be well-conditioned. If condition matrix is much greater as 1, they are ill-conditioned. One may not be able to trust the results of computations on an ill-conditioned matrix.

Applying to the problem at the hand, the reconstructed interface at a high condition number contains a higher reconstruction error. For the present reconstruction problem it is typical that the condition number of the system matrix increases with the growth of  $N$  (see Figure 3.3). Thus, the more radial modes we wish to reconstruct, the higher the reconstruction error will be.

At this point it is important to comment on the choice of the number of modes to be reconstructed (number  $N$  in eq. (3.19)). Fig. 3.4 demonstrates that the reconstruction error can significantly depend on the choice of  $N$ , whose incorrect choice leads to non-satisfactory reconstruction results. The reconstruction error is defined as the ratio of the norm of two functions [8]. The numerator of the following equation is the norm of the difference between the reconstructed and the exact interface functions, the denominator is the norm of the exact interface function.

$$\delta = \sqrt{\frac{\int_0^{2\pi} \int_0^1 [\eta(r, \varphi) - \eta_{ex}(r, \varphi)]^2 r dr d\varphi}{\int_0^{2\pi} \int_0^1 \eta_{ex}^2(r, \varphi) r dr d\varphi}} \quad (3.24)$$

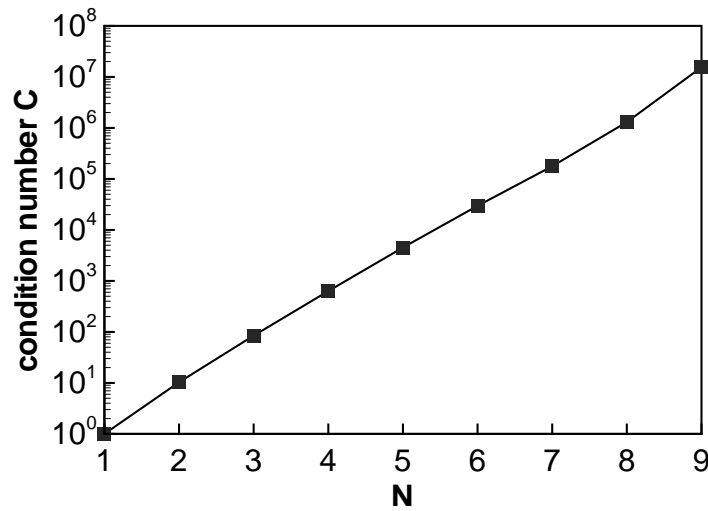


Figure 3.3: Dependence of the condition number of the system matrix on the number of the reconstructed radial modes  $N$ . The computation is performed for an axisymmetric interface and non-equidistant location of the measurement points.

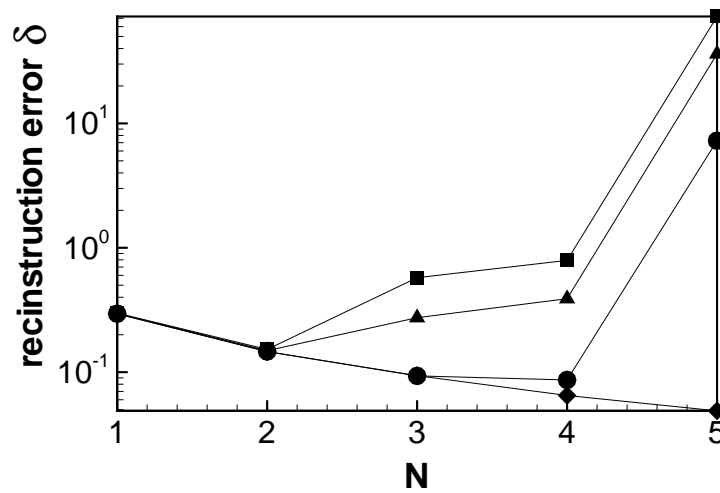


Figure 3.4: Dependence of the reconstruction error on the number of radial modes  $N$  which is used for the reconstruction of the axisymmetric interface. ◆ denote the reconstruction without data error, ● denotes the 1% data error, ▲ - 5% data error, ■ - 10% data error.

To find the optimal number of modes  $N$ , which are used for the reconstruction, the L-curve criterion [33] is used. We solve the forward problem for different numbers

$N$  and compute for any  $N$  the integral squared norm of the solution  $\|\eta(r)\|$  (called solution norm below) and the squared Euclidean norm  $\|A\boldsymbol{\eta} - \boldsymbol{\phi}\|$  (called residual norm):

$$\|\eta(r)\| = \int_0^{2\pi} \int_0^1 \eta^2(r) r dr d\varphi \quad (3.25)$$

$$\|A\boldsymbol{\eta} - \boldsymbol{\phi}\| = \sum_{k=1}^K \left[ \left( \sum_{n=1}^N A_{kn} \cdot c_n \right) - \phi_k \right]^2 \quad (3.26)$$

Afterwards we plot  $\log \|\eta(r)\|$  as a function of  $\|A\boldsymbol{\eta} - \boldsymbol{\phi}\|$ . The resulting plot is typically L-shaped (see Fig. 3.5) with the largest curvature at the optimal number of modes ( $N = 2$  in most of the cases) used for reconstruction. In order to achieve a good reconstruction quality  $N$  should to be equal to the number of active modes in the system, i.e. the modes with significant large amplitudes. The corner of the presented L-curve shows the compromise between data error and reconstruction error. For small  $N$  the reconstructed interface is too smooth. For large  $N$  the data error decreases but the reconstructed interface has too large deviations, it becomes too wavy and the results of the reconstruction are useless (see Fig. 3.6).

The bend of the plotted L-curve can be computed applying a method described by Kaufmann and Neumaier [38]. This method works as follows. Describe the vertices of the L-curve as  $(w_1, q_1), (w_2, q_2), \dots, (w_L, q_L)$ , where  $w_1 > w_2 > \dots > w_L$ ,  $q_1 < q_2 < \dots < q_L$ , where  $w_l$  and  $q_l$  are the  $l$ -th values of the residual norm and the solution norm respectively. The regularisation parameter  $N$  is set for any step to  $l = 1, \dots, L$ . Then in the first step we compute the slopes

$$s_k = (w_{k-1} - w_k) / (q_k - q_{k-1}) \quad k = 2, \dots, L \quad (3.27)$$

and in the second step the quotient of two consecutive slopes

$$d_k = s_k / s_{k-1}. \quad (3.28)$$

The largest quotient  $c_k$  indicates a bend of the L-curve, which is in our case the optimal number of modes to be reconstructed.

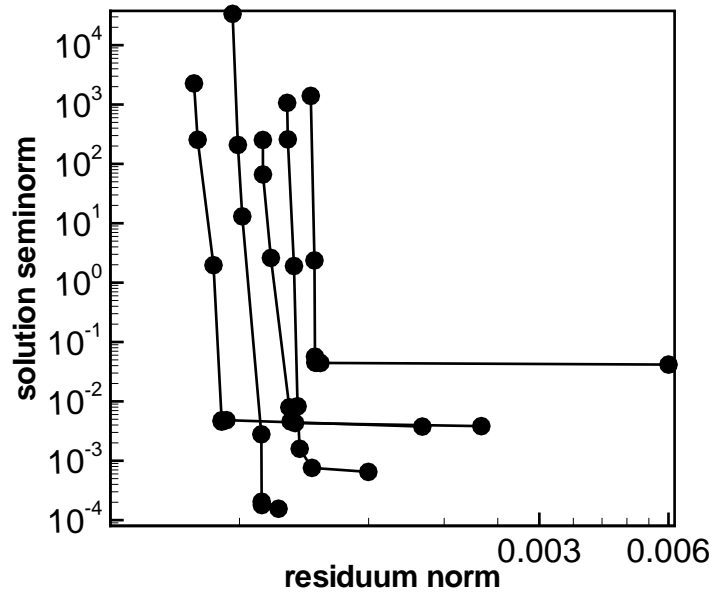


Figure 3.5: Dependence of the solution norm on the residuum norm (L-Curve) at 1% data error. The azimuthal modes with  $m = 0.5$  are plotted. The optimal number of reconstructed modes is  $N = 2$ .

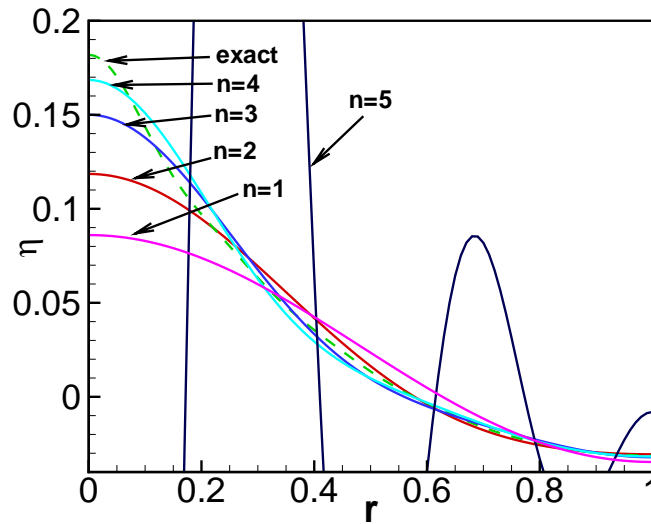


Figure 3.6: Reconstruction of axisymmetric interface with a different number of radial modes at 1% data error.

### 3.3.3 Reconstruction of the non-axisymmetric interface

The mapping of the interface perturbation into the electrical potential at the fluid boundary ( $r = 1$ ) can be described for the non-axisymmetric case as follows:

$$\phi_{kp} = \sum_{m=-M}^M e^{im\varphi_p} \sum_{n=1}^N c_{mn} J_m(y_{mn}) e^{-y_{mn}z_k}. \quad (3.29)$$

Here  $k$  is the vertical running index of the measurement points and  $p$  is the azimuthal running index. These numbers define the measurement point locations  $(z_k, \varphi_p)$  respectively (see Figure 3.1a), and  $\varphi_p = 2\pi \frac{p}{P}$ , where  $P$  is the number of measurement points in azimuthal direction. Eq.(3.29) shows, that the reconstruction problem for the non-axisymmetric case decouples into  $M$  inverse problems for the individual Fourier-modes whose mathematical structure is identical to that of the axisymmetric problem. In general, the reconstruction algorithm for the non-axisymmetric interface can be divided in two operations: 1) discrete Fourier transformation 2) solution of the inverse problem for every  $m = 0, \dots, M$  with the method described in section 3.3.2. Here  $M$  is the number of azimuthal modes to be reconstructed. The discrete Fourier transformation filters from the common data set the electrical potential which is caused by all of radial modes  $n = 1, \dots, \infty$  of fixed azimuthal wave number  $m$ . After this we can apply the algorithm of reconstruction described above in section 3.3.2.

The number of azimuthal modes from which we can reconstruct  $M$  is limited by the number of measurement point in azimuthal direction as  $M < P/2$  according to the sampling theorem. In practice good results can be achieved with a small number of  $M = 1, \dots, 6$ . This will be discussed later in the next subsection.

Equation (3.29) can be transformed to

$$\phi_{kp} = \sum_{m=-M}^M F_{km} e^{im\varphi_p} = \sum_{m=-M}^M F_{km} e^{2\pi i m \frac{p}{P}} \quad (3.30)$$

where

$$F_{km} = \sum_{n=1}^N c_{mn} J_m(y_{mn}) e^{-y_{mn}z_k}.$$

Expression (3.30) represents the discretisation of a harmonic function. This function

is the dependence of the electrical potential perturbation on an azimuthal angle  $\phi(\varphi)$  at some fixed point on the cylinder boundary with  $r = 1$  and  $z = \text{const}$ .

In the first step of reconstruction a discrete Fourier transform is performed on each  $k$ -th row of the measurement data set  $\phi_{kp}$  with  $p = 0, \dots, P$ ,  $P = 2M$  and  $k = \text{const}$ . This operation let us filter the electrical potential perturbations caused by the different azimuthal modes. As result the coefficients matrix  $F$  is obtained as

$$F_{km} = \sum_{p=0}^{P-1} \phi_{kp} e^{-2\pi i \frac{p}{P} m}. \quad (3.31)$$

The  $m$ -th column  $\mathbf{f}$  of the coefficients matrix  $F$  satisfies for any  $m = 1, \dots, M$  the matrix equation

$$f_k = \sum_{n=1}^N A_{kn} \cdot c_n \quad (3.32)$$

where the linear operator

$$A_{kn} = J_m(y_{mn}) e^{-y_{mn} z_k} \quad (3.33)$$

is now the system matrix. The solution of such matrix equations using the singular value decomposition method has already been discussed in the subsection 3.3.2. The matrix  $A$  can be decomposed as (3.23) and the particular solution for non-axisymmetric case is

$$\mathbf{b} = V \cdot \mathbf{w}^{-1} \cdot U^T \cdot \mathbf{f} \quad (3.34)$$

Here the vector  $\mathbf{b}$  corresponds to the  $m$ -th row of the amplitudes matrix  $c_{mn}$ . We note, that the reconstruction problem is solved for each mode with  $m = 0, \dots, M$  completely independent from the other azimuthal modes.

### 3.3.4 Choice of optimal reconstruction parameters

In this subsection the choice of the number of azimuthal modes  $M$ , of the radial mode number  $N$ , and also the measurement points numbers  $p$  and  $k$ , are discussed. The general case of non-axisymmetrical interface is discussed here, because the axisymmetric interface is a partial case of the general problem.

In the presented reconstruction problem there exist two very important parameters, namely  $M$  and  $N$ , the number of modes which form the reconstructed

interface. In reality there exists an infinite number interfacial modes at the same time. As a matter of fact, we can not reconstruct all of these modes, but it is also not necessary. The gravitational wave number spectrum satisfies the power law [26]

$$\langle |\eta_k|^2 \rangle \sim k^{-7/2} = y^{-7/2}. \quad (3.35)$$

It means, that the higher modes have a very small amplitude and can be neglected without loss of important information about the interface shape to be recovered. This information can be used for the a-priori estimation of number  $M$ . The electrical potential perturbation  $\phi$  which is produced by an azimuthal mode declines very fast with growing  $m$  and  $n$ . If we consider some point on the cylinder boundary with coordinates  $(1, \varphi, z)$ , it satisfies

$$\phi_m = \text{sgn}[z] \sum_{n=1}^{\infty} \eta(1, \varphi) \exp(-y_{mn}z).$$

The amplitudes of interfacial waves decline as shown in Eq.(3.35), therefore we rewrite the last expression as

$$\phi_m = \text{sgn}[z] \sum_{n=1}^{\infty} y_{mn}^{-7/4} \exp(-y_{mn}z).$$

The conclusion is that for any fixed point on the cylinder wall the higher modes produce very small electrical potential. It is smaller in comparison to the measurement error from the measurement of the strongest mode. This mode which causes the largest electrical potential on every data point is the mode with  $m = 1, n = 1$ . We have used this fact as criterion for filtering the data after the Fourier decomposition procedure. In other words, the choice of  $M$ , the number of azimuthal modes which are to be reconstructed, depends on the measurement error. According to this, the following numbers of azimuthal modes  $M$  has been chosen in dependence on the measurement error: The optimal number of reconstructed modes  $N$  is found using the L-curve criterion, which was described above. This procedure is done for any azimuthal mode number  $m = 0 \dots M$ . We have chosen  $N = 2$  because the L-curves for the 6 first azimuthal modes with  $m = 0..5$  have a sharp bend in the majority of

Table 3.1: Dependence of  $M$  on the measurement error.

meas. error	1%	5%	10%
$M$	6	3	3

cases at  $N = 2$  (see Fig. 3.5).

After this procedure we have the numbers of modes to be reconstructed,  $M$  and  $N$ . Then we choose the number of measurement points in the vertical direction as  $k \geq N$  and in azimuthal direction as  $p \geq 2M$ . The first condition follows from the fact that the number of reconstructed modes must be smaller as the number of points in vertical direction  $k$ . The second one follows from the sampling theorem.

### 3.4 Examples of interface reconstruction

The simulation is performed in four steps as follows. First the amplitudes  $c_n$  for axisymmetric or  $c_{mn}$  for non-axisymmetric cases are prescribed which determine the interface shape. In the second step the electrical potentials  $\phi_k$  or  $(\phi_{kp}$  in the general case) at the cylinder boundary are computed using the analytical solution (3.19) or (3.23) for the forward problem. Then in the third step random white noise is added to the obtained electrical potential data set as  $\phi_{kp}(1 + \varepsilon\delta)$ , where  $-1 < \varepsilon < 1$  is a random number and  $\delta$  is the maximum amplitude of error. These operations simulate the noisy measurement of the electrical potentials. Different noise amplitudes represent different data errors. The fourth step is the reconstruction of the interfaces employing the algorithms described in section 3.3.

We perform our numerical experiments for two cases. Firstly, the axisymmetric interface is reconstructed and then the general case of a non-axisymmetric interface is investigated. We have tried to simulate the conditions similar to the physical experiment. Therefore the amplitudes of interfacial waves are computed as

$$\eta_{mn} = y_{mn}^{-1.75} \tag{3.36}$$

where  $y_{mn}$  is the dimensionless wavenumber for the  $n$ -th radial of the  $m$ -th azimuthal



mode.

Examples of the axisymmetric interface reconstruction are shown in Fig. 3.7. The exact interface shape consists of the first ten modes which amplitudes are com-

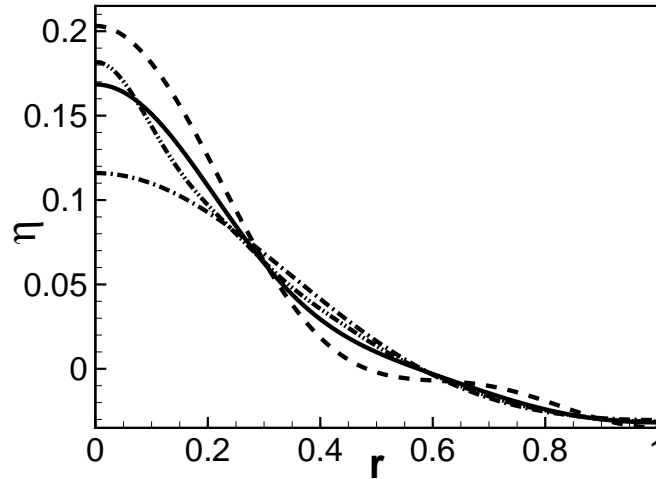


Figure 3.7: Reconstruction of the axisymmetric interface for different data errors. The exact interface is denoted with full line. The --- corresponds to 1% data error, the - - - to 5% data error, the . . . . 10% data error.

puted using Eq.(3.36). The number of modes  $N$  which are used for the reconstruction procedure, is obtained from the L-curve (see Fig. 3.5). It depends on the measurement error. For 1% data error in measurement set we have used four modes for reconstruction, for 5% - three modes and for 10% two modes only. The reconstructed curves are very similar to the exact interface. Some deviation in the centrum of the interface ( $r > 0$ ) results from the fact, that the true interface has more modes in comparison to the reconstructed. However, the form of the interface is well recovered. Even if the the measurement error is as high as 10%, the reconstructed interface looks similar to the exact one. It demonstrates that the presented reconstruction method is robust with respect to measurement noise.

Figure 3.8 presents examples of the non-axisymmetric interface reconstruction. The exact interface consists of the first ten radial modes for  $m = 0, \dots, 10$ , whose dimensionless amplitudes are computed with Eq. (3.36). Of course, the reconstructed interface is smooth in comparison to the true interface consisting of 100 interfacial modes because we reconstruct with a short number of interfacial modes. However,

the reconstructed interface is also very similar to the exact interface even for the highest measuring error.

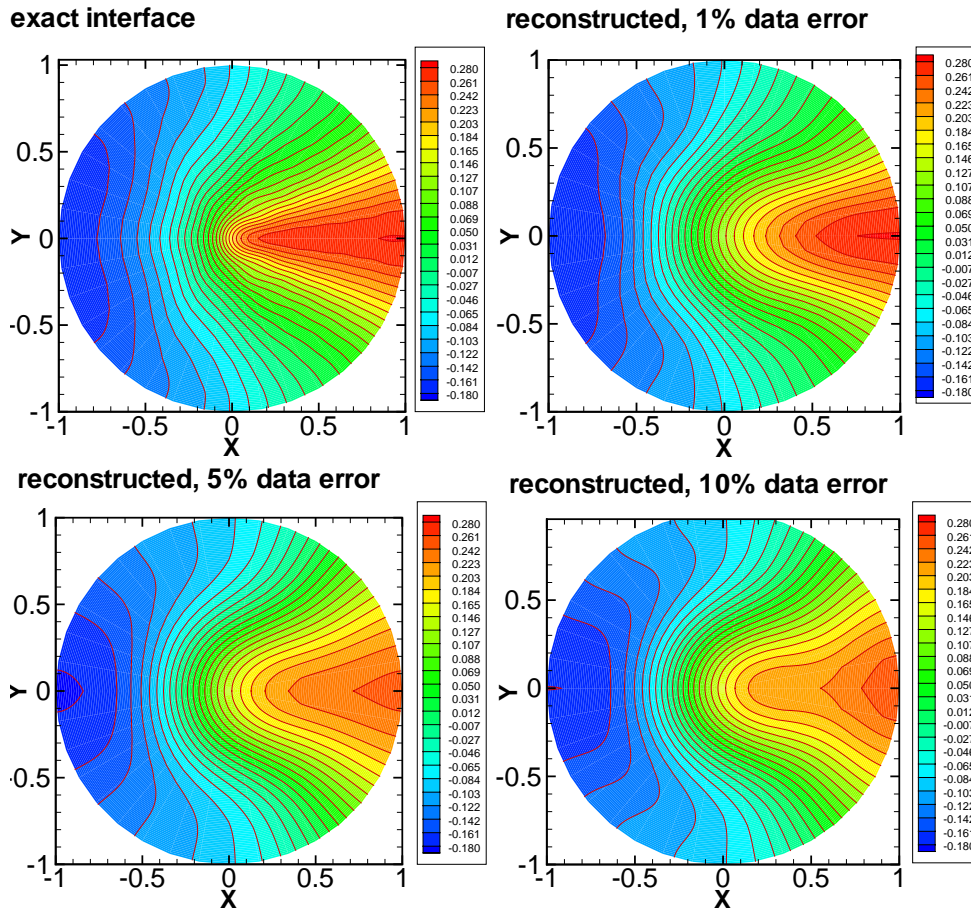


Figure 3.8: Reconstruction of the non-axisymmetric interface. View from above.

### 3.5 Conclusion

In the present work we have described an algorithm for the interface reconstruction from electrical potential measurements at the fluid boundary in a two-fluid system with cylindrical configurations. We have investigated axisymmetric and non-axisymmetric interfaces. In both cases the interface shape is determined with good accuracy. The method is robust to measurement errors and works even at noise levels as high as 10%.

Two important parameters are presented in this inverse problem. There are

the numbers of modes, which are used for reconstruction,  $M$  for azimuthal modes and  $N$  for radial. It is shown, that  $M$  can be estimated before the reconstruction. The incorrect choice of  $N$  has a strong influence on the reconstruction quality and it makes the reconstruction results unacceptable. An optimal  $N$  is found with the help of the dependence of the integral solution norm on the residual norm, which has the typical L-curve shape and its bend corresponds to the optimal number of modes to be reconstructed. It was found that the optimal number is  $N = 2$  for the most cases.

The presented reconstruction algorithm is based on the analytical solution of the forward problem. Therefore it is much faster in comparison to any another method which is based on the numerical solution. The numerical cost of reconstruction is extreme low. At the other side, the reconstruction results show good accuracy. The presented method can be used in an real-time fast interface detection system, whose application field can be the aluminium reduction cells, glass melting etc.



# Chapter 4

## Reconstruction of interfaces in aluminium reduction cells using magnetic field measurements: solution of the forward problem<sup>‡</sup>

### 4.1 Introduction

Fig. 4.1 shows the statement of the problem. Two fluids with different electrical conductivities are superimposed in an infinitely long rod. The form of the cross-section is arbitrary complex and it is constant throughout the rod. Walls of the rod are non-conducting. A homogeneous electrical current with current density  $\mathbf{J}_0 = -J_0 \mathbf{e}_z$  is applied which flows through the interface between the fluids. The basic state is the flat interface ( $\eta(x, y) = 0$ ) and the homogeneous electrical current  $\mathbf{J}_0$ . The current  $\mathbf{J}_0$  produces the main magnetic field  $\mathbf{B}_0$ . If the interface is perturbed ( $\eta(x, y) \neq 0$ ), the magnetic field perturbation  $\mathbf{b}$  appears in addition to the main magnetic field  $\mathbf{B}_0$ . The reason of this is that the electrical current distribution is changed as the result of the redistribution of electrical conducting mediums in the rod. For the disturbed interface it appears the perturbation of electrical current  $\mathbf{j}$ .

---

<sup>‡</sup>This chapter is based on the paper "Computation of the magnetic field in two fluid systems with electrical current through the interface". A.Kurenkov and A.Thess. Submitted to *Magnetohydrodynamics*.

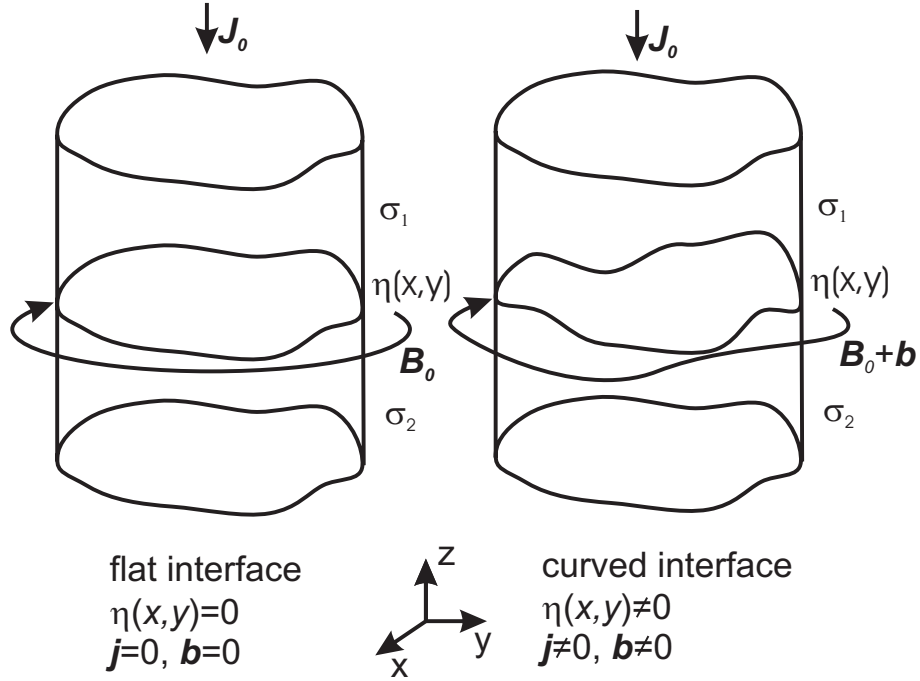


Figure 4.1: Sketch of the problem. The left picture shows the flat interface. The form of cross-section is arbitrary. Neither the electrical current perturbation nor magnetic field perturbation are presented. The right picture shows the case of disturbed interface. The magnetic field perturbation and current perturbation appears.

In the next sections a semi-analytical method will be described for computing the electrical current perturbation  $\mathbf{j}$  and the magnetic field perturbation  $\mathbf{b}$ .

## 4.2 Governing equations

### 4.2.1 Interface displacement

We consider small deviations of the interface position  $z = \eta(x, y, t)$  from its unperturbed location in the plane at  $z = 0$ . Then the interface displacement can be represented in the form [45]

$$\eta(x, y, t) = \sum_{n=1}^{\infty} \eta_n(t) \psi_n(x, y) \quad (4.1)$$

where  $\eta_n(t)$  time-dependent amplitudes of interfacial modes,  $\psi_n(x, y)$  is the complete set of orthonormal functions determined by

$$(\nabla_H^2 + k_n^2) = 0 \quad \text{in } D$$

$$\mathbf{n} \nabla \psi = 0 \quad \text{in } L$$

$$\langle \psi_m \psi_n \rangle = \delta_{mn}$$

$\langle \rangle$  means the averaging over the cross-section  $D$ ,  $k_n$  are the eigenvalues,  $\delta_{mn}$  is the Kroneker delta and  $L$  is the intersection line of interface boundary with the rod walls. We do not consider in this thesis the dynamical behavior of the interfacial waves and therefore we omit in the follows part the time-dependence in the amplitudes of the waves  $\eta_{mn}$ . Such quasistatistical approach simplifies the treatment of the electrodynamical problem. However, slow oscillations of the interface can be taken into account by replacing  $\eta_n$  with  $\eta_n \cos(\omega t)$ .

### 4.2.2 Computation of perturbed electrical current

We start with the computing of the current density distribution in the rod. We assume, that the temporal variation of the electrical current  $\mathbf{J}_0$  and interface  $\eta(x, y)$  does not affect the magnetic field distribution. Then the magnetic field perturbation and the electrical current perturbation can be computed quasistatically under the assumption

$$\nabla \times \mathbf{E} = -\frac{\partial \mathbf{B}}{\partial t} \approx 0.$$

We decompose the total electrical current as

$$\mathbf{J} = \mathbf{J}_0 + \mathbf{j}, \tag{4.2}$$

where  $\mathbf{J}_0$  is the mean electrical current (the electrical current which is applied to the rod if the interface is flat,  $\eta(x, y) = 0$ ).  $\mathbf{j}$  is the current perturbation which corresponds to the interface displacement ( $\eta(x, y) \neq 0$ ). Analogically the total

electrical potential in the fluids can be described as

$$\Phi = \Phi_0 + \phi \quad (4.3)$$

and the total magnetic field is

$$\mathbf{B} = \mathbf{B}_0 + \mathbf{b}, \quad (4.4)$$

where  $\phi$  is the perturbation of the electrical potential induced by the current density perturbation  $\mathbf{j}$ . The electrical potential perturbations satisfy the Laplace-equations

$$\Delta\phi_1 = \Delta\phi_2 = 0 \quad (4.5)$$

with the following boundary conditions

$$\frac{\partial\phi_1}{\partial n} = \frac{\partial\phi_2}{\partial n} = 0, \quad x, y \in L \quad (4.6)$$

$$\phi_1 = \phi_2 = 0, \quad z = \pm\infty \quad (4.7)$$

$$\phi_1 - \phi_2 = J_0\eta \left[ \frac{1}{\sigma_2} - \frac{1}{\sigma_1} \right], \quad z = 0 \quad (4.8)$$

$$\sigma_1 \frac{\partial\phi_1}{\partial z} = \sigma_2 \frac{\partial\phi_2}{\partial z}. \quad z = 0 \quad (4.9)$$

The first condition (4.6) expresses the non-conductivity of the cylinder walls and the second condition (4.7) shows the vanishing of the electrical potential perturbation for  $z = \pm\infty$ . The last two equations (4.8-4.9) follow from the continuity of the tangential component of the electrical field and the normal component of the electrical current density at the interface respectively. The exact conditions are  $\mathbf{J}_1 \cdot \mathbf{n} = \mathbf{J}_2 \cdot \mathbf{n}$  and  $\Phi_1 = \Phi_2$  along the interface  $z = \eta(r, \varphi)$ . They were linearized around  $z = 0$  in order to solve the problem analytically. This method which is based on the assumption of the small interface perturbation was used for the analysis of aluminium reduction cells (see e.g. Davidson [17], [41]).

The harmonic function which satisfies all four boundary conditions is determined from the ansatz [17]

$$\phi_i(x, y, z) = \frac{J_0\eta(x, y)}{\sigma_i} f_i(z) \quad (4.10)$$



where  $\sigma_i$ ,  $i = 1, 2$  is the conductivity in the corresponding fluid. Subscript 1 denotes the first one and subscript 2 the second one respectively.  $f_i(z)$  are the some functions which have to be determined. This expression is valid for both fluids. Substituting expression (4.10) into equation (4.5) and using condition (4.7) we obtain  $f_1(z) = b_1 \cdot \exp(-k_{mn}z)$  and  $f_2(z) = b_2 \cdot \exp(k_{mn}z)$ . We find the constants  $b_1$  and  $b_2$  from the boundary conditions (4.8)-(4.9) as  $b_1 = -b_2 = (\sigma_1 - \sigma_2)/(\sigma_1 + \sigma_2)$ . The electrical potential perturbation in the fluid is the superposition of the elementary potential perturbations caused by each mode of the interface perturbation. Then the potential perturbation in the fluid caused by a one single mode is

$$\phi_i(x, y, z) = \text{sign}(z) \frac{J_0 \sigma_1 - \sigma_2}{\sigma_i \sigma_1 + \sigma_2} \eta(x, y) e^{-k|z|}. \quad (4.11)$$

From this expression the electrical current density can be derived

$$\mathbf{j} = -\text{sign}(z) J_i \nabla [\eta(x, y) e^{-k|z|}], \quad (4.12)$$

where  $J_i = \frac{J_0 \sigma_1 - \sigma_2}{\sigma_i \sigma_1 + \sigma_2}$ .

### 4.2.3 Computation of the magnetic field perturbation

The total magnetic field is presented as the sum of the main component  $\mathbf{B}_0$  and magnetic field perturbation  $\mathbf{b}$ :

$$\mathbf{B} = \mathbf{B}_0 + \mathbf{b}. \quad (4.13)$$

In the following we derive the expressions for the magnetic field perturbation  $\mathbf{b}$ . The magnetostatic problem has to be solved

$$\mathbf{j} = \frac{1}{\mu_0} \nabla \times \mathbf{b} \quad (4.14)$$

$$\nabla \cdot \mathbf{b} = 0 \quad (4.15)$$

$$\mathbf{b} \rightarrow 0 \quad \text{for} \quad |\mathbf{r}| \rightarrow \infty \quad (4.16)$$

where  $\mathbf{r}$  is the position vector. We introduce the magnetic vector potential  $\mathbf{a}$  via

$$\mathbf{b} = \nabla \times \mathbf{a} \quad (4.17)$$

with the gauge

$$\nabla \cdot \mathbf{a} = 0. \quad (4.18)$$

Then the problem can be rewritten to

$$-\nabla^2 \mathbf{a} = \mu_0 \mathbf{j} \quad (4.19)$$

$$\mathbf{a} \rightarrow 0 \quad \text{for} \quad |\mathbf{r}| \rightarrow \infty \quad (4.20)$$

The solution of such a problem is well-known as Biot-Savart law:

$$\mathbf{a}(\mathbf{r}) = \frac{\mu_0}{4\pi} \iiint \frac{\mathbf{j}(\mathbf{r}')}{|\mathbf{r} - \mathbf{r}'|} dV' \quad (4.21)$$

where  $\mathbf{r}$  is the position vector,  $\mathbf{r}'$  is the running vector. Inserting the explicit expression (4.12) for the electrical potential perturbation  $\mathbf{j}$  into the last equation, we obtain

$$\mathbf{a}(\mathbf{r}) = -\frac{\mu_0 J_i}{4\pi} \iiint \text{sgn}(z') \frac{\nabla' [\eta(\mathbf{r}'_h) \exp(-k|z'|)]}{|\mathbf{r} - \mathbf{r}'|} dV'. \quad (4.22)$$

From the last expression it can be easily determined the expression for the magnetic field perturbation

$$\mathbf{b}(\mathbf{r}) = -\frac{\mu_0 J_i}{4\pi} \iiint \text{sgn}(z') \frac{\mathbf{r} - \mathbf{r}'}{|\mathbf{r} - \mathbf{r}'|^3} \times \nabla' (\eta(\mathbf{r}'_h) e^{-k|z'|}) dV'. \quad (4.23)$$

The magnetic field perturbation  $\mathbf{b}$  can be represented as a sum of the vertical and the horizontal components. Using the identity  $\nabla(\mathbf{u}\mathbf{v}) = \mathbf{v}\nabla\mathbf{u} + \mathbf{u}\nabla\mathbf{v}$ , we get:

$$\begin{aligned} \mathbf{b}(\mathbf{r}) = & -\frac{\mu_0 J_i}{4\pi} \iiint \text{sgn}(z') \left\{ \frac{(z - z') \mathbf{e}_z}{|\mathbf{r} - \mathbf{r}'|^3} \times \nabla' \eta(\mathbf{r}'_h) e^{-k|z'|} + \right. \\ & \frac{\mathbf{r} - \mathbf{r}'}{|\mathbf{r} - \mathbf{r}'|^3} \times \nabla' \eta(\mathbf{r}'_h) e^{-k|z'|} - \\ & \frac{\mathbf{r}_h - \mathbf{r}'_h}{|\mathbf{r} - \mathbf{r}'|^3} \times \eta(\mathbf{r}'_h) \text{sgn}(z') k e^{-k|z'|} \mathbf{e}_z - \\ & \left. \frac{(z - z') \mathbf{e}_z}{|\mathbf{r} - \mathbf{r}'|^3} \times \text{sgn}(z') k e^{-k|z'|} \mathbf{e}_z \right\} dV' \end{aligned} \quad (4.24)$$

where  $\mathbf{r}_h$  is the horizontal position vector,  $\mathbf{r}'_h$  is the running horizontal position vector. The last term in this expression is equal to zero ( $\mathbf{e}_z \times \mathbf{e}_z = 0$ ). The second term represents the vertical magnetic field and two other are the horizontal components of the magnetic field perturbation.

In order to make these expressions more compact we define the integral kernels:

$$K_1(\mathbf{r}, \mathbf{r}', k) = k \int_{-\infty}^{\infty} \frac{e^{-k|z'|}}{|\mathbf{r} - \mathbf{r}'|^3} dz' \quad (4.25)$$

$$K_2(\mathbf{r}, \mathbf{r}', k) = \int_{-\infty}^{\infty} \text{sgn}(z') \frac{e^{-k|z'|}(z - z')}{|\mathbf{r} - \mathbf{r}'|^3} dz' \quad (4.26)$$

$$K_3(\mathbf{r}, \mathbf{r}', k) = \int_{-\infty}^{\infty} \text{sgn}(z') \frac{e^{-k|z'|}}{|\mathbf{r} - \mathbf{r}'|^3} dz'. \quad (4.27)$$

Then the horizontal component of the magnetic field can be expressed as an integral over the surface deflection:

$$\mathbf{b}_h(\mathbf{r}) = \frac{\mu_0 J_i}{4\pi} \iint_D \{K_1 \cdot (\mathbf{r}_h - \mathbf{r}'_h) \eta(\mathbf{r}'_h) + K_2 \cdot \nabla' \eta(\mathbf{r}'_h)\} \times \mathbf{e}_z dx' dy'. \quad (4.28)$$

From the last expression the components  $\mathbf{b}_x$ ,  $\mathbf{b}_y$  can be obtained:

$$\mathbf{b}_x(\mathbf{r}) = \frac{\mu_0 J_i}{4\pi} \iint_D \left\{ K_1 \cdot (y - y') \eta(\mathbf{r}'_h) + K_2 \cdot \frac{\partial \eta(\mathbf{r}'_h)}{\partial y} \right\} dx' dy'. \quad (4.29)$$

$$\mathbf{b}_y(\mathbf{r}) = -\frac{\mu_0 J_i}{4\pi} \iint_D \left\{ K_1 \cdot (x - x') \eta(\mathbf{r}'_h) + K_2 \cdot \frac{\partial \eta(\mathbf{r}'_h)}{\partial x} \right\} dx' dy'. \quad (4.30)$$

The vertical component of magnetic field can be expressed as

$$\mathbf{b}_z(\mathbf{r}) = - \iint_D K_3 \cdot (\mathbf{r}_h - \mathbf{r}'_h) \times \nabla' \eta(\mathbf{r}'_h) dx' dy'. \quad (4.31)$$

The last integral can be simplified using the identity  $\nabla'_h \times \{K_3 \cdot (\mathbf{r}_h - \mathbf{r}'_h) \cdot \eta(\mathbf{r}'_h)\} =$

$-K_3(\mathbf{r}_h - \mathbf{r}'_h) \times \nabla'_h \eta(\mathbf{r}'_h)$  and the Stokes theorem:

$$\mathbf{b}_z(\mathbf{r}) = -\frac{\mu_0 J_i}{4\pi} \oint_L K_3 \cdot (\mathbf{r}_h - \mathbf{r}'_h) \eta(\mathbf{r}'_h) d\mathbf{r}'_h \quad (4.32)$$

where  $L$  is the intersection line of the interface boundary with the rod walls.

### 4.3 Results

The semi-analytical method represented above allows us to compute the magnetic field outside the vessel if the current density  $J_0$  and the interface displacement  $\eta(x, y)$  are known. Here two cases were investigated, the vessel with the cylindrical cross-section and with the rectangular cross-section. In case of a cylindrical cross-section the interface is assumed as

$$\eta(r, \varphi) = \sum_{m=0}^M \sum_{n=1}^N J_m(y_{mn}r) (\eta_{mn}^A \cos(m\varphi) + \eta_{mn}^B \sin(m\varphi))$$

where  $y_{mn}$  are the prime zeroes Bessel-function  $J_m$ . For the rectangular cross-section the interface is

$$\eta(x, y) = \sum_{m=0}^M \sum_{n=1}^N \eta_{mn} \cos\left(\frac{\pi m}{L_x} x\right) \cos\left(\frac{\pi n}{L_y} y\right).$$

For the cylindrical cross-section two computations were performed, for the interface resulting from the first azimuthal mode only ( $m = 1$ ):

$$\eta(r, \varphi) = J_1(y_{11}r)(0.002 \cos(\varphi) + 0.003 \sin(\varphi))$$

and for the second azimuthal mode ( $m = 2$ ):

$$\eta(r, \varphi) = J_2(y_{21}r)(0.002 \cos(2\varphi) + 0.003 \sin(2\varphi)).$$

Here  $y_{11} = 1.84118378134237925$  and  $y_{21} = 3.05423692822714087$ .

Fig. 4.2 a) shows the case  $m = 1$  (top view). The interface and the corresponding magnetic field are presented. In Fig. 4.2 b) the same interface is displayed.

The tilted interface produces a electrical current distribution which can be hardly

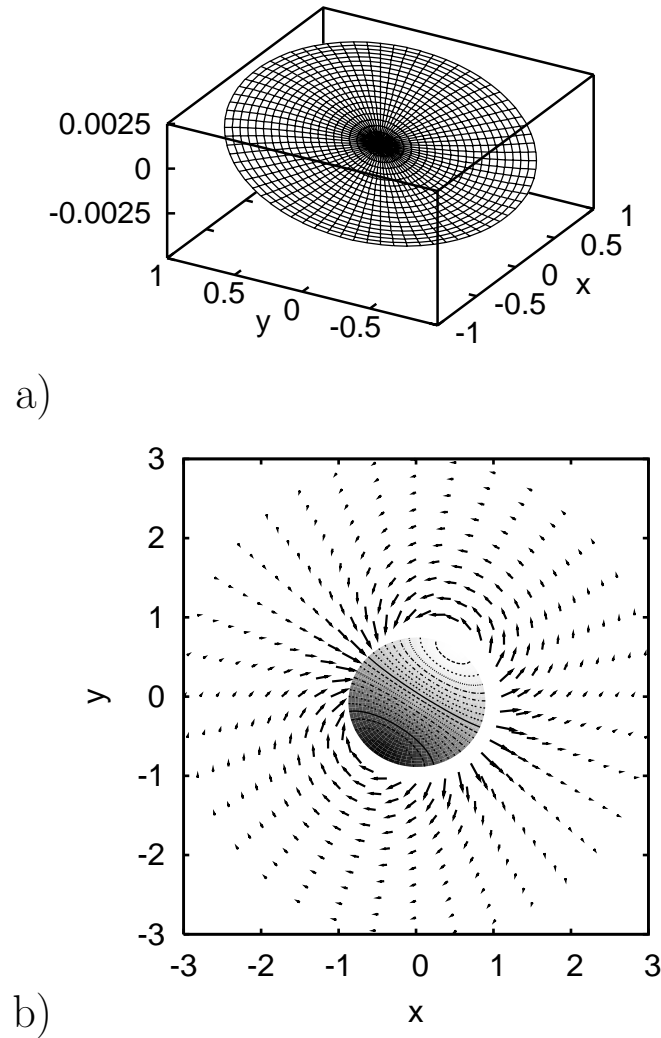


Figure 4.2: Perturbed magnetic field in a circular domain. The interface contains only first azimuthal mode ( $m = 1$ ). a) 3D-representation of the perturbed interface  $\eta(r, \varphi)$ . b) Magnetic field perturbation in the plane  $z = 1$ .

simplified as the perturbed electrical current flowing from the maximum of interface to the point of minimum in the first fluid. In the second fluid the currents flow in the opposite direction. There is a vortex of electrical current, which induces the perturbed magnetic field. The structure of the perturbed magnetic field is similar to the magnetic field of a coil with electrical current.

Fig. 4.3 represents the more complicated case for the interface formed by the second azimuthal mode ( $m = 2$ ). There are four electrical current vortices flowing

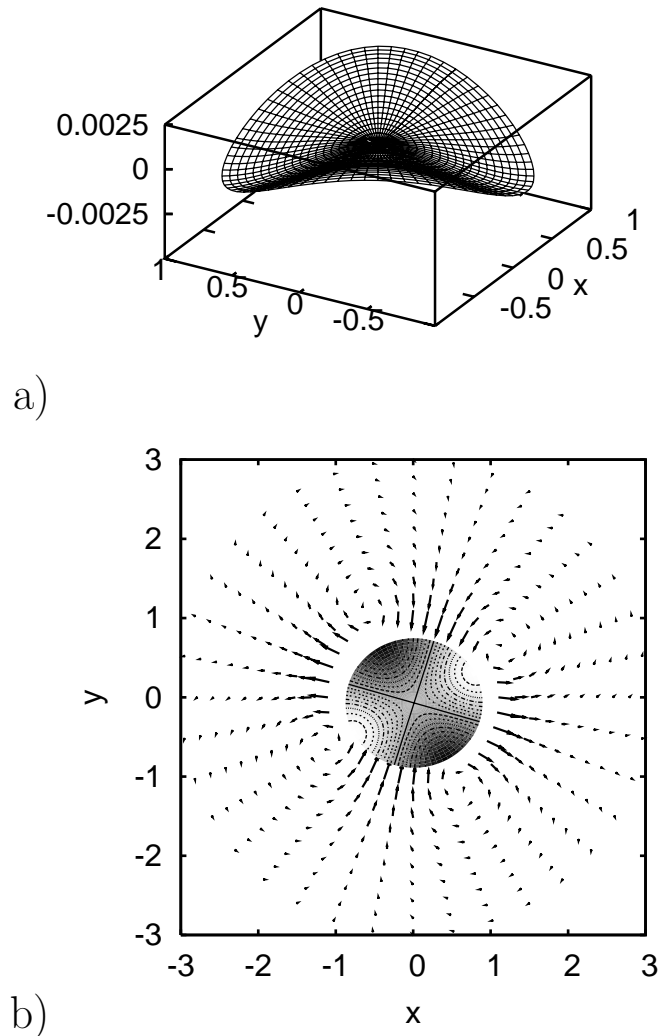


Figure 4.3: Perturbed magnetic field in a circular domain. The interface contains only second azimuthal mode ( $m = 2$ ). a) 3D-representation of the perturbed interface  $\eta(r, \varphi)$ . b) Magnetic field perturbation in the plane at  $z = 1$ .

from two ridges on the interface to the two minimums on the interface. It is similar to the existing of four electrical current coils.

Fig. 4.4 shows the case of the rectangular cross-section. The interface (see Fig.4.4 a)) is formed by the one-dimensional mode ( $m = 0, n = 1$ ):

$$\eta(x, y) = 0.001 \cos\left(\frac{\pi}{L_y}y\right).$$

The corresponding to it magnetic field is shown in Fig.4.4 b). Fig. 4.5 shows the

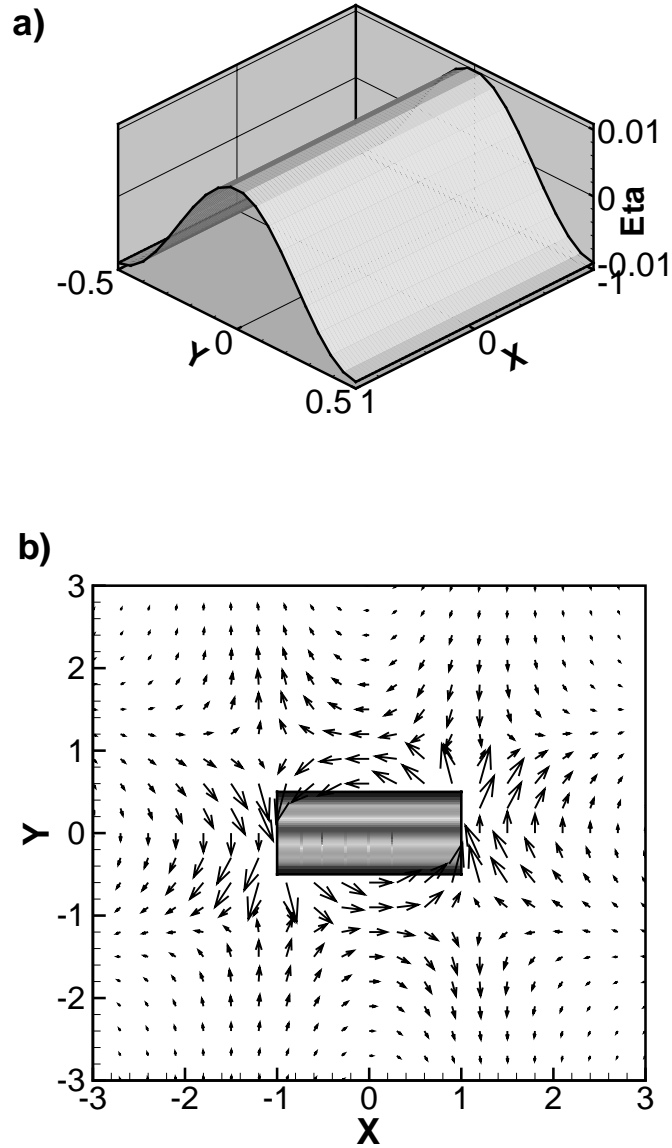


Figure 4.4: Perturbed magnetic field in a rectangular domain. The single one-dimensional mode forms the interface. a) 3D-representation of the perturbed interface  $\eta(x, y)$ . b) Magnetic field perturbation in the plane  $z = 1$  (view from above). In centrum the rectangular domain with perturbed interface is shown.

interface and corresponding to it magnetic field for a single two-dimensional mode ( $m = 1, n = 1$ ):

$$\eta(x, y) = 0.001 \cos\left(\frac{\pi}{L_x}x\right) \cos\left(\frac{\pi}{L_y}y\right).$$

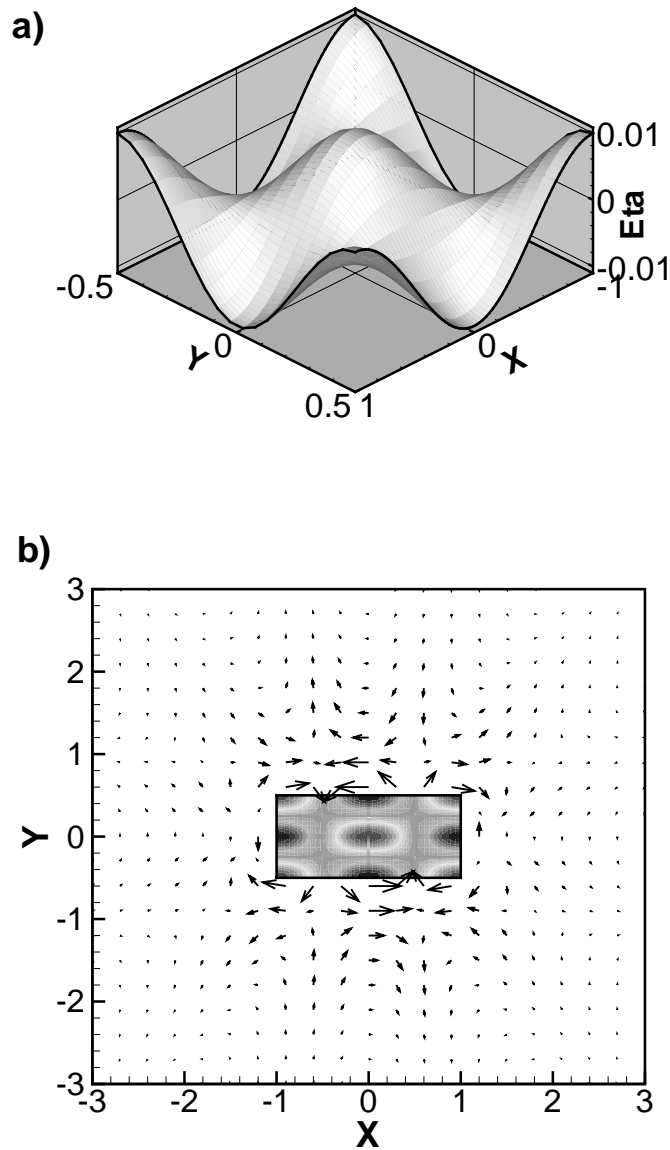


Figure 4.5: Perturbed magnetic field in a rectangular domain. The single two-dimensional mode forms the interface. a) 3D-representation of the perturbed interface  $\eta(x, y)$ . b) Magnetic field perturbation in the plane  $z = 1$  (view from above). In centrum the rectangular domain with perturbed interface is shown.



## 4.4 Conclusions

A semi-analytical method for the computation of the electrical current perturbation and magnetic field perturbation in a rod with non-conducting walls and applied vertical electrical current was developed. The method can be applied to arbitrary forms of the cross-section. In comparison to numerical solution (finite-elements based, for example, which is available in the most codes) the represented method gives the possibility to a direct computation of the perturbation of the electrical current perturbation and magnetic field at the prescribed positions. The described analytical solution can be useful for stability analysis of aluminium reduction cells because the instabilities in the aluminium reduction cells are produced by the perturbed electrical current or perturbed magnetic field [17]. The presented solution can also be used as solution of the forward problem for the reconstruction of the interface in the two-fluids system from the magnetic field measurement.



# Chapter 5

## Conclusions

Two important problems have been treated in this thesis, namely the stability of an aluminium reduction cell and the problem of reconstruction of an aluminium-cryolite interface.

In chapter 2 of this thesis, the stability of an aluminium reduction cell in the presence of a mean flow is investigated. Simplified model of an Alu-cell is used in order to obtain the analytical solutions. The basic equations are derived on the basis of the two-dimensional modeling in the shallow water approximation. A normal mode analysis is performed with respect to the perturbation of the interface and perturbation of the electrical potential. Four non-dimensional parameters are found, which influence the instability threshold. A critical dimensionless velocity of the mean flow and MHD-parameter, form the instability thresholds. The other two parameters, a dimensionless aspect ratio and a material property parameter, also influence the two instability thresholds. Two types of the instability are studied using this model, namely the MHD-instability and the Kelvin-Helmholtz instability. No interaction between both instabilities concerning their instability thresholds were found. However, the direction of propagation of interfacial waves is changed in the presence of magnetic field due to the Lorentz forces. The particular case with a large aspect ratio (it corresponds to a very wide channel) is studied in Appendix **A**. It was proved, that the linearized governing equations have unstable solutions always in the presence of magnetic field for such system.

In chapter 3 a new deterministic algorithm is developed for the problem of interface reconstruction from electrical potential measurement. The interface shape

is represented as a set of orthonormal functions (modes), that allows to obtain an analytic solution to the forward problem. The solution of the inverse problem is based on two comparatively simple operations, namely Fourier decomposition and matrix inversion using singular value decomposition. The optimal number of modes which should be used for reconstruction is obtained using the L-curve criterion, which represents a compromise between data error and solution norm, in other words, between the good approximation of the measurement and smoothness of the reconstructed interface. The good reconstruction results are obtained with a very small number of modes. A good reconstruction quality is achieved and the reconstructed interfaces are similar to the exact interface. The key point of the presented algorithm is that it is used for reconstruction only a few number of a modes without loss of the reconstruction quality. Therefore, the algorithm is very fast and robust in respect to the measurement error. Because of its simplicity and unexcelled quickness of the represented method, it has the best chance to be used as a part of a real-time reconstruction system with application in the aluminium reduction cells.

In chapter 4 the forward problem of reconstruction of the interface in Alu-cells using the magnetic field measurement outside the cell is treated. A semi-analytical method for the computation of the perturbed magnetic field and perturbed electrical current in a rod with insulating walls is presented. This analysis is valid for an arbitrary form of the cross-section and therefore can be easily applied to the aluminium reduction cells. Two examples of computations are shown, for a cylindrical rod and for a rod with rectangular cross-section. The advantages of the described method is that the perturbation can be directly computed with a good accuracy. For a moderate number of data points, the method will be faster in comparison to the electromagnetic solver based on the numerical solution. The presented semi-analytical solver can be used as a part of a system which performs a reconstruction of the interface shape from the magnetic field measurement.

# Chapter 6

## Appendix

### 6.1 Appendix A: Linear stability analysis in the half-bounded system

#### 6.1.1 Formulation of the stability problem

The statement of the problem is shown in Fig. 6.1. It is a particular case of the system which is described in chapter 2. It corresponds to the case when the channel walls are far away from each other. Two thin layers of the fluids with the different electrical conductivities and densities are superimposed. We assume that the fluids are bounded only with one wall. As in chapter 2, the vertical homogeneous electrical current and magnetic field are applied. Initially the interface between the fluids is at rest and the uniform flow in the lower fluid is assumed. The upper fluid is also at rest in the steady state.

It is obvious, that in such system two types of instability can appear, the Kelvin-Helmholtz and the MHD instability. The details of the presented stability analysis and the description of the instability mechanisms are described in chapter 2. In this part of the thesis only the deriving of the stability equations and obtained results are presented.

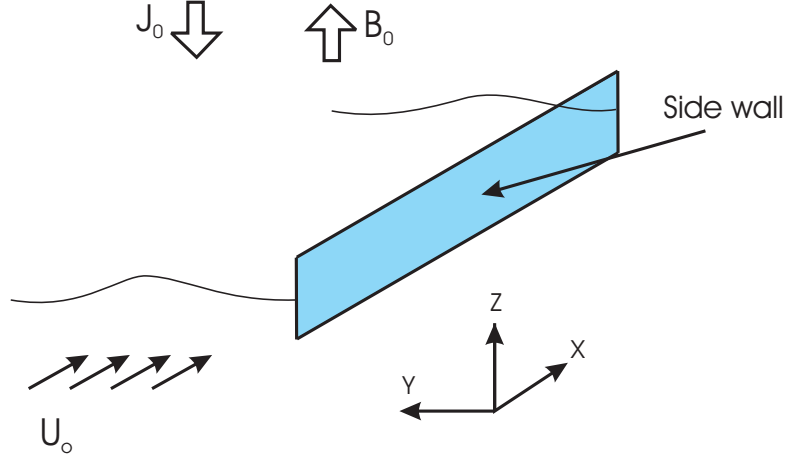


Figure 6.1: Half-bounded system. Statement of the stability problem.

### 6.1.2 Basic equations

The presented model is based on the shallow water approximation [51]. The approximation is based on the assumption that the layer thicknesses are small, i.e.,

$$h, H \ll \lambda, \quad (6.1)$$

where  $\lambda$  is the typical length scale of interfacial perturbations, and  $h$  and  $H$  are the thicknesses of cryolite and aluminium layers, respectively. Taking into account the Lorentz force in the aluminium  $\mathbf{F}_a = -\sigma_a B_0 \nabla_{\perp} \phi$  due to the interaction of the electric current perturbation  $\mathbf{j}_a = -\sigma_a \nabla \phi$  with the magnetic field  $B_0 \mathbf{e}_z$ , the nonlinear shallow water equations governing the fluid motions can be written as [71]:

$$\frac{\partial \mathbf{u}_a}{\partial t} + (\mathbf{u}_a \cdot \nabla) \mathbf{u}_a = -\frac{\nabla p}{\rho_a} - g \nabla \eta - \sigma_a \frac{B_0}{\rho_a} \nabla_{\perp} \phi \quad (6.2)$$

$$\frac{\partial \mathbf{u}_c}{\partial t} + (\mathbf{u}_c \cdot \nabla) \mathbf{u}_c = -\frac{\nabla p}{\rho_c} - g \nabla \eta \quad (6.3)$$

$$\frac{\partial \eta}{\partial t} + \nabla \cdot [(H + \eta) \mathbf{u}_a] = 0 \quad (6.4)$$

$$\nabla \cdot [(H + \eta) \mathbf{u}_a + (h - \eta) \mathbf{u}_c] = 0 \quad (6.5)$$

$$\nabla^2 \phi = -\frac{J_0 \eta}{\sigma_a H h} \quad (6.6)$$

## 6.1. Appendix A: Linear stability analysis in the half-bounded system 73

where  $\nabla_{\perp} = \mathbf{e}_x \partial / \partial y - \mathbf{e}_y \partial / \partial x$ . The shallow-water approximation eliminates the  $z$ -dependence, so all equations are two-dimensional. Indices "a" and "c" refer to aluminium and cryolite respectively.  $\mathbf{u}_a(x, y, t)$  and  $\mathbf{u}_c(x, y, t)$  are the vertically averaged horizontal velocities in corresponding layers,  $p(x, y, t)$  is the pressure at the interface  $z = \eta(x, y, t)$ , and  $\phi(x, y, t)$  is the perturbation of the electrical potential. In the system (6.2) - (6.6), equations (6.2) and (6.3) are the momentum equations, (6.4) describes the evolution of the interface, (6.5) imposes the mass conservation condition, and (6.6) provides the link between the deflection of interface and perturbations of electrical current. The boundary conditions are

$$u_{ay} = u_{cy} = \frac{\partial \phi}{\partial y} = 0 \quad \text{at } y = 0 \text{ and } y = L \quad (6.7)$$

The first two conditions are the conventional free slip conditions at the channel walls, while the last condition describes electrically non-conducting channel walls. Equations (6.2-6.6) admit an exact stationary solution

$$\mathbf{u}_a = U_0 \mathbf{e}_x, \quad \mathbf{u}_c = 0, \quad p = \eta = \phi = 0 \quad (6.8)$$

whose stability with respect to infinitesimal perturbations we want to investigate.

The derivation of the stability equations is performed using the analysis described in chapter 2. The basic equations are linearized, the unknown quantities are represented as a sum of a mean and perturbation, and the normal mode analysis is performed. Based on this methods, the following dimensionless stability equations are derived:

$$(D^2 - \kappa^2) \hat{\eta} = 0 \quad (6.9)$$

$$(D^2 - k^2) \hat{\phi} = 0 \quad (6.10)$$

and four boundary conditions

$$D \hat{\eta} - i N k \hat{\phi} = 0 \quad \text{at } y = 0 \quad (6.11)$$

$$D \hat{\phi} = 0 \quad \text{at } y = 0 \quad (6.12)$$

$$\hat{\eta} = \hat{\phi} = 0 \quad \text{at } y = \infty \quad (6.13)$$

Here  $k$  is the wavenumber,  $D = d/dy$ . The following abbreviation is introduced:  $\kappa^2 = k^2(c^2 - 2\xi Mc - 1 + \xi M^2)$ . The stability equations (6.9-6.10) contain the non-dimensional numbers:

$$M = \frac{U_0}{c_0}$$

is the dimensionless velocity of the mean flow.

$$N = \frac{J_0 B_0 H}{(\rho_a - \rho_c)gh}$$

is the main stability parameter. It describes the ratio between destabilizing electromagnetic forces and stabilizing influence of gravity. The parameter

$$\xi = \frac{1}{1 + \frac{\rho_c H}{\rho_a h}}$$

contains the thicknesses of the fluid layers and densities of the fluids.

### 6.1.3 Solution of the stability problem

The general solutions of the stability equations are

$$\hat{\eta}(y) = Ae^{-\kappa y} \quad (6.14)$$

$$\hat{\phi}(y) = \frac{Ae^{-\kappa y}}{-\kappa^2 + k^2} + Be^{-\kappa y} \quad (6.15)$$

where  $A$  and  $B$  are the unknown constants. Applying the boundary conditions (6.11-6.13), we obtain the following system of equations:

$$\underbrace{\begin{pmatrix} \kappa + \frac{iNk}{-\kappa^2 + k^2} & iNk \\ \frac{\kappa}{-\kappa^2 + k^2} & k \end{pmatrix}}_{\mathbf{Q}} \begin{pmatrix} A \\ B \end{pmatrix} = 0 \quad (6.16)$$

The system has non-trivial solution only in the case  $\det[\mathbf{Q}] = 0$ . From this condition we obtain the defining equation for  $\kappa$ :

$$\kappa^3 - (k^2 - iN)\kappa - iNk = 0 \quad (6.17)$$



## 6.1. Appendix A: Linear stability analysis in the half-bounded system 75

which has two solutions

$$\kappa_1 = -\frac{k}{2} - \sqrt{-iN + \frac{k^2}{4}}$$

$$\kappa_2 = -\frac{k}{2} + \sqrt{-iN + \frac{k^2}{4}}$$

Non-dimensional velocity of waves is

$$c_{1,2} = \xi M \pm \sqrt{1 - M^2(\xi - \xi^2) - \frac{\kappa^2}{k^2}} \quad (6.18)$$

Imaginary part of complex velocity  $c(N, M, \xi, k) = c_r + c_i$  describes stable ( $c_i < 0$ ) or unstable ( $c_i > 0$ ) waves. The condition  $c_i = 0$  defines a marginal stability curve.

### 6.1.4 Discussion of the results

Let us at first consider the general case  $N \neq 0$ ,  $M \neq 0$ . Fig 6.2 shows the real and imaginary parts of dimensionless dispersion relation (6.18). Let us now consider the

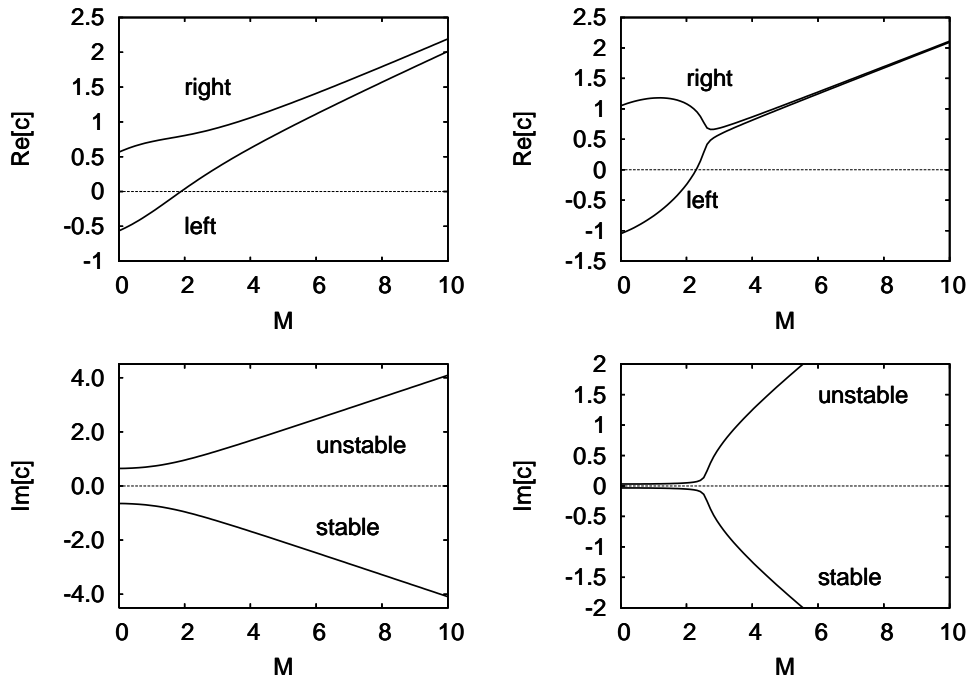


Figure 6.2: Half-bounded system. Dispersion relation of internal gravity waves at fixed wavenumber  $k = 0.5$  in two-fluid system with vertical magnetic field. Lower fluid moves with constant velocity.  $N = 0.1$ ,  $\xi = 0.2102$ .

particular case of pure Kelvin-Helmholtz instability,  $N = 0$ ,  $M > 0$ . Fig. 6.3 shows the dispersion relation for this case. Kelvin-Helmholtz instability appears if the

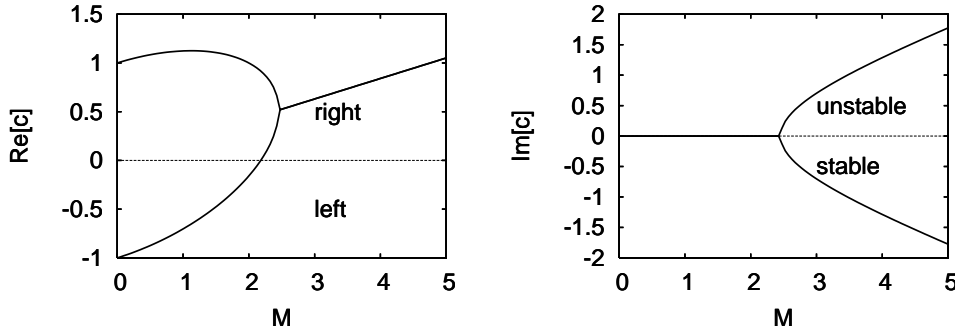


Figure 6.3: Half-bounded system. Dispersion relation of internal gravity waves at fixed wavenumber  $k = 0.5$ . Pure Kelvin-Helmholtz instability ( $N = 0$ ).  $\xi = 0.2102$ .

mean flow velocity  $M > M_c$ . Critical velocity  $M_c$  can be obtained from condition  $\text{Im}[c] = 0$  (see eq. 6.18) after substituting of exact solution for this case  $\kappa = 0$ :

$$M_c = \sqrt{\frac{1}{\xi - \xi^2}} \quad (6.19)$$

Critical mean flow velocity is for half-bounded system identical with critical mean flow velocity for one-dimensional waves in the channel.

Now we consider the particular case of pure MHD instability ( $M = 0$ ). Fig. 6.4 shows the relation corresponding to this case dispersion. We note, that the waves are always unstable if  $N > 0$ .

The mechanism of instability onset is very interesting. In the absence of Lorentz force there exist gravitational modes with different transverse wavenumber  $n$ . The key of understanding of instability onset is the interaction of two modes with  $n = 0$  [see Fig. 6.5 (a)] and  $n = 1$ . As  $N$  increases the mode with  $n = 0$  changes its shape under the influence of Lorentz force [see Fig.6.5 (b)]. This new mode has transverse wavenumber  $n = 1$  and its shape is identical to those of the existing gravitational mode with  $n = 1$ . Its oscillation frequency, however, is at small  $N$  different from that of the "old" gravitational mode with  $n = 1$ . If  $N$  increases further, the two complex frequencies of "new" and "old" modes with  $n = 1$  converge on the real axis. At  $N = N_c$ , the two frequencies meet and move off into the complex plane resulting

## 6.1. Appendix A: Linear stability analysis in the half-bounded system 77

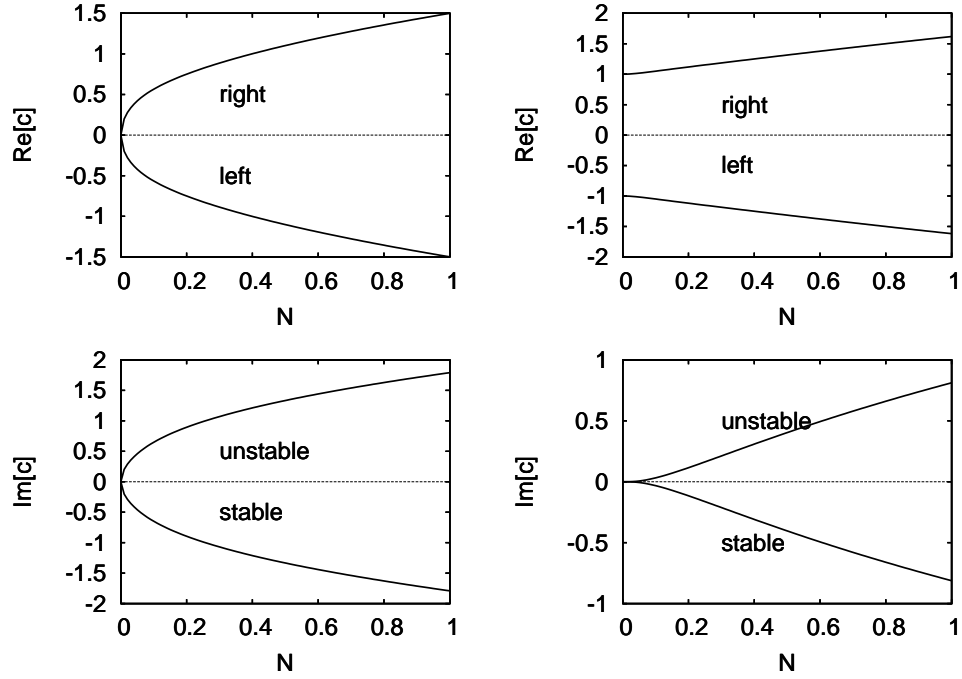


Figure 6.4: Stability of waves in half-bounded system. Dispersion relation of internal gravity waves with fixed wavenumber  $k = 0.5$  in two-fluid system. Pure MHD instability ( $M = 0$ ).  $\xi = 0.2102$ .

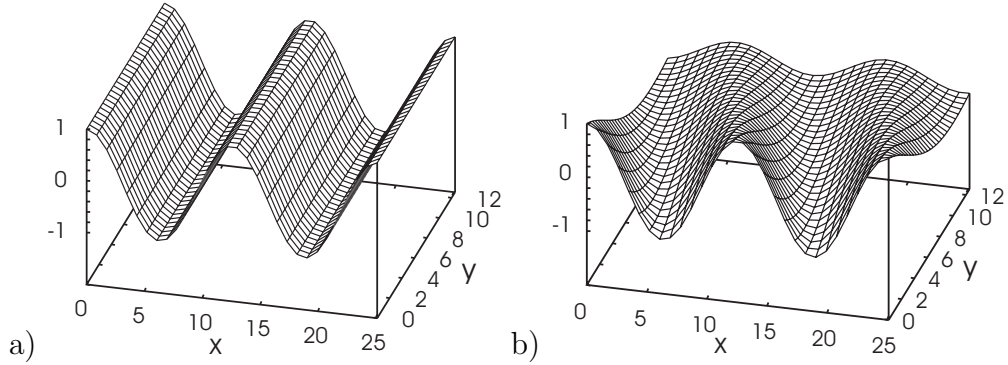


Figure 6.5: Stability of waves in half-bounded system. Interface shape for a wave at wavenumber  $k = 0.5$ . a) stable state ( $N=0$ ). b) unstable state ( $N=0.2$ ). The wave shape is distorted by the Lorentz forces.

one unstable and one stable mode.

A similar instability scenario was described by Davidson & Lindsay [18] for the mechanical counterpart of the system (the so-called compound pendulum). In their model, two arbitrary gravitational modes are modified by the Lorentz force so

that their complex frequencies coincide on the real axis and then move off into the complex plane. Contrary to the pendulum model we do not observe the interaction between any other modes than the two with  $n = 0$  and  $n = 1$ . It can be explained by the fact, that the pendulum model explains the instabilities in the rectangular cell with finite dimensions while our model deals with an infinitely long channel.

## 6.2 Appendix B: EIT Patents

In this part of thesis some EIT patents are briefly described. Although the method of EIT is principally known and well studied, there exist a lot of problems connected with the minimizing of measurement noise [10], optimization of measurement due to using of optimal currents set [37]. An interesting application of EIT is the determining of external shape of body which is represented in [11].

**US patent 5311878, Real-time electrical impedance tomography system [10].** An online system for imaging the electrical properties of humans body is presented in this invention (see Fig. 6.6). The application is the real-time imaging of the blood flow or the observation of the lung resistivity variations during respiratory and cardiac cycles. The changing of the resistivity in the lungs at the respiration

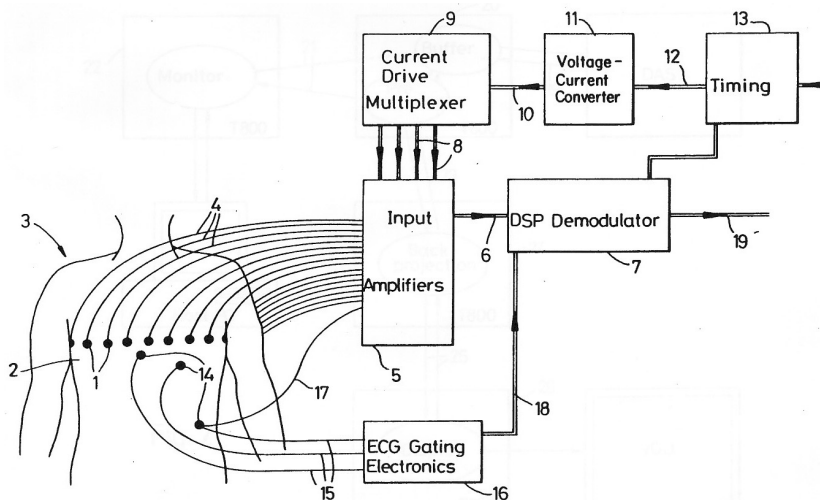


Figure 6.6: Real-time electrical impedance tomography system.

is small (2%). However, the low noise level of the apparatus allows to observe the small changes of resistivity small as 0.5%. The system can be used to monitor oc-

currence of pulmonary embolism. The authors claim a method and apparatus of invention. The device contains pairs of surface electrodes. A constant electrical current is applied to selected electrodes. The electrical potential is measured between adjacent pairs of other electrodes. An algorithm of reconstruction is implemented as a single matrix multiplication of the measured data with a weighting matrix. The measurement noise is minimized by special means, such a demodulation of the potential measurements by digital signal processing and synchronous measurement of the drive current and electrical potentials, and then dividing the drive current into potential measurement before the signal processing.

**US patent 5381333, Current patterns for electrical impedance tomography [37].** This patent is devoted to question how the reconstruction quality of an EIT system can be improved. A method and apparatus are invented for the producing of optimal current pattern and optimal imaging of the impedance distribution inside the body.

The current patterns which are applied to the electrodes should contain the maximum amount of information about the internal impedance distribution in the body under imaging. However, the optimal current patterns depend on the unknown at the beginning of experiment internal impedance distribution. The authors propose a method for producing of optimal current patterns for the body under consideration. At the same time the internal impedance distribution will be reconstructed.

The flowchart shown in the Fig. 6.7 represents the algorithm for producing the optimal current pattern. In the first step an initial guess (typically uniform distribution) of electrical conductivity in the body under consideration is assumed. Then the set of orthogonal current patterns is applied to the electrodes. The resulting voltages are measured on all electrodes and a norm called "distinguishability" is computed. The next step is the computing of the theoretical voltages on the electrodes with assumed conductivity distribution. From the difference of theoretical and measured voltage the new current set is computed. The represented iterative process converges rapidly. The result is the optimal current patterns and the conductivity distribution which is imaged with this optimal currents set.

**US patent 5184624, Electrical impedance tomography [11].** A method for determining external shape of a body with help of EIT is claimed in this patent.

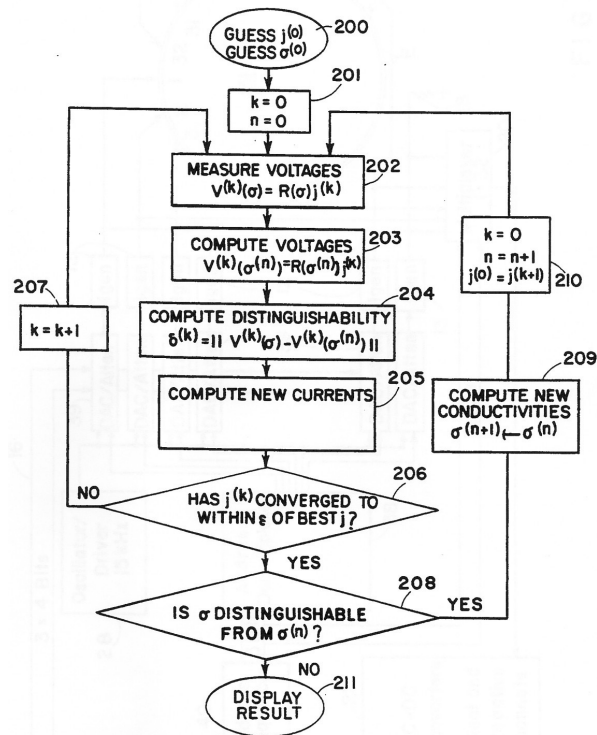


Figure 6.7: Current patterns for electrical impedance tomography.

$N$  electrodes are connected to the body surface (see Fig. 6.8). The electrical currents are applied to the adjacent electrodes and the voltages are measured at the other electrodes. In the beginning the circular boundary is assumed. During the measurement new distances between electrodes are computed and a new boundary is estimated. For a computation of a boundary an empirical ansatz is used. The process ends if the boundary does not change. The method presented is not sensitive to the internal conductivity distribution. Faster convergence can be obtained if the starting body is similar to the required.

### 6.3 Appendix C: Inverse problem of interface reconstruction: uniqueness proof

This part of appendix deals with the problem of interface reconstruction described in chapter 3, where the interface shape is reconstructed from the electrical potential perturbation measured on the cylinder walls (for the details see the chapter 3). It will

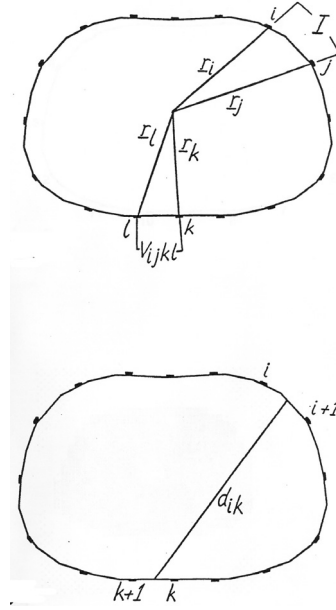


Figure 6.8: Determining of external shape with EIT.

be shown here that there is a unique correspondence between the interface deflection  $\eta(r, \varphi)$  and the electrical potential perturbation  $\phi(\varphi, z)$  at the wall. This is a very important question, because this implies the uniqueness of the reconstruction. A non-unique mapping would make an exact reconstruction impossible, as it happens in many inverse problems. For example if we want to recover the interface shape from the data set of the magnetic field outside the fluid region we would not be able to reconstruct the axisymmetric component of the interface. The axisymmetric interface shape leads to axisymmetric electrical current perturbation which does not produce any changes of the magnetic field outside the fluid region. Thus, one cannot detect an axisymmetric interface from the magnetic field measurement outside the fluid. But we can recover it from the electrical potential measurement as at will be shown below.

We start from the simple case of the axisymmetric interface and will extend the proof to the non-axisymmetric case. The mapping of the interface perturbation into the electrical potential at the cylinder wall is

$$\phi(z) = \sum_{n=1}^N \eta_n J_0(y_n) e^{-y_n z} \quad (6.20)$$

We can rewrite this expression as

$$\phi(z) = \sum_{n=1}^N a_n e^{-y_n z} \quad (6.21)$$

where  $a_n = \eta_n J_0(y_n)$ . We introduce a vector  $\mathbf{a}$  such that  $\mathbf{a} = (a_1, a_2, \dots, a_n)$ .

To demonstrate the uniqueness of the mapping one has to prove that  $\forall \mathbf{a}_1 \neq \mathbf{a}_2 : \phi_1(z) \neq \phi_2(z)$ , i.e. it does not exist two different vectors  $\mathbf{a}_1 \neq \mathbf{a}_2$  which would lead to the same functions  $\phi_1(z) = \phi_2(z)$ . It is therefore necessary to show that the function  $\phi(z)$  must be non-zero for any non-zero vector  $\mathbf{a}$ . This is an equivalent to the fact that the functions  $e^{-y_n z}$  are linearly independent.

The functions are linearly independent if the Wronski-determinant is non-zero [8]. The Wronski-determinant of the functions  $e^{-y_n z}$  is

$$\det \mathbf{W} = \begin{vmatrix} e^{-y_1 z} & e^{-y_2 z} & \dots & e^{-y_n z} \\ -y_1 e^{-y_1 z} & -y_2 e^{-y_2 z} & \dots & -y_n e^{-y_n z} \\ \dots & \dots & \dots & \dots \\ (-y_1)^{(n-1)} e^{-y_1 z} & (-y_2)^{(n-1)} e^{-y_2 z} & \dots & (-y_n)^{(n-1)} e^{-y_n z} \end{vmatrix}. \quad (6.22)$$

This determinant can be transformed to

$$\det \mathbf{W} = \prod_{n=1}^n e^{-y_n z} \begin{vmatrix} 1 & 1 & \dots & 1 \\ -y_1 & -y_2 & \dots & -y_n \\ \dots & \dots & \dots & \dots \\ (-y_1)^{(n-1)} & (-y_2)^{(n-1)} & \dots & (-y_n)^{(n-1)} \end{vmatrix}. \quad (6.23)$$

The right part of the last expression is a Vandermonde-matrix whose determinant is always non-zero if the elements of this matrix are non-equal [27]. The left part of the last expression is non-zero, too. Thus, we have proved that the Wronski-determinant (6.22) is non-zero and from this the linear independence of the functions  $e^{-y_n z}$  in equation (6.21) follows. From that the fact of the non-nullity of the expression (6.20) follows. Thus, the mapping of the axisymmetric interface into the electrical potential is unique.

The non-axisymmetric interface can be represented as a superposition of single interfaces where every single interface consists of the radial modes for only one



azimuthal mode:

$$\eta(r, \varphi) = \sum_{m=-M}^M \eta_m(r, \varphi) \quad (6.24)$$

where  $\eta_m(r, \varphi) = \sum_{n=1}^N \eta_{mn}(r, \varphi)$ . It can be easily proved, that any single interface  $\eta_m(r, \varphi)$  is uniquely mapped into the potential perturbation. Thus, the non-axisymmetric interface is also uniquely mapped into electrical potential perturbation in the fluid.

## 6.4 Appendix D: Bessel functions as the set of orthonormal functions describing the interface separating fluids in a cylinder.

In this part of appendix it is to be shown that the interface between two fluids in a rod with cylindrical cross-section can be described as a superposition of Bessel functions. The equations describing the interface will be derived directly from the equations of fluid mechanics.

The problem at hand is shown in the Figure 6.9. The two inviscid incompressible fluids with the different densities  $\rho_1$  (upper) and  $\rho_2$  (lower) are situated in an infinite cylinder. We consider further only the gravity forced waves. The radius of the cylinder is large comparatively with the capillary length and the capillary effects can be neglected. The surface tension is neglected. The amplitudes of the waves are small compared with the wave length and with the cylinder radius.

We start from the Euler equation and the mass conservation law:

$$\rho \frac{\partial \mathbf{v}}{\partial t} + \rho(\mathbf{v} \cdot \nabla) \mathbf{v} = -\nabla p - g \mathbf{e}_z \quad (6.25)$$

$$\nabla \cdot \mathbf{v} = 0 \quad (6.26)$$

where  $\mathbf{v}$  is the velocity,  $\rho$  - the density,  $p$  - the pressure and  $g$  - gravity acceleration. We assume irrotational flow ( $\nabla \times \mathbf{v} = 0$ ) and express the velocity as the gradient of a scalar velocity potential  $\phi$  (we have in the problem at hand the inviscid irrotational

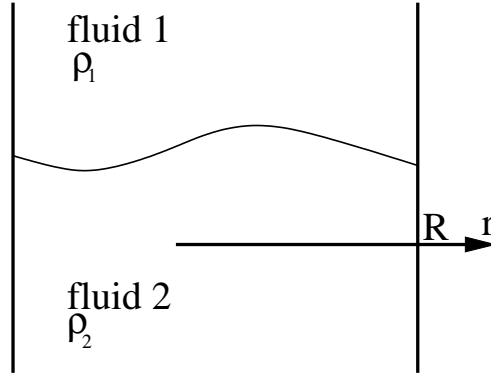


Figure 6.9: Reconstruction of interface. Derivation of a set of orthonormal functions describing the interface.

flow):

$$\mathbf{v} = \nabla\phi \quad (6.27)$$

The velocity potential in this subsection should not be confused with the electrical potential in the previous sections. Substituting the expression (6.27) in the equations (6.25) and (6.26), we obtain:

$$\rho \frac{\partial}{\partial t} \nabla\phi + \nabla \frac{\rho}{2} (\nabla\phi)^2 = -\nabla p - \nabla \rho g z \quad (6.28)$$

We integrate the last expression and obtain

$$\rho \frac{\partial\phi}{\partial t} + \frac{\rho}{2} (\nabla\phi)^2 = -p - \rho g z + c(t) \quad (6.29)$$

where the function  $c(t)$  can be omitted by redefining  $\phi$  without the changing of the velocity field [44]. We neglect the non-linear term in the last equation and obtain:

$$p = -\rho g z - \rho \frac{\partial\phi}{\partial t} \quad (6.30)$$

The equation (6.26) is changed to

$$\Delta\phi = 0 \quad (6.31)$$

The velocity potential in the studied system satisfies the following boundary condi-

tions:

$$\phi_1 = \phi_2 = 0 \quad z = \pm\infty \quad (6.32)$$

$$\frac{\partial\phi_1}{\partial r} = \frac{\partial\phi_2}{\partial r} = 0 \quad r = R \quad (6.33)$$

The harmonic function, which satisfies the Laplace-equation (6.31) at the conditions (6.32) and (6.33), has the form:

$$\phi_i = C_i J_m(k_{mn}r) e^{-k_{mn}|z| + im\varphi - i\omega t} \quad (6.34)$$

where constants  $C_i$  can be complex;  $J_m$  is the Bessel function of the first kind,  $k_{mn} = y_{mn}/R$ ,  $y_{mn}$  is the  $n$ -th solution of the equation  $J'_m(r) = 0$  at  $m > 0$  and  $(n + 1)$ -th solution at  $m = 0$ . In the case  $m = 0$  we neglect the solution  $r = 0$  because this solution corresponds to the plane surface  $\eta(t) = const$ . One has to find the interface  $\eta$  and possible values of the frequency  $\omega$ . We consider the equation (6.30) at the boundary conditions  $p_1 = p_2$  at  $z = \eta$  (pressure continuity) and obtain:

$$\eta = \frac{1}{g(\rho_2 - \rho_1)} \left( \rho_1 \frac{\partial\phi_1}{\partial t} - \rho_2 \frac{\partial\phi_2}{\partial t} \right) \quad (6.35)$$

Substituting the expression (6.34) in (6.35), we have:

$$\eta = C \frac{\omega}{g} J_m(k_{mn}r) e^{im\varphi} \sin\omega t \quad (6.36)$$

The possible values of frequency  $\omega$  can be obtained from (6.35) at the following boundary conditions:

$$\frac{\partial\phi_1}{\partial z} = \frac{\partial\phi_2}{\partial z} \quad z = 0 \quad (6.37)$$

$$\frac{\partial\phi_i}{\partial z} = \frac{\partial\eta}{\partial t} \quad z = 0 \quad i = 1, 2 \quad (6.38)$$

The first condition (6.37) shows the continuity of the velocity normal component at the interface  $z = \eta$ . The second (6.38) is obtained from the kinetic boundary condition with neglecting the non-linear terms. More details see in [42]. Thus, for the infinite deep fluids it is valid

$$\omega = \sqrt{k_{mn}g \frac{\rho_2 - \rho_1}{\rho_2 + \rho_1}} \quad (6.39)$$

The equation (6.39) produces an elementary interface perturbation. The complete interface perturbation is a superposition of the elementary perturbations:

$$\eta(r, \varphi) = \sum_{m=-M}^M \sum_{n=1}^N \eta_{mn} J_m(k_{mn}r) e^{im\varphi} \quad (6.40)$$

We call the value  $n$  as the radial mode number and the value  $m$  as the azimuthal mode number. Although the quantity of the radial and azimuthal modes is usually unlimited, the highest modes have the small amplitudes decaying as [26]

$$\langle |\eta_k|^2 \rangle \sim k^{-7/2}$$

where  $k$  is the wavenumber. Therefore the higher modes can be often (depending on the problem) neglected.

## 6.5 Appendix E: Reconstruction of interfaces between electrically conducting fluids from electrical potential measurements. A.Kurenkov and A.Thess. *Proc. of the PAMIR Conference, 2000, France.*

### 6.5.1 Introduction

There are a variety of problems in materials processing where it would be useful to know the time-dependent distribution of the electrical conductivity of a single fluid or a multiphase flow. For instance, the knowledge of the exact position of the interface between highly conducting molten Aluminum and poorly conducting liquid Cryolite is important to prevent unwelcome instabilities in Aluminum reduction cells [19]. Other examples include electrical conductivity distributions in glass melting furnaces, metal-slag interfaces in steel and ironmaking as well as on-line detection of inclusions [32].

The statement of the considered problem is schematically shown in Fig. 6.10,

left. Two fluids with different electrical conductivities  $\sigma_1$  (upper) and  $\sigma_2$  (lower) are situated in an infinite cylinder with the radius  $R$ . The cylinder walls are non-conducting. Along the axis of the cylinder a homogeneous electrical current with density  $J_0$  is applied.

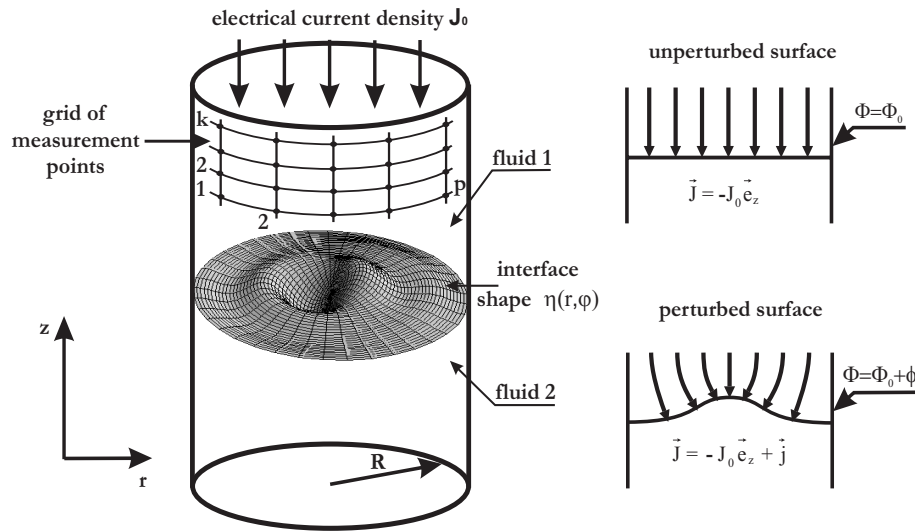


Figure 6.10: Definition of the problem.

If the interface between the fluids is flat, the electrical current  $\mathbf{J}$  is homogeneous everywhere as shown in the upper right part of Fig. 6.10. In this case the total electrical potential  $\Phi$  is equal to the electrical potential  $\Phi_0$ , induced by the applied electrical current  $J_0$ . As soon as the interface deviates from its flat shape due to interfacial waves or an external forcing, the electrical current density  $\mathbf{J}$  will become nonhomogeneous (lower right part of Fig. 6.10). This inhomogeneity can be represented by the perturbation of electrical current density  $\mathbf{j}$  (where  $\mathbf{J} = \mathbf{J}_0 + \mathbf{j}$ ) and it induces a perturbation of the electrical potential  $\phi$  (where  $\Phi = \Phi_0 + \phi$ ). The question as to whether we can reconstruct the interface shape from measurements of  $\phi$  at the wall represents the central focus of our work.

We will distinguish two tasks in further discussion. The first task, the so-called forward problem, concerns the calculation of the electrical potential in the fluids from the interface perturbation. The second task, the so-called inverse problem, is devoted to the reconstruction of the interface shape from the electrical potential at the fluid-cylinder boundary.

## 6.5.2 Forward problem

### The interface perturbation

Assuming that the interface displacement is small ( $\eta \ll R$ ), we can represent it using a complete set of orthonormal functions satisfying the Neumann boundary condition  $\partial\psi_n/\partial r$  at the cylinder walls  $r = R$  [45]. Using the eigenfunctions of the Helmholtz equation as a basis we can write interface displacement in the form

$$\eta(r, \varphi, t) = \sum_{m=-M}^M \sum_{n=1}^N \eta_{mn}(t) J_m(k_{mn}r) e^{im\varphi} \quad (6.41)$$

where  $\eta_{mn}$  is the complex amplitude of the interface modes,  $J_m$  is the Bessel function of the first kind,  $k_{mn} = y_{mn}/R$  and  $y_{mn}$  is the  $n$ -th solution of the equation  $J'_m(r) = 0$  for  $m > 0$  and the  $(n + 1)$ -th solution at  $m = 0$ . In the case  $m = 0$  we omit the solution  $r = 0$  because this solution corresponds to the flat surface  $\eta(t) = const.$

### Electrical potentials in the fluids

The perturbation of electric potential  $\phi$  is obtained from the equations

$$\Delta\phi_1 = \Delta\phi_2 = 0 \quad (6.42)$$

with the system of the boundary conditions [17]

$$\frac{\partial\phi}{\partial r} = 0, \quad r = R \quad (6.43)$$

$$\phi_1 = \phi_2 = 0, \quad z = \pm\infty \quad (6.44)$$

$$\phi_1 - \phi_2 = J_0\eta \left[ \frac{1}{\sigma_2} - \frac{1}{\sigma_1} \right], \quad z = 0 \quad (6.45)$$

$$\sigma_1 \frac{\partial\phi_1}{\partial z} = \sigma_2 \frac{\partial\phi_2}{\partial z}, \quad z = 0 \quad (6.46)$$

The first condition (6.43) expresses the fact of the non-conductivity of the cylinder walls and the second condition (6.44) expresses the vanishing of the electrical potential perturbation for  $z = \pm\infty$ . The last two conditions (6.45)-(6.46) follow from the continuity of the tangential component of the electrical field and the normal

component of the electrical current density respectively at the interface. Then the total potential perturbation in the fluids satisfies

$$\phi_i(r, \varphi, z) = \text{sign}[z] \frac{J_0 \sigma_1 - \sigma_2}{\sigma_i \sigma_1 + \sigma_2} \sum_{m=-M}^M \sum_{n=1}^N \eta_{mn} J_m(k_{mn}r) e^{im\varphi - k_{mn}|z|} \quad (6.47)$$

where  $i = 1$  for the first fluid and  $i = 2$  in the second fluid.

For the axisymmetric interface case ( $m = 0$ ) this expression simplifies to

$$\phi_i(r, z) = \text{sign}[z] \frac{J_0 \sigma_1 - \sigma_2}{\sigma_i \sigma_1 + \sigma_2} \sum_{n=1}^N \eta_n J_0(k_n r) e^{-k_n |z|} \quad (6.48)$$

### 6.5.3 Inverse problem

The mapping of axisymmetric interface perturbation into the electrical potential in the fluid at the cylinder boundary given by eq. (6.48) can be written as matrix equation

$$\phi_k = A_{kn} \cdot \eta_n, \quad (6.49)$$

where  $\phi_k$  is the value of the electrical potential in the fluid at the cylinder wall at the  $k$ -th measurement point, and  $z_k$  is the  $z$ -coordinate of the  $k$ -th measurement point with  $1 \leq k \leq K$ . The linear operator  $A_{kn} = J_0(y_n) e^{-y_n z_k}$  is called the system matrix. A direct inversion of  $A$  leading to  $\eta = \phi \cdot A^{-1}$  becomes unstable. Therefore we use the singular value decomposition technique [52] for reconstruction. Further, for a good reconstruction it is necessary to find the number of active modes in the system (number  $N$  in eq. (6.41)) which has the strongest influence on the reconstruction quality. We compute this parameter using the L-curve criterion [33].

The inverse problem for the non-axisymmetric case decouples into  $M$  inverse problems for the individual Fourier-modes (s. eq. (6.47)) whose mathematical structure is identical with that of the axisymmetric problem.

### 6.5.4 Examples of interface reconstruction

The simulation is performed in four steps as follows. First the amplitudes  $\eta_n$  or  $\eta_{mn}$  are prescribed which determine the interface shape. In the second step the measurement data  $\phi_k$  and  $\phi_{kp}$  of the electrical potentials at the cylinder boundary

are computed using the analytical solution (3.14) or (6.47). Then in the third step random white noise is added to the obtained electrical potential data set as  $\phi_{kp}(1 + \varepsilon\delta)$ , where  $-1 < \varepsilon < 1$  is a random number and  $\delta$  is the maximum amplitude of error. These operations simulate the noisy measurement of the electrical potentials. The fourth step is the reconstruction of the interfaces employing the algorithms described in subsection 6.5.3.

The examples of the axisymmetric interface reconstruction are shown in Fig. 6.11. The exact interface shape consists of first three modes and is denoted with solid line. The dotted line corresponds to the 5% data error, the dashed line - 10% data error, the dash dotted line - 20%. The  $r = 1$  corresponds to the fluid-cylinder boundary. The reconstruction was performed with exactly computed number  $N$  by applying the L-curve criterion. The curves of the exact interface and the reconstructed curves are virtually indistinguishable.

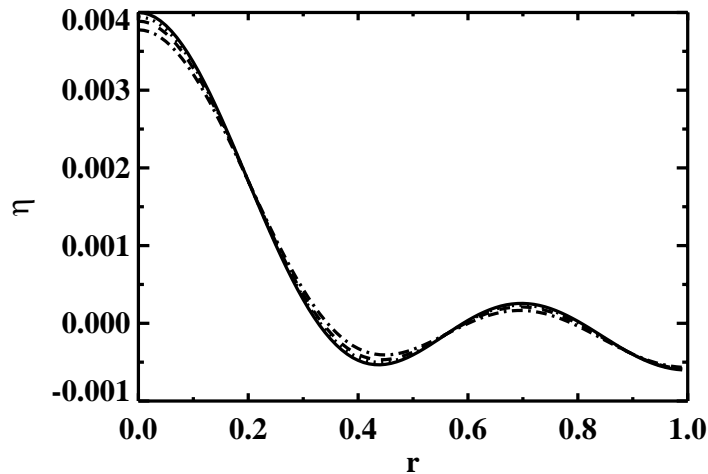


Figure 6.11: Reconstruction of axisymmetric interface.

Figure 6.12 presents examples of the non-axisymmetric interface reconstruction. The exact interface consists of the first three radial modes for 0th and first azimuthal modes. In this case the reconstructed interface is also very similar with the exact interface even for the high measuring error.



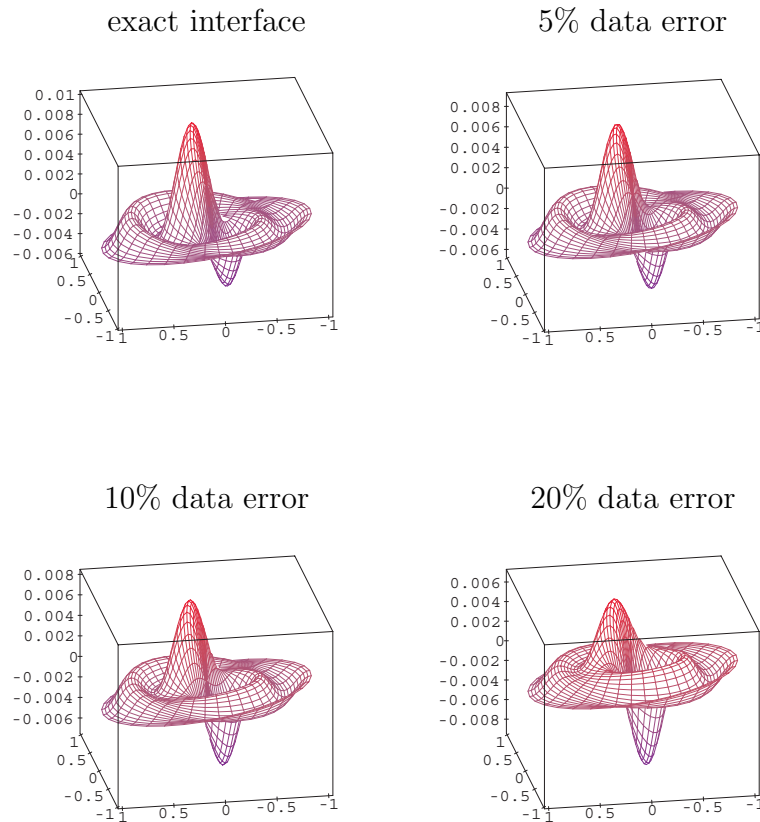


Figure 6.12: Reconstruction of non-axisymmetric interface.

### 6.5.5 Conclusion

In the present work we have described an algorithm for the interface reconstruction from electrical potential measurements at the fluid boundary in a two-fluid system with cylindrical configurations. We have investigated axisymmetric and non-axisymmetric interfaces. In both cases the interface shape is determined with high accuracy. The method is robust to measurement errors and works even at noise level as high as 20%.

In the future it is planned to verify the predictions of the presented theory experimentally. Our research will be also extended to systems with arbitrary form of cross-section. We shall also investigate the possibility of reconstruction from magnetic field measurements.



# References

1. BÄCK T. *Evolutionary algorithms in theory and praxis*. New York, Oxford: Oxford university press, 1996.
2. BAUMGARTL J., HUBERT A., MÜLLER G. The use of magnetohydrodynamic effects to investigate fluid flow in electrically conducting melts. *Phys. Fluids A*, vol. **5** pp. 3280-3289.
3. BERKOV D. V., GORN N.L. Reconstruction of the velocity distribution in conducting melts from induced magnetic field measurements. *Compt. Phys. Commun.*, vol. **86** (1995), pp. 255-263.
4. BOJAREVICS V., ROMERIO M.V. Long waves instability of liquid metal-electrolyte interface in aluminium electrolysis cells: a generalisation of Seles criterion. *Eur. J. Mech. B/Fluids*, vol. **13** (1994), pp. 33-56.
5. BRAUER H., KOSCH O., TENNER U., WIECHMANN H., ARLT A. A modified linear estimation approach for solving biomanetic inverse problems. *IEEE Transactions on magnetics*, vol. **32**:3 (1996), pp. 1298-1301.
6. BRAUER H., TENNER U., WIECHMANN H., ARLT A., ZIOLKOWSKI M., HAUEISEN J., NOWAK H., LEDER U. Physical Modelling of Phantoms for Biomagnetic Studies. *Proc. of Int conf on Measurement, Smolenice (Slovakia)* (1997), pp. 225-228.
7. BRAUER H., ZIOLKOWSKI M., KOSCH O., TENNER U., HAUEISEN J., NOWAK H., LEDER U. Reconstruction of Extended Current Sources in a Physical Thorax Phantom Using Magnetic Field and/or Electrical Potential Measurements. *11th International Conference on Biomagnetism, Sendai/Japan* (1998).
8. BRONSTEIN I. N., SEMENDJAEV K. A. *Taschenbuch der Mathematik (in german)*. Frankfurt am Main, Verlag Harri Deutsch, 1999.

9. BROWN B.H., LEATHARD A., SINTON A., MCARDLE F.J., SMITH R.W., BARBER D.C. Blood flow imaging using electrical impedance tomography. *Clin. Phys. Physiol. Meas.*, vol. **13** Suppl A (1992), pp. 175-179.
10. BROWN ET ALL. US Patent No. 5311878. Real-time electrical impedance tomography.
11. BROWN ET ALL. US Patent No. 5184624. Electrical impedance tomography.
12. BUTLER J., BONNECAZE R. Imaging of particle shear migration with electrical impedance tomography. *Phys. Fluids*, vol. **11** (1999), pp. 1982-1994.
13. CHANDRASEKHAR S. *Hydrodynamic and hydromagnetic stability*. International Series of Monographs on Physics. Oxford, At the Clarendon Press, 1961.
14. CHENEY M., ISAACSON D., NEWELL J. Electrical impedance tomography. *SIAM Review*, vol. **41** (1999), pp. 85-101.
15. CLARKE J., GOUBAU W.M. AND KETCHEN M.B. Thin film dc SQUID with low noise and drift. *Appl. Phys. Lett.* vol. **27** (1975), pp. 155-156.
16. DAILY W., RAMIREZ A. Electrical resistance tomography during in-situ tricholoethylene remediation at the Savannah River Site. *Appl. Geophysics*, vol. **33** (1995), pp. 239-245.
17. DAVIDSON P. An energy analysis of unstable, aluminium reduction cells. *Eur. J. Mech., /B Fluids*, vol. **13** (1994), pp. 15-32.
18. DAVIDSON P.A., LINDSAY R. Stability of interfacial waves in aluminium reduction cells. *J. Fluid Mech.*, vol. **362** (1998), pp. 273-295.
19. DAVIDSON P. Magnetohydrodynamics in material Processing. *Annu. Rev. Fluid Mech.*, vol. **31** (1999), pp. 273-300.
20. DINES K.A., LYTLE R.J. Analysis of electrical conducting imaging. *Geophysics*, vol. **46** (1981), pp. 1025-1036.
21. DJAMDJI F., GORVIN A.C., FREESTON I.L., TOZER R.C., MAYES I. C., BLIGHT S. R. Electrical impedance tomography applied to semiconductor wafer characterization. *Meas. Sci. Technol.*, vol. **7** (1996), pp. 391-395.
22. DÖSSEL O, KULLMANN W. SQUIDS and Bilder neuronaler Ströme. *Psys. Bl.*, vol. **44** (1988), pp. 423-425.

23. DRAZIN P.G, REID W.H. *Hydrodynamic stability*. Cambridge Monographs on Mechanics and Applied Mathematics. Cambridge: Cambridge University Press, 1981.
24. DROSTE CH., SEGATZ M. AND VOGELSANG D. Improved 2-dimensional model for magnetohydrodynamic stability analysis in reduction cells. *Light Metals*, (1998), pp. 419-428.
25. DROSTE CH. , SEGATZ M. AND VOGELSANG D.. Analysis of magnetohydrodynamic instabilities in aluminum reduction cells. *Light Metals*, vol. 313 (1994), pp. 313- 322.
26. DYACHENKO A. I., KOROPTKEVICH A. O., ZAKHAROV V. E. Weak turbulent Kolmogorov spectrum for surface gravity waves. *Phys. Rev. Lett.*, vol. **92**:13 (2004).
27. GABRIEL P. *Matrizen, Geometrie, Lineare Algebra*. Basel: Birkhäuser Verlag, 1996.
28. GEORGE D.L., TORCZYNSKI J.R., SHOLLENBERGER K.A., O'HERN T.J., CECCIO S.L. Validation of electrical impedance tomography for measurements of material distribution in two-phase flows. *Journal of Multiphase Flow*, vol. **26** (2000), pp. 549-581.
29. GOLDBERG D. *Genetic Algorithms*. Addison Wesley, 1988.
30. GOLUB G.H., REINSCH C. Singular value decomposition and least squares solutions. *Numer. Math.* vol. **14** (1970), pp. 404-420.
31. GOLUB G.H., MATT U. Generalized cross-validation for large scale problems. *J. Comp. Graph. Stat.* vol. **6**:1 (1997), pp. 1-34.
32. GUTHRIE R. I. L., LI M., CARROZZA C. The application of the electric sensing zone to liquid metals for on-line detection of inclusions. *Proc. 3rd Internatinal Symposium on Electromagnetic Processing of Materials*. Nagoya: The Iron and Steel Institute in Japan (2000), pp. 31-36.
33. HANSEN CH. Analysis of discrete ill-posed problems by means of the L-curve. *SIAM Review*, vol. **34** (1992), pp. 581-613.
34. HÄMÄLÄINEN M., HARI R., ILMONIEMI R., KNUUTILA J., LOUNASMAA O.V. Magnetoencephalography. *Review of modern Physics*, vol. **65**:2 (1993).
35. HARI R., ILMONIEMI R.J. Cerebral magnetic fields. *CRC Crit. Rev. Biom. Eng.* vol. 14, pp. 93-126.

36. HELMHOLTZ H. Über einige Gesetze der Verteilung elektrischer Ströme in körperlichen Leitern, mit anwendung auf die tierisch-elektrischen Versuche. *Ann. Phys. Chem.* vol. **89** (1853), pp. 211-233.
37. ISAACSON ET ALL. US Patent No. 5381333. Current patterns for electrical impedance tomography.
38. KAUFMANN L. C., NEUMAIER A. PET regularization by envelope guided conjugate gradients. *IEEE Trans. Medical Imag.*, vol. **15** (1996), pp. 385-389.
39. KASUGA M., FUKAI I., AMANO M. AND KUMOYAMA K. Remote Sensing of Induced Electric Current in Melt for Magnetic Czochralski Crystal Growth. *Jpn. J. Appl. Phys.* vol. **32** (1993), pp. L1103-L1105.
40. KIRKPATRICK S., GELATT C.D, VECCHI M.P. Optimization by simulated annealing. *Science* vol. **220**:4598 (1983) pp. 671-681.
41. KURENKOV A. AND THESS A. Reconstruction of interfaces between electrically conducting fluids from electric potential measurements. *Proc. of the PAMIR Conference*, (2000) France.
42. LANDAU L. D., LIFSHITZ E. M. *Course of theoretical physics, Vol. 6: Hydrodynamics*. Oxford, Pergamon Press, 1987.
43. LOUIS A. K. Numerik inverser Probleme. *GAMM-Mitteilungen*. vol. **1** (1990), pp. 5-27.
44. MEI CHIANG C. The applied dynamics of ocean surface waves. Singapore: JBW Printersn & Binders Ltd., 1992.
45. MILES J. AND HENDERSON D.. Parametrically forced surface waves. *Annu. Rev. Fluid Mech.*, vol. **22** (1990), pp. 143-165.
46. MOREAU R. J. AND ZIEGLER D. Stability of aluminum cells - a new approach. *Ligth Metals*, (1986), pp. 359-364.
47. MOREAU R.J. AND EVANS J.W. An analysis of the hydrodynamics of aluminium reduction cells. *J. Electrochem. Soc.*, vol. **131** (1984), pp. 2251.
48. OYE H.A., MASON N., PETERSON R.D. Aluminium: Approaching the New Millennium. *JOM*, vol. **51**:2 (1999), pp. 29-42.

49. PAIGE C.C., SAUNDERS M.A. LSQR: An algorithm for sparse linear equations and sparse least squares. *ACM Trans. on Meth. Software*, vol. **8:2**, (1982), pp. 43-71.
50. PARKER R.L. The inverse problem of resistivity sounding. *Geophysics*, vol. **42** (1984), pp. 2143-2158.
51. PEDLOSKY J. *Geophysical Fluid Dynamics*. New-York: Springer-Verlag, 1987.
52. PRESS W.H., TEUKOLSKY S.A., WETTERING W.T., FLANNERY B.P. *Numerical recipes in Fortran 77*. Cambridge: Cambridge university press, 2001.
53. RAMIREZ A., DAILY W., LABRECQUE D., OWEN E., CHESNUT D. Monitoring an underground steam injection process using electrical resistance tomography. *Water Resources Research*, vol. **29** (1993), pp. 73-87.
54. RAMIREZ A., DAILY W., BINLEY A., LABRECQUE D., ROELANT D. Detection of leaks in underground storage tanks using electrical resistance methods. *J. Environmental and Engineering Geophysics*, vol. **1** (1996), pp. 189-203.
55. RECHENBERG I. *Evolutionsstrategie'94. (Werkstatt Bionik und Evolutionstechnik, 1)*. Frommann, Holzboog, 1994.
56. ROMANI G.L., NARICI L. Principles and clinical validity of the biomagnetic method. *Med. Progr. Technol.* vol. **11** (1986), pp. 123-159.
57. SCHWARZ H. R. *Numerische Mathematik*. Stuttgart: Teubner, 1997.
58. SEGATZ M., DROSTE CH. Analysis of magnetohydrodynamic instabilities in aluminum reduction cells. *Light Metals*, (1994), pp. 313-322.
59. SELE T. Instabilities of the metal surface in electrolytic alumina reduction cells. *Met.Trans.*, vol. **8B** (1977), pp. 613-618.
60. SNEYD A.D., WANG A. Interfacial instability due to MHD mode coupling in aluminium reduction cells. *J. Fluid Mech.*, vol. **263** (1994), pp. 343-359.
61. STEFANI F, GERBETH G. Velocity reconstruction in conducting fluids from magnetic field and electric potential measurements. *Inverse Problems*, vol. **15** (1999), pp. 771-786.

62. STEFANI F, GERBETH G. On the uniqueness of velocity reconstruction in conducting fluids from measurements of induced electromagnetic fields. *Inverse Problems*, vol. **16** (2000), pp. 1-9.
63. STEFANI F, GUNDRUM T., GERBETH G. Contactless inductive flow tomography. *Phys. Rev E* vol. **70** (2004), 056306.
64. SUN H., ZIKANOV O., ZIEGLER D. Non-linear two-dimensional model of melt flows and interface instability in aluminium reduction cells. *Fluid Dyn. Res.*, vol. **35**:4 (2004), pp. 255-274.
65. TIKHONOV A., ARSEININ V. *Solution of ill-posed problems*. Wiley, New-York, 1977.
66. URATA N. Magnetics and metal pad instability. *Light Metals*, (1985), pp. 581-589.
67. WILLIAMS R.A., BECK M.S. *Process Tomography-Principles, Techniques and applications*. Oxford: Butterworth-Heinemann, 1995.
68. WILLIAMSON S.J., KAUFMAN L. Biomagnetism. *J. Magn. Mat.* vol. **22** (1981), pp. 129-201.
69. WILLIAMSON S.J., KAUFMAN L. Advances in neuromagnetic instrumentation and studies of spontaneous brain activity. *Brain Topogr.*, vol. **2** (1989), pp. 129-139.
70. XIE C.G., HUANG S.M., HOYLE B.S. AND BECK M.S. *Tomographic imaging of industrial process equipment-Development of system model and image reconstruction algorithm for capacitive tomography*. Edinburgh: Sensors & Their applications V, 1991.
71. ZIKANOV O., THESS A., DAVIDSON P.A., ZIEGLER D.P. A new approach to numerical simulation of melt flows and interface instability in Hall-Herout Cells. *Met. trans. B*, vol. **31** (2000), pp. 1541-1550.
72. *International Aluminium Institute*. <http://www.world-aluminium.org>



# Acknowledgments

Several people have inspired me and contributed to this work. I would like to express my gratitude to them.

At first I would like to thank my supervisor Prof. Andre Thess who has not only initiated this research but also was the perfect advisor. His deep physical insight and wide knowledge in the field of magnetohydrodynamic and especially in aluminium reduction cells was always of great assistance. We had a lot of interesting discussions which always motivated me for the investigations which are presented in this thesis. I have learned much from him about the magnetohydrodynamics, as well as the preparation of research results and presentations.

Furthermore, I would like to thank the thesis examiners Prof. Martin Oberlack and Prof. Yury Kolesnikow.

Dr. Brauer from TU Ilmenau helped me to get into the theory of inverse problems. Prof. Babosky spent hours discussing the reconstruction algorithm and helped me to formulate the mathematically correct inversion scheme.

Mr. Khujadze and Dr. Groll are acknowledged. They have corrected the text of the manuscript.

All my colleagues working at the department of Thermo- and Fluidynamics at Ilmenau Technical university are acknowledged for the strong support in my academic and private life, especially Dr. Resagk, Dr. duPuits, Dr. habil. Karcher. In day-to-day work and life my colleagues have provided a convivial and supportive atmosphere.

Many thanks to my friends, M.Broschart, N.Frey, T.Danko and everyone else for their support and encouragement.



## Erklärung

Ich versichere, dass ich die vorliegende Arbeit ohne unzulässige Hilfe Dritter und ohne Benutzung anderer als der angegebenen Hilfsmittel angefertigt habe. Die aus anderen Quellen direkt oder indirekt übernommenen Daten und Konzepte sind unter Angabe der Quelle gekennzeichnet.

Bei der Auswahl und Auswertung folgenden Materials haben mir keine Personen (entgeltlich oder unentgeltlich) geholfen.

Weitere Personen waren an der inhaltlich-materiellen Erstellung der vorliegenden Arbeit nicht beteiligt. Insbesondere habe ich hierfür keine entgeltliche Hilfe von Vermittlungs- bzw. Beratungsdiensten (Promotionsberater oder anderer Personen) in Anspruch genommen. Niemand hat von mir unmittelbar oder mittelbar geldwerte Leistungen für Arbeiten erhalten, die im Zusammenhang mit dem Inhalte der vorgelegten Dissertation stehen.

Die Arbeit wurde bisher weder im In- noch im Ausland in gleicher oder ähnlicher Form einer Prüfungsbehörde vorgelegt.

Ich bin darauf hingewiesen worden, dass die Unrichtigkeit der vorstehenden Erklärung als Täuschungsversuch angesehen wird und den erfolglosen Abbruch des Promotionsverfahrens zu Folge hat.

Ilmenau, den 16.Juni 2005

Oleksiy Kurenkov



# **Thesen zur Dissertation von O.Kurenkov:**

## **Reconstruction and stability analysis of interface between two conducting fluids**

1. In dieser Arbeit wurden drei Probleme untersucht. In dem ersten Teil der Arbeit wird eine lineare Stabilitätsanalyse an einem vereinfachten Modell einer Alu-Zelle untersucht. Im zweiten Teil wird ein neues Konzept für die Rekonstruktion der instabilen Grenzfläche in einer Aluminium-Elektrolysezelle (weiter Alu-Zelle) aus einer Potentialmessung vorgestellt. Im dritten Teil wird eine Methode entwickelt, die die Berechnung einer Magnetfeldstörung in einer Alu-Zelle anhand der bekannten Deformation der Aluminium-Kryolith Grenzfläche ermöglicht.
2. Aluminium wird mittels Electrolyse durch den Hall-Herault Prozess in Alu-Zellen hergestellt. Eine Alu-Zelle beinhaltet in Form zwei übereinander angeordneten Fluidschichten Kryolith (oben) und Aluminium (unten). Durch die Grenzfläche zwischen Aluminium und Kryolith fließt elektrischer Strom mit der Stromstärke von bis zu 500kA. Kryolith hat einen viel größeren spezifischen Widerstand im Vergleich zu Aluminium, was die Ursache für den immensen Energieverbrauch (bis zu 21,5 kWh für 1 kg Aluminium) darstellt. Die Verringerung der Dicke der Kryolithschicht ist nur begrenzt möglich, da die Grenzfläche Aluminium/Kryolith instabil ist. Das Anwachsen der Instabilitäten auf der Grenzfläche begünstigt einen Kurzschluß zwischen den Elektroden durch das gut leitende Aluminium, was die Zerstörung der Alu-Zelle bedeuten würde.
3. Die Entwicklung von modernen Alu-Zellen hat zwei dominante Ziele: die Verringerung von Produktionskosten, die im wesentlichen Teil aus dem Energieverbrauch resultieren, und die Steigerung der Effizienz einer Alu-Zelle. Infolgedessen ist die Sicherstellung der Funktion einer Alu-Zelle und die Kontrolle einer instabilen Grenzfläche von einer großer Bedeutung.
4. Die gezeigte lineare Stabilitätsanalyse einer Alu-Zelle dient zur Untersuchung der Wechselwirkung zwischen Kelvin-Helmholtz-Instabilität und der magneto-

hydrodynamischen (MHD) Instabilität. Die Kelvin-Helmholtz Instabilität wird durch den Geschwindigkeitgradienten an der Kryolith-Aluminium Grenzfläche verursacht. Die MHD-Instabilität ist ein Resultat von dem Interagieren der Grenzflächenwellen mit dem vertikalem Magnetfeld in der Zelle. Es wurden vier dimensionslose Parameter hergeleitet, die das Verhalten der Zelle beschreiben. Zwei von diesen (dimensionslose Strömungsgeschwindigkeit und MHD-Parameter) bestimmen die Grenzen von Stabilitätsregionen. Die zwei anderen (Materialparameter und Aspektverhältnis) verändern die Grenzen der Stabilität. Die Studie hat gezeigt, daß Kelvin-Helmholtz-Instabilität und MHD-Instabilität unabhängig voneinander auftreten, obwohl die Form der Wellen durch das Magnetfeld verändert wird.

5. Die entwickelte Methode zur Rekonstruktion der instabilen Grenzfläche in einer Alu-Zelle stellt eine neue nichtinvasive Technik dar, die auf den Ansätzen der "Electric Impedance Tomography" (EIT) beruht. Der vorhandene elektrische Strom, der zwischen den Elektroden angelegt ist, wird in dargestelltem Verfahren zur Detektion der Grenzfläche genutzt. Die Information über die Deformation der Grenzfläche spiegelt sich in der Verteilung des elektrischen Potentials beider Fluide wieder. Das Rekonstruktionsverfahren nutzt die Ergebnisse aus der Messung der Störung des elektrischen Potentials. Das Verfahren wird durch sehr hohe Schnelligkeit und Zuverlässigkeit charakterisiert und ist dadurch für Echtzeit-Systeme zur Überwachung der instabilen Alu-Zellen geeignet.
6. Die Berechnung der Störung des Magnetfeldes in einer Alu-Zelle, die in dem dritten Teil der Arbeit untersucht wurde, beruht auf dem modifizierten Biot-Savart-Gesetz. Das dreidimensionale Integral läßt sich für diesen Fall in eine wesentlich einfachere Form umwandeln. Die vorgeschlagene Methode kann für die Entwicklung von Rekonstruktionsalgorithmen dienen, die die Grenzfläche aus der Magnetfeldmessung außerhalb der Alu-Zelle bestimmen sollen.
7. Die vorliegende Arbeit trägt zur Kontrolle von Alu-Zellen und dem Verständniss der Instabilitätsmechanismen in Alu-Zellen bei. Die gewonnenen Erkenntnisse eignen sich auch zur Weiterentwicklung eines Systems zum Verhindern der unwillkommenen Instabilitäten in Alu-Zellen.